VILNIUS UNIVERSITY

CENTER FOR PHYSICAL SCIENCE AND TECHNOLOGY

Jevgenij Pavlov

Detector structures on defect-rich silicon and fast-response wide-gap semiconductor materials

Doctoral dissertation

Technological Science, Material Engineering (08 T)

Vilnius 2016

Doctoral dissertation was prepared during period of 2012-2016 years at Vilnius University Faculty of Physics and Institute of Applied Research

Supervisor:

Prof. Dr. Sc. Eugenijus Gaubas (Vilnius University, Technological Sciences, Material Engineering – 08 T).

Acknowledgements

First of all, I would like to thank my parents for their support and encouragement, during long years of my education.

I would like to express my appreciation to Prof. Dr. Sc. E. Gaubas for supervising this thesis and his continues support, advice, encouragement and long lasting discussions about fundamental problems of describing of hadron detectors.

I am thankful to my friend and senior colleague Dr. T. Čeponis for consultations.

I am thankful to my friends and colleagues D. Meškauskaitė, A. Jasiūnas, A. Velička, A. Tekorius, D. Bajarūnas, and Dr. V. Kalendra for good team-work and cooperation.

Special thanks to M. Pučėtaitė for help in FTIR spectroscopy of HPHT diamond.

Lithuanian State Science and Studies Foundation and Research Council of Lithuania are acknowledged for the financial support.

Content

List of abbreviations

LHC – Large Hadron Collider

MOCVD – metal organic chemical vapour deposition

SI – semi-insulating

CERN – European Organization for Nuclear Research

TSC – thermally stimulated current

DLTS – deep level transient spectroscopy

MW – microwave

TCT – transient current technique

HPHT – high pressure-high temperature

HTLP – high temperature-low pressure

CVD – chemical vapour deposition

HVPE – hydride vapour phase epitaxy

PPI – pulsed photo-ionization

BELIV – barrier evaluation by linearly increasing voltage

FTIR – Fourier transform infrared spectroscopy

SEM – scanning electron microscope

MW-PC – microwave probed photoconductivity

TR-PL – time resolved photoluminescence

C-DLTS – capacitance DLTS

I-DLTS – current DLTS

O-I-DLTS –optical current DLTS

OPO – optical parametric oscillator

DFG – differential frequency generator

XRD – X-ray diffraction

ESR – electron spin resonance

EDXS – energy dispersed X-ray spectroscopy

PPI – pulsed photo-ionization

DAP – donor -acceptor photoluminescence

SER – stretched-exponential relaxation

ICDC – injected charge domain drift current

PCB – printed circuit board

MCZ – magnetic Czochralski

S-R-H – Shockley-Read-Hall

I. Introduction

Research problem. The necessity of radiation tolerant, fast and solar-blind sensors for radiation-hard electronics in medicine, aerospace and military applications [1-3] stimulates search for new materials and development of the advanced device structures. In addition, new material quality control technologies and device operation modes should be designed in creation of the modern sensor structures.

As usual, modern materials, such as newly synthesized and grown binary/ternary compounds, contain large density of grown-in defects due to a poor development of the as-invented material fabrication technologies. On the other hand, the extremely intense high-energy irradiations, inevitable for the sensors addressed to functioning within harsh areas of high-energy physics (e.g., super-high-luminosity Large Hadron Collider (LHC) [2]) experiments, nuclear-power plants and cosmic-space apparatus, create the extremely high densities of radiation defects even during rather short exposure times.

The silicon based devices, fabricated on the best technologically developed materials, mainly suffer from the introduction of radiation defects. Moreover, their sensitivity to natural lighting and the rather large leakage currents within natural environment (due to rather narrow band-gap) limits the fields of silicon sensor applications within specific, such as mentioned above, detection configurations. Thus, the wide band-gap high-density materials, such as synthetic diamonds and gallium nitride (GaN), become a promising matter for fabrication of the specific detectors, due to significantly beneficial Fano factors [3], relative to Si. On the other hand, the wide band-gap materials can serve in formation of the dual purpose sensors, which are capable to generate both the electrical and optical signals. Nevertheless, technological developments of fabrication of the sensors based on the latter wide band-gap materials stay on the rather initial stage. There are a lot of problems to solve in creation of the advanced detectors capable to operate as radiation-hard, long-lasting and low-leakage sensors.

Several contradictive requirements exist for sensor design. First of all, the depth- and lateral-homogeneity of sensor structures is necessary to have linearity of detector response. This requirement raises difficulties in applications of HPHT (high pressure high temperature) grown diamond and MOCVD (metal organic chemical vapour deposition) grown GaN materials, where large densities of technological defects such as threading dislocations, clusters of impurities, crystallographic morphology defects etc., are inevitable for nowadays technology layers even of the rather small areas and thicknesses [3]. To detect events of rather small interaction cross-section, inherent for sensors of the penetrative radiations, the thick sensor structures are required, satisfying depth homogeneity requirement. The crystalline materials with elevated carrier transport parameters (as, carrier mobility, transit time) are desirable to get fast and perfect detector responses. However, heavily irradiated crystals become the rather disordered structures. To expediently govern the operation features of junction structure devices with thick sensor structure by external voltage or to implement a full-depletion regime, the rather pure materials of large resistivity should be employed, where low doping level should be maintained. This large resistivity regime would be inherent for pure wide-band-gap crystals. However, high densities of the technological and radiation defects compensate easily the dopants making the fabricated junctions non-operational. On the other hand, the large resistivity, semi-insulating (SI) materials are fabricated by introduction of the high density of impurities. These defects are acting as fast carrier killers, to compensate the un-intentional doping of wide-band-gap materials by introduced technological defects, which act as carrier generation centres. Nevertheless, the introduction of fast carrier recombination defects, suppresses the drift current component within sensor response, thus making the position and energy sensitive particle detectors to be “badly-operational”. The spontaneous and piezo-polarization effects in crystals, lacking the inversion centre symmetry, may also affect the functional characteristics of sensors. To reach a trade-off among contradictive

requirements in design of the specific sensors, new technological, methodical and defect engineering approaches are necessary.

There are two main mechanisms of creation of the radiation defects within semiconductor materials, - namely, the displacement and ionization damage [2, 3]. Ionizing damage events happen by creation of fast electrons, those interacting with material are capable create point defects. The displacement damage – when lattice atoms are knocked from their sites, thus, creating vacancies and interstitials. Thereby, the cascades of point and extended radiation defects, as a consequence of further clustering and annihilation of the primary introduced defects, are generated along the tracks of the penetrative particles [4]. Large density of radiation induced defects, acting as carrier traps, affect the device functional parameters by reducing the charge collection efficiency, by increasing the leakage current and, consequently, by modifying the detector response [5-8]. This necessitates a deeper study of peculiarities of carrier recombination channels attributed to radiation defects. Carrier thermal generation and trapping parameters are the most important in evaluation of the performance of particle detectors operating at high fluences. In materials containing considerable densities of technological defects, like synthetic diamond and GaN, interplay of radiation and intrinsic defects becomes complicated and important [9-15]. Therefore, new defect identification and spectroscopy techniques as well as defect engineering technologies are desirable in fabrication of advanced and specific particle detectors.

In experiments of high energy physics at European Organization for Nuclear Research (CERN), the high purity and large resistivity Si particle detectors of PIN structure, operating at full depletion regime, are commonly employed for tracking of high energy radiations. These detectors should withstand fluences higher than 10^{16} cm^{-2}. However, the effective doping density N_{eff} of the material varies during detector exploitation due to accumulated radiation defects, whose form charged centres acting as carrier traps. As a result, the charge collection efficiency, being the most important

characteristic of detector functionality, is reduced [16]. Evaluation of the mechanisms of radiation damage of the particle detectors is commonly implemented by combining several measuring techniques. Variations of carrier generation lifetime are examined by using technique of the thermally stimulated current (TSC) and by capacitance deep level transient spectroscopy (DLTS). In the range of high ($>10^{15}$ cm^{-2}) irradiation fluence, application of the above-mentioned techniques is complicated since the radiation defect density significantly overpasses the concentration of dopants, and cluster formation may become the dominant mechanism in radiation damaged material. Measurements of the excess carrier capture/recombination characteristics are performed by well-known photoconductivity technique, which can be implemented in contact-less mode by pulsed excitation – microwave (MW) probe method. Examination of the drift current transients using transient current technique (TCT) emulates most closely the regimes of detector operation, where electrical signals are measured by registering of displacement and convection current components formed by injection and drift of the secondary carrier pairs. However, analysis of these current transients is commonly based on application of quasi-steady–state approach when using TCT technique [17, 18]. Application of this TCT technique becomes even more complicated when built-in or dynamic polarization fields appear in wide-bandgap materials [19].

The problem of pulsed current signals in junction and capacitor type sensors (due to drifting surface charge domain) is considered for the analysis of the operational characteristics in photo- and particle-detectors. The analysis of transient currents [18, 20-25] due to moving charges is commonly based on the Shockley-Ramo theorem [26, 27]. Alternatively, current density changes dependent on applied voltage can be simulated based on Boltzmann equation, e.g., [28], using conservation laws for carrier concentration, momentum and energy. However, the latter approach is acceptable for simulation of quasi-steady-state regime, and, as emphasized in [29], “an analysis based on the Boltzmann equation with a rigorous treatment of the collision integral is

prohibitive" in the dynamic theories concerned with the transport properties under dynamic conditions, *i.e.*, when the electric field varies in time and space. Therefore, the dynamic models including electric field variations are needed for deeper understanding of the transient currents in particle and photo-detectors.

Wide-bandgap semiconductor materials like diamond, GaN and CdS are attractive for fabrication of particle detectors, as the efficient and fast radiative recombination provides opportunity to get both the electrical and optical signals from sensors made of these materials. Technology of making polycrystalline CdS layers sensitive to ionizing radiations is rather cheap. However, operational characteristics of sensors made of GaN or CdS significantly depend on technologically introduced defects acting as rapid traps of excess carriers which reduce charge collection efficiency of detectors. Additionally, formation of mesa structures is the simplest approach in fabrication of electric signal detectors using sputtered or epitaxial layers of these materials [9]. Moreover, technological developments of formation of the terrace structures by combining plasma etching, laser ablation and other novel techniques represent only the initial stages in creation of the reliable fabrication means [9]. The efficiency of dual-purpose detectors, by employing of the scintillation and electrical signals, and of their functionality had insufficiently been investigated [6].

Synthetic diamond is the most promising material in fabrication of specific, extremely radiation tolerant sensors. However, large densities of the technologically inevitable impurities and crystalline morphology defects lead to complicated application of the diamond structures for manufacturing of radiation detectors. Therefore, investigation of the characteristics of synthetic diamond grown by various methods, such as high pressure-high temperature (HPHT), high temperature-low pressure (HTLP), chemical vapour deposition (CVD), is important in search of new matter for formation of the efficient particle detectors. The comparative study of several wide-band-gap materials in aspect of formation of the dual-purpose and radiation tolerant sensors would

be an effective tool for evaluation of the most acceptable design of detectors functional for the range of elevated fluences.

Objectives of research. This study was addressed to search of the efficient device operation modes, design configurations and the most suitable materials for the formation of fast, radiation tolerant and dual-purpose sensors, capable to generate optical and electrical responses.

The tasks were concentrated on:

- spectroscopy of technological and radiation induced defects by combining several techniques for the comprehensive and reliable characterization of HPHT and CVD synthetic diamond, HVPE (hydride vapour phase epitaxy) and MOCVD GaN materials by covering a wide range of the trap and effective doping densities;
- research of the impact of the technological procedures of the formation of junctions, of passivating layers and of electrodes on the operational characteristics of devices using silicon as a modelling material;
- investigation of radiation defect formation under irradiations by reactor neutrons, protons and pions of Si material and detectors covering the range of fluences from 10^{11} to 10^{16} cm^{-2} and the regimes for the efficient radiation defect anneals;
- study the evolution of the photo-electrical and luminescence characteristics during hadron irradiations of the CdS and GaN materials;
- creation of the analytical models and of simulation algorithms for description of the dynamics of the electric field distribution and evolution of the current components within pulsed detector signals due to the injected bipolar domains of secondary carrier pairs;
- development of the techniques for profiling of the transient sensor signals for evaluation of the parameters of carrier transport, recombination and thermal emission as well as for analysis of the polarization effects in wide-bandgap materials;

- development of the technology for the junction and capacitor type sensor formation based on synthetic diamond and GaN materials grown using different methods.

Relevance and scientific novelty. Defect engineering of the technologically introduced impurities and crystal imperfections is a rather permanent problem in various applications of the newly synthesized or exploited materials for device fabrication. Despite of big progress in silicon based electronics and developments of silicon technology, specific tasks still exist in passivation of defects and suppression of their interplay, in formation of barriers and contacts in heavily doped or radiation damaged materials for production of the efficient solar cells and radiation hard detectors, etc. Solution of these problems, addressed to creation of novel defect engineering approaches, to particular silicon applications for dosimetry, require the development of the in situ material characterization techniques during irradiations. Moreover, silicon as the most technological material is desirable as the modelling matter in prediction of the defect interplay and device operation features in other materials containing large densities of the technological and radiation defects. Thus, in this research, several relevant investigations have been implemented using silicon as the tentative material in development of the electrode deposition and of the specific characterization techniques.

The novel approaches were necessary in description of the complicated current transients in order to clarify the registered electrical and optical responses of the radiation and photo-sensors. The dynamic models for description of the current transients in junction and capacitor type detectors under injection of electron-hole pairs have been developed. The regimes of bipolar and monopolar carrier drift and of the avalanche amplification have been discriminated. The role of the carrier capture and thermal emission as well as of the external circuit has been clarified in formation of detector signals. The implementation of the detection modes, dependent on the injected charge density, close Ramo's regime and for small drifting charge, has been

analyzed in order to reveal possibilities of the sensor signal governing by external voltage and under increasing density of traps. It has been demonstrated that synchronous carrier drift and trapping lead to a vast variety of possible current pulse waveforms. On the basis of the novel dynamic models, transient current profiling techniques have been developed and approved for characterization of the silicon and wide-band–gap semiconductor detectors. It has been discriminated the fast detection regimes in materials with different densities of recombination centres by sensing variations of the carrier concentration and drift components.

The technique of synchronous profiling of the microwave probed photoconductivity and time resolved photoluminescence spectra during irradiation have been applied and approved for characterization of the synthetic diamond and GaN materials in order to clarify correlations of the distribution of the grown-in as well as radiation defects and carrier radiative as well as non-radiative recombination channels. It has been demonstrated that this novel technique is an efficient tool for evaluation of secondary carrier pair production by penetrative hadrons and for extraction of defect introduction rates by ionizing radiations in different materials. The techniques of pulsed photo-ionization (PPI) spectroscopy and barrier evaluation by linearly increasing voltage (BELIV) have been demonstrated as the efficient methods for detection of intrinsic and radiation induced defects in silicon and wide band-gap materials and devices. These techniques appeared to be efficient in control of defect engineering procedures performed by heat treatments, as demonstrated on different technology and conductivity type Si irradiated by high energy protons, neutrons and pions. Efficiency of the combining of several spectroscopies (Fourier transform infrared spectroscopy (FTIR), luminescence), microscopy (scanning electron microscope (SEM) and con-focal), electron-spin resonance and electrical-optical (microwave probed photo-conductivity (MW-PC), time resolved photo luminescence (TR-PL)) characterization techniques in reliable identification of defects has been demonstrated. For instance, the prevailing grown-in point defects, associated

with neutral and charged nitrogen impurity complexes as well as the pairs of nitrogen atoms on neighbouring sites, and the nickel impurities in HPHT diamond were unveiled. The transient techniques have been developed for analysis of the polarization effect. Relaxation of recovery of the detector peak current values in diamond and GaN sensors under a set of the carrier injection pulses has been employed to discriminate dynamic and static components of surface polarization. It has been shown that charge collection efficiency at low voltages can be considerably limited due to screening of the external electric field caused by the polarization effects in such structures under injection of the bulk charge within inter-electrode gap.

The novel design and formation technology has been created and approved in fabrication of mesa structures on the MOCVD GaN epi-layers by using plasma etching, laser ablation and electrode deposition steps. The electrode deposition is there implemented on the terrace structures using metal sputtering followed by sintering procedures and exploiting buffer layers as rear contact of the sensors. These technological developments are promising in fabrication of future planar sensors where polarization effects can be excluded. Also, technology of formation of bulk capacitor-type sensors, filled with the wide band-gap (GaN and diamond) materials, has been designed. It has been demonstrated that such simple sensors can be fast and rather efficient radiation detectors.

Practical importance. The technologies for sensor formation on MOCVD GaN epi-layers by depositing the Schottky barriers and plane-parallel electrodes have been developed. These technologies can be applied in production of solar-blind, low leakage and fast response detectors. The specific plasma etching, laser ablation and electrode deposition technological procedures are promising in fabrication of future planar sensors where polarization effects can be excluded.

The techniques of PPI spectroscopy and BELIV can be the efficient methods for detection of the intrinsic and radiation induced defects in silicon

and wide band-gap materials and devices. These techniques appeared to be efficient tools in control of defect engineering procedures performed by heat treatments. The designed methodology of the combining of several spectroscopies, microscopy, electron-spin resonance and electrical-optical characterization techniques is a reliable tool for identification, separation and characterization of various species of defects.

The novel dynamic models for description of the current transients in junction and capacitor type detectors under injection of electron-hole pairs and for analysis of the avalanche amplification modes can be useful in design of the detector operation regimes. The transient current profiling techniques based on the novel dynamic models can be applied for comprehensive characterization of the silicon and wide-bandgap semiconductor detectors in evaluation of such parameters as charge collection efficiency, transit and carrier trapping time, dynamic polarization, mobility if carriers.

Statements in defence. The main statements in defence of this thesis are as follows:

1. The developed models for description of current transients allow emulating the dynamics of the electric field formation and the evolution of the drift and carrier trapping components, and the model of carrier pair multiplication process is suitable for design of the internal avalanche amplification regimes.
2. The techniques of transient current profiling by external voltage and positioning of carrier photo-injection can be applied for comprehensive characterization of the silicon and wide-bandgap semiconductor detectors.
3. Inspection of carrier lifetime values in pion irradiated wafer fragments of electronics-grade silicon can be a reliable tool for pion dosimetry in wide range of fluences, where carrier lifetime dependence on pion fluence fits the same calibration curve for hadrons.
4. The designed formation technology in fabrication of mesa structures on the MOCVD GaN epi-layers allow to fabricate fast radiation sensors, capable to generate both the optical and electrical signals.

Author's contribution. During this study, author has performed measurements: capacitance-voltage characteristics, C-DLTS, I-DLTS, O-I-DLTS, BELIV, FTIR and luminescence spectroscopy. Also, author implemented the *in situ* (during proton irradiations) measurements of microwave probed photoconductivity transients and scintillation spectra in various materials. Moreover, author implemented a lot of experiments at CERN, where he installed and approved the instrument VUTEG-5-AIDA. Author performed simulations of pulsed current signals in GaN and diamond based junction as well as capacitor type particle detectors. Main results of dissertation author presented within a set of international ("International Workshop of Radiation Imaging Detectors '14" (IWORID'14) and IWORID'15, "Radiation Interaction with Material and Its Use in Technologies" in 2014, "International Conference on Ion Beam Modification of Materials" (IBMM2014) in 2014, "Workshop on Radiation hard semiconductor devices for very high luminosity colliders" 27th RD50 Workshop in 2015) and national ("Lithuanian national physics conference" LNFK40 in 2013) conferences. Author has prepared several drafts of article manuscripts.

Several experimental studies were performed in collaboration with PHD students D. Meškauskaitė (in O-DLTS characterization of MOCVD GaN Schottky diodes) and I. Reklaitis (in forming MOCVD GaN Schottky). Several publications were prepared in collaboration with Dr. T. Čeponis, A. Tekorius, J. Kalesinskas, J. Vyšniauskas. All the investigations, data analysis and writing of manuscript drafts were made together and under supervision of Prof. Dr. Sc. E. Gaubas and Dr. T. Čeponis.

In situ experiments on the study of carrier lifetime and scintillation characteristic during protons implantations were performed by ion accelerator installed at State Research Institute Centre for Physical Sciences and Technology, Vilnius. Recombination characteristics of carriers in Si irradiated by pions were measured at CERN using VUTEG-5-AIDA instrument. Measurements of PPI spectra on the pristine materials have been combined

with simultaneous control of carrier lifetime, implemented in contact-less mode using MW-PC transients. The spectrally tuned 40 fs excitation pulses were generated by OPO (optical parametric oscillator) and DFG (differential frequency generators) instruments installed at Department of Quantum Physics and VU Laser Research Centre.

Publications. The main results of this study are published within 14 scientific articles [A1-A14] and the research results have been approved within 15 oral and poster presentations [P1-P15].

Articles:

A1. E. Gaubas, T. Ceponis, E. Kuokstis, D. Meskauskaite, **J. Pavlov** and I. Reklaitis, *Study of Charge Carrier Transport in GaN Sensors,* Materials **9** (2016**)** 293.

A2. **J. Pavlov**, T. Ceponis, E. Gaubas, D. Meskauskaite, I. Reklaitis, J. Vaitkus, R. Grigonis and V. Sirutkaitis, *Comparative study of deep levels in HVPE and MOCVD GaN by combining O-DLTS and pulsed photo-ionization spectroscopy*, JINST **10** (2015) C12015.

A3. E. Gaubas, T. Ceponis, V. Kalesinskas, **J. Pavlov** and J. Vysniauskas, *Simulations of Operation Dynamics of Different Type GaN Particle Sensors*, Sensors **15** (2015) 5429-5473.

A4. E. Gaubas, T. Čeponis, **J. Pavlov**, *Modeling of radiation damage recovery in particle detectors based on GaN*, Nucl. Instrum. Meth. B **365** (2015) 163-167.

A5. E. Gaubas, T. Čeponis, **J. Pavlov**, A. Tekorius, *In situ variations of the scintillation characteristics in GaN and CdS layers under irradiation by 1.6 MeV,* Nucl. Instrum. Meth. B, **365** (2015) 159-162.

A6. E. Gaubas, T. Ceponis and **J. Pavlov***, Pulsed current signals in capacitor type particle detectors, Journal of instrumentation*, JINST **10** (2015) C01006.

A7. E. Gaubas, T. Ceponis, **J. Pavlov**, A. Jasiunas, V. Jonkus, D. Meskauskaite and A. Tekorius, *Carrier decay and luminescence characteristics in hadron irradiated MOCVD GaN,* JINST **9** (2014) C12044.

A8. E. Gaubas, T. Ceponis, A. Jasiunas, V. Kalendra, **J. Pavlov**, N. Kazuchits, E. Naumchik, M. Rusetsky, *Lateral scan profiles of the recombination parameters correlated with distribution of grown-in impurities in HPHT diamond*, Diam. Relat. Mater. **47** (2014) 15–26.

A9. E. Gaubas, T. Ceponis, **J. Pavlov**, and A. Baskevicius, *Profiling of the injected charge drift current transients by cross-sectional scanning technique*, J. Appl. Phys. **115** (2014) 054509.

A10. **J. Pavlov**, D. Bajarūnas, T. Čeponis, E. Gaubas, D. Meškauskaitė, *Spectroscopy of Technological Defects in Si Solar Cells by Analysis of Temperature Dependent Generation Currents*, 1392–1320 Mater. Sci-Medzg. **20** (2014) 252-255.

A11. **J. Pavlov**, E. Gaubas, T. Ceponis, *Simulation of the Pulsed Current Responses in GaN and Diamond Based Capacitor Type Particle Detectors*, Materials of the international Conference Proceedings "Radiation Interaction with Material and Its Use in Technologies 2014" Kaunas, Technologija (2014) 278-281.

A12. T. Ceponis, E. Gaubas , V. Balevicius , S. Galkin , A. Jasiunas , K. Katrunov, V. Kovalevskij, **J. Pavlov**, V. Remeikis , D. Shevchenko, G. Tamulaitis, A. Tekorius, *Comparative Study of Scintillation Characteristics of CdS and ZnSe Varied during 1.6 MeV proton irradiation*, Materials of the international Conference Proceedings, Radiation Interaction with Material and Its Use in Technologies 2014, Kaunas, Technologija (2014), 405-408.

A13. E. Gaubas, T. Čeponis, **J. Pavlov**, A. Velička, V. Kalesinskas, *Spectroscopy of radiation traps in Si by temperature dependent photoconductivity and generation currents*, Lith. J. Phys. **54**, (2014) 89–93.

A14. E. Gaubas, D. Bajarūnas, T. Čeponis, D. Meškauskaitė, and **J. Pavlov**, *Optically induced current deep level spectroscopy of radiation defects in neutron irradiated Si PAD detectors*, Lith. J. Phys. **53** (2013) 215–218.

A15. E. Gaubas, T. Ceponis, A. Jasiunas, V. Kovalevskij, D. Meskauskaite, **J. Pavlov,** V. Remeikis, A. Tekorius, J. Vaitkus, *Correlative analysis of the in situ changes of carrier decay and proton induced photoluminescence*

characteristics in chemical vapor deposition grown GaN, Appl. Phys. Lett. **104** (2014) 062104.

Presentations at conferences:

P1. E. Gaubas, T. Ceponis, **J. Pavlov**, J. Vaitkus, M. Moll, C. Gallrapp, M. Glaser, B. Gkotse, F. Ravotti. *Carrier lifetime variations in pion irradiated and annealed* Si. 27th RD50 Workshop, CERN, Geneva, 2015.

P2. **J. Pavlov**, T. Ceponis, E. Gaubas, D. Meskauskaite, J. V. Vaitkus, R. Grigonis, V. Sirutkaitis, *Comparative study of deep levels in HVPE and MOCVD GaN by combining O-DLTS and pulsed photo-ionization spectroscopy*, iWoRiD'15, DESY Hamburg, 2015.

P3. J. Vaitkus, E. Gaubas, T. Ceponis, **J. Pavlov**, I. Reklaitis, *Transient signals of the capacitor and Schottky barrier type HVPE and MOCVD GaN sensors,* iWoRiD'15, 2015.

P4. **J. Pavlov**, E. Gaubas, T. Ceponis, A. Jasiunas, V. Kovalevskij, D. Meskauskaite, A. Tekorius. *In situ changes of carrier decay and proton induced photoluminescence characteristics in MOCVD grown GaN,* iWoRiD'14, Trieste, 2014.

P5. T. Ceponis, E. Gaubas, **J. Pavlov**, *Pulsed current signals in capacitor and junction type particle detectors,* iWoRiD'14, Trieste, 2014.

P6. E. Gaubas, T. Ceponis, **J.Pavlov**, and J. Vysniauskas, *Operation characteristics and radiation damage of particle detectors based on GaN*, IBMM2014, Leuven, 2014.

P7. T. Ceponis, E. Gaubas, **J. Pavlov**, and A. Tekorius, *In situ variations of the scintillation characteristics in GaN and CdS layers under irradiation by 1.6 MeV protons*, IBMM2014, Leuven, 2014.

P8. **J. Pavlov**, E. Gaubas, T. Ceponis, *Simulation of the Pulsed Current Responses in GaN and Diamond Based Capacitor Type Particle Detectors*, International conference Radiation Interaction with Material: Fundamentals and Applications, Kaunas, 2014.

P9. A. Tekorius, E. Gaubas, T. Ceponis, A. Jasiunas, V. Kovalevskij, D. Meskauskaite, **J. Pavlov**, V. Remeikis, J. Vaitkus, *In Situ and Ex Situ Study of Variations of Recombination Characteristics in MOCVD Grown GaN under Hadron Irradiations*, International conference Radiation Interaction with Material: Fundamentals and Applications, Kaunas, 2014.

P10. **J. Pavlov**, T. Čeponis, E. Gaubas. *Profiling of current transients in silicon particle detector*, Advanced materials and technologies, Palanga, 2013.

P11. **J. Pavlov**, D. Bajarūnas, T. Čeponis, E. Gaubas. *Technologinių defektų si saulės elementuose spektroskopija generacinės srovės temperatūrinių kitimų analizės būdu*. LNFK, Vilnius, 2013.

P12. E. Gaubas, T. Čeponis, **J. Pavlov**, A. Šimkutė, A. Stalnionis. *Dreifo srovės kinetikų dalelių detektoriuose profiliavimas skersinės žvalgos būdu*. LNFK, Vilnius, 2013.

P13. D. Bajarūnas, T. Čeponis, E. Gaubas, **J. Pavlov**, *Radiacinių defektų giliųjų lygmenų spektroskopija neutronais apšvitinto Si detektoriuose optiškai injektuotų srovių kinetikų metodu*, LNFK, Vilnius, 2013.

P14. E. Gaubas, T. Čeponis, V. Kalendra, **J. Pavlov**, J. V. Vaitkus, *Radiacinių defektų spektroskopija ir srovių dalelių detektoriuose profiliavimas*, LNFK, Vilnius, 2013.

P15. **J. Pavlov**, E. Gaubas, T. Čeponis, V. Kalendra, *Radiacinių defektų spektroskopija CERN standarto Si detektoriuose*, third junior researchers' conference (III JMK), Tarpdalykiniai tyrimai fiziniuose ir technologijos moksluose – 2012, Vilnius, 2013.

Other publications:

A16. E. Gaubas, I. Brytavskyi, T. Ceponis, A. Jasiunas, V. Kalesinskas, V. Kovalevskij, D. Meskauskaite, **J. Pavlov**, V. Remeikis, G. Tamulaitis, A. Tekorius, *In situ variations of carrier decay and proton induced luminescence characteristics in polycrystalline CdS*, J. Appl. Phys. **115** (2014) 243507.

A17. E. Gaubas, T. Ceponis, A. Jasiunas, **J. Pavlov**, A. Tekorius, D. Shevchenko, K. Katrunov, V. Kovalevskij, V. Remeikis, S. Galkin, G.

Tamulaitis, *In situ variations of proton-induced luminescence in ZnSe crystals*, J. Phys. D: Appl. Phys. **47** (2014) 265102.

A17. A. Tekorius , E. Gaubas, T. Ceponis , **J. Pavlov**, J. Vaitkus, M. Glaser, M. Moll, *Fluence and Anneal Dependent Variations of Recombination Parameters in Si Irradiated by 26 GeV Protons*, Materials of the international Conference Proceedings "Radiation Interaction with Material and Its Use in Technologies 2014" Kaunas, Technologija (2014) 432-435.

A19. A. Tekorius, E. Gaubas, T. Ceponis, A. Jasiunas, V. Kovalevskij, D. Meskauskaite, **J. Pavlov**, V. Remeikis, J. Vaitkus, *In Situ and Ex Situ Study of Variations of Recombination Characteristics in MOCVD Grown GaN under Hadron Irradiations*, Materials of the international Conference Proceedings "Radiation Interaction with Material and Its Use in Technologies 2014" Kaunas, Technologija (2014) 436-439.

P17. A. Tekorius, E. Gaubas, T. Ceponis, A. Jasiunas, V. Kovalevskij, D. Meskauskaite, **J. Pavlov**, V. Remeikis. *In situ variations of carrier recombination characteristics in polycrystalline CdS during 1.6 MeV proton irradiation,* iWoRiD'14, Trieste, 2014.

P17. T. Ceponis, E. Gaubas , V. Balevicius , S. Galkin , A. Jasiunas , K. Katrunov, V. Kovalevskij, **J. Pavlov**, V. Remeikis , D. Shevchenko, G. Tamulaitis, A. Tekorius, *Comparative Study of Scintillation Characteristics of CdS and ZnSe Varied during 1.6 MeV Proton Irradiation*, International conference Radiation Interaction with Material: Fundamentals and Applications, Kaunas, 2014.

P18. A. Tekorius, E Gaubas, T. Ceponis , **J. Pavlov**, J. Vaitkus, M. Glaser, M. Moll, *Fluence and Anneal Dependent Variations of Recombination Parameters in Si Irradiated by 26 GeV Protons*, International conference Radiation Interaction with Material: Fundamentals and Applications, Kaunas, 2014.

Structure of dissertation. The research problems, scientific relevance and novelty, objectives of the research and practical importance are discussed within Introduction section. The statement defence as well as author

contribution are there determined in the Introduction chapter. In Chapter 2, the issues concerned with technological and radiation defects in the analyzed semiconductor materials and pulsed current signals in capacitor type particle detectors are briefly reviewed to ground motivation of this research. Chapter 3 is devoted to analysis of the main characteristics of the initial materials for sensor fabrication. There the measurement techniques are also briefly described. In Chapter 4, the dynamic models for description of sensor pulsed responses and results of the profiling of pulsed current signals in GaN detectors are presented. The tentative technologies for fabrication of GaN different type sensors, sensor operation characteristics and carrier drift/recombination parameters extracted from pulsed characteristics are discussed in Chapter 5. There, the appearance of polarization effects and characteristics of their relaxation are also discussed. The dosimetry sensors made of different type Si and their sensitivity to pion irradiations are discussed in Chapter 6. The general conclusions are presented at the end of dissertation.

II. The role of defects in semiconductor sensors - brief review of issues

2.1. Technological defects in diamond, GaN and Si

Physical properties of diamond make it an attractive material for optical and optoelectronic applications. Diamond has a wide range spectrum of optical transparency as compared with other solid materials. This range covers wavelengths from 0.22 μm to far infrared, excluding internal vibration modes of wavelengths from 2.5 to 7 μm. This allows to study defects in diamond crystals, their optical activity, electronic and vibrational transitions by employing transmittance spectroscopy. The band gap of diamond is about of 5.49 eV (Fig. 2.1). Mechanical and heat conductivity properties of diamonds play the important role in various fields of diamond applications [30, 31], as well. High material density is beneficial in fabrication of the high power/high frequency transducers and radiation tolerant particle detectors [32-35]. Boron (n –conductivity type) and phosphorus (p - type) doped diamond is suitable for fabrication of UV LED's, emitting wavelengths of 235 nm [33]. Mass production of LED's, however, needs well-developed and cheap technology for growth of the synthetic diamond crystals. Nowadays, two technologies dominate in synthetic diamond growth, as the HPHT and CVD techniques [9].

To evaluate quality of synthetic diamonds, the methods of the UV-VIS-NIR, FTIR and EDXRF spectroscopy are often employed. There a number of optically active centres (defects) had been revealed and classified, those determine the colour of diamond specimen [36]. The low-temperature PL measurements are commonly used for examination of tiny structure of spectra in advanced classification and certification of diamonds [10, 37, 38].

The transitional metal catalysts are specifically exploited in HPHT diamond synthesis technology, those are the main sources of metallic impurities serving as centres of rapid carrier recombination. The HPHT diamond crystals growth rate can be elevated by doping of zinc. However, this technique requires higher temperatures than HPHT process with conventional catalysts. Moreover, the excessive addition of zinc may act as a suppressant for the nucleation in diamond synthesis [39].

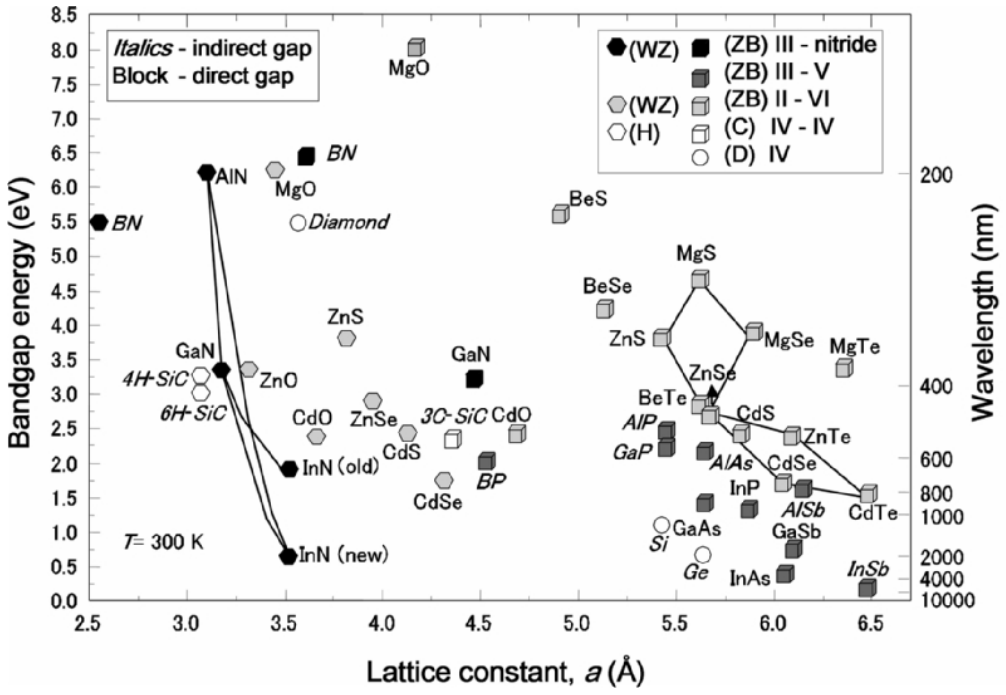

Fig. 2.1. The bandgap energy as a function of the lattice constant in wide-bandgap binary semiconductors, after [9].

Also the nitrogen is inevitable in precursors of HPHT diamond growth. As a consequence, the nitrogen aggregation rate depends on the presence of transitional metals [11, 12]. Thereby, large densities of metallic impurities and of nitrogen complexes are routinely present in diamond crystals grown by HPHT technique, those considerably modify electrical and optical properties of these materials. Nitrogen forms the optically active defects, such as the isolated atoms, polyatomic complexes and nitrogen complexes wit other impurities and crystal imperfections. Qualitative classification of the diamond specimen is often performed on the basis of the optical absorption within spectral range ascribed to vibrational modes of nitrogen and its complexes [30, 40]. As a rule, the metallic and nitrogen impurities are distributed non-uniformly [39, 41]. The excess carrier lifetime is one of the most sensitive parameters to electrically active defects in material. On the other hand, carrier lifetime is the main limiting factor for charge collection efficiency in diamond based sensors and detectors [6]. Thereby, control of the recombination parameters enables ones to reveal the distribution of the technological impurities and to separate the prevailing channels of radiative and non-radiative recombination. The special

regimes should be kept in growth of the high quality single crystals of diamond, to avoid defect clusters or even different material phase inclusions by applying the linear growth rate of crystal [11, 42, 43]. However, significant heterogeneity of the growth processes, formation of crystal phases of different morphology and inhomogeneous spatial distribution of various impurities, as nitrogen and nickel as well as their complexes, complicate formation of diamond single crystals [44, 45]. Therefore, production of sensors on HPHT diamond needs primary evaluation of material quality by using spectral and electrical characterization techniques. The more homogeneous bulk diamond material is obtained using CVD growth technology. Nevertheless, these CVD diamond single-crystal materials are considerably more expensive relative that of HPHT, and can preferentially be exploited for particular detector production.

Gallium nitride is a wide bandgap III-V semiconductor [46] (Fig. 2.1), which is a promising material for fabrication of the solar-blind photo-sensors and of particle detectors applied in high energy physics, radiation monitoring and other fields [46, 47]. The low leakage current, high luminescence efficiency and high tolerance of ionizing radiation are there attractive characteristics of GaN. However, defects introduced during crystal growth procedure affect functional characteristics of devices made of GaN material [47, 48]. The knowledge of parameters of the technological defects [49-51] is very important in prediction of operational characteristics (leakage current determined by deep levels, charge collection efficiency affected by shallow trapping centres, etc.) of detectors.

The spectroscopic methods are there highly effective tools for the investigation of these defects. Point defects include the isolated native defects, such as vacancies, interstitials, anti-site defects, impurities and their complexes in various combinations. Understanding of the role of these defects suggests the defect engineering means, applied within crystal growth and doping procedures, those are desirable in order to improve the performance and durability of devices made of these GaN materials [52-55]. Several

technologies of GaN crystal growth are wide-spread in formation of bulk and layered GaN structures. The high rate growth method is the hydride vapour phase epitaxy. The epi-layer is usually grown on sapphire substrate which is afterwards removed to get bulk wafer. Another epitaxial growth technique is metal-organic chemical vapour deposition on various substrates to obtain rather thin GaN layers for optoelectronics applications. Production of the low-temperature buffer layer on a sapphire substrate is a specific step to obtain high quality GaN thin films. Sapphire C-face (0001) substrates, determine a lattice mismatch of 16%, is widely used for the growth of GaN. The MOCVD GaN thin films are routinely grown on SiC, Si and GaAs substrates almost always using buffer layers [9, 13, 14]. The inevitable disordered domains appear at boundaries of GaN crystallites. This is the main reason in formation of edge dislocations arranged at these boundaries [15, 56-58].

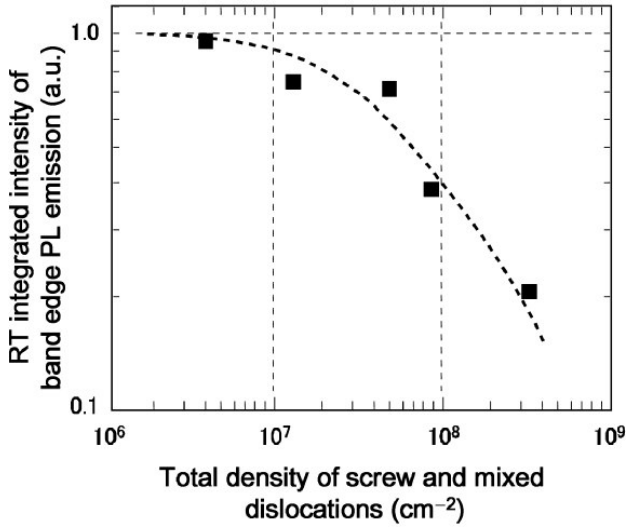

Fig. 2.2. Variation of the integrated PL intensity as a function of density of the screw and mixed dislocations in GaN:Si sample, after [9].

The rather high density of threading dislocations and the mosaic structure of epi-layers can significantly affect the excess carrier transport and recombination characteristics for the MOCVD GaN material. Dislocations and their densities (Fig. 2.2) are commonly controlled by X-ray diffraction (XRD) techniques. The electrical activity and spectra of deep levels (Fig. 2.3) introduced by various point defects are conventionally evaluated using deep

level transient spectroscopy means, which nevertheless require the presence of p-n junction or a Schottky contact [59-61].

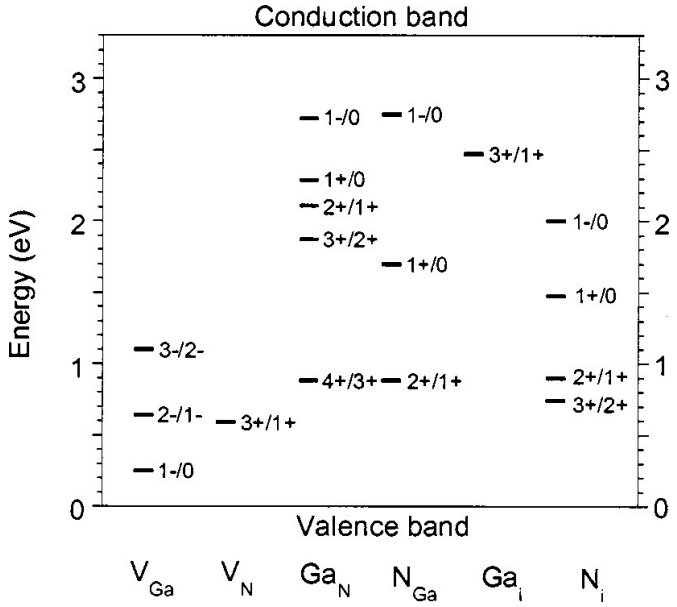

Fig. 2.3. Deep levels within bandgap of GaN associated with native defects, after [52].

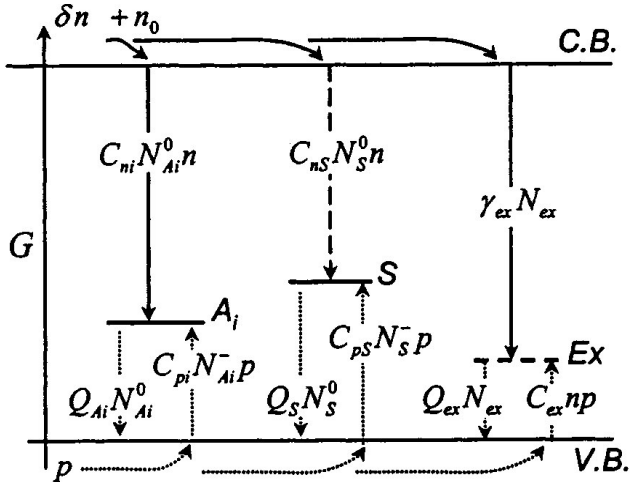

Fig. 2.4. A scheme of radiative transitions in *n*-type GaN, responsible for various PL spectral bands, after [52].

These deep levels determine different spectral bands of radiative transitions (Fig. 2.4). The deep levels involved into non-radiative transitions can affect the luminescence efficiency [62-67], important for LED (light emitting diode) formation. Wide nomenclature of extended and point defects

had been revealed, e.g. [68, 69], in GaN materials produced by different technologies. However, manifestation and the role of various defects are specific for different device structures. For instance, the short carrier lifetime determined by carrier capture to deep traps can serve for fast response of radiation sensors, however, carrier trapping and thermal emission decreases the sensitivity of detector and increases the leakage current. There, study of photo-activation spectra combined with monitoring of carrier lifetime can be a direct approach for discrimination of the predominant defects; those determine the carrier-pair generation rate and charge collection efficiency. Therefore, the relevant material characterization means should be smartly combined with device formation steps to get sensors of proper performance.

A lot of similarities are within performance of diode detectors and solar cells in sense of barrier formation, governing of the depletion layers and the role of intrinsic defects in degradation of device characteristics. The efficiency of solar cells and radiation detectors considerably depend on the technological defects introduced during formation of junctions, of passivation layers and electrodes [70]. These defects as usually act as carrier trapping centres in the bulk and at surface of devices. As the alternative to the conventional silver based technologies in solar cell production, usage of copper electrodes is an attractive way in order to cheapen the commercial fabrication of solar cells. However, the problem of copper diffusion into the base region appears where metallic impurities are fast carrier traps and can make meta-stable complexes with dopants [71-72]. This problem can partially be solved by forming the diffusion barrier, which prevents copper in-diffusion [73-75]. The formation of copper electrodes on a solar cell is additionally complicated by the necessity to combine a deposition of several metals. These technological procedures should be precisely controlled to avoid a contamination of the active device layers by carrier capture and generation centres. The high conductivity Si material base is commonly used in production of the modern solar cells. The problem of the usage of the standard techniques and instrumentation (such as the capacitance deep level transient spectroscopy [76-78]) then appears in precise control of

the introduced defects, when heavily doped materials are exploited. The high conductivity base region leads to a large barrier capacitance of a junction. This requires the extremely small area samples for the application of the standard C-DLTS instruments. Consequently, the enhanced leakage current on sample boundaries is inevitable for the small area samples. Therefore, it is important to develop the alternative methods for the defect spectroscopy in the high conductivity junction structures, to directly control a relatively low concentration of metallic impurities. The solar-cell grade silicon materials exploited in mass-production of photo-cell panels can then be an appropriate modelling matter for emulation of features of heavily irradiated particle detectors and for validation of testing techniques. In addition, the solar cell standard Si materials can be the cheap sensors employed for dosimetry of harsh areas of the particle accelerators of high luminosity.

2.2. Radiation defects in GaN, CdS and Si

Crystalline GaN is a promising material for creation of radiation hard particle detectors capable to operate in harsh areas of particle accelerators [48, 79-81]. Bombardment by high-energy particles of the gallium nitride material alters the structure of the material by producing a lot of defects of various species, those affect operational characteristics of detectors [47, 82-88] Moreover, GaN crystals show rather efficient luminescence properties under excitation by ultraviolet (UV) radiation [89-92]. Thereby, GaN material can be employed for fabrication of dual-purpose sensors, which are able to operate both as the scintillation and charge collection detectors. However, efficiency of such detectors and their functionality is investigated insufficiently.

Polycrystalline cadmium sulfide layers and heterojunctions are of great interest due to their unique properties in variation of composition and their potential applications in numerous fields [93], such as sensors in the X-ray imaging devices, [94] solar cells [95], super-ionic conductors, photo-detectors as well as photo-thermal converters [96-99]. Much research interest comprises the possible applications of CdS in fabrication of various optoelectronic

devices based on CdS polycrystalline films. Polycrystalline CdS can also be exploited as a cheap scintillating material for visualization of particle beams and for dosimetry. However, radiation hardness of the polycrystalline CdS is poorly investigated. In addition, the heterostructures Cu_2S-CdS formed on these polycrystalline CdS layers [100, 101] show an opportunity to employ the heterostructures as the particle sensors. Thereby, such a sensor could be suitable for synchronous detection of the optical (acting as a scintillator) and electrical (as a charge collection sensor) responses.

Particle detectors based on Si pin structure are commonly employed in high energy particle experiments for rapid and reliable detection of high energy particles [5, 6]. However, large density of radiation induced defects acting as carrier traps affect the detector functional parameters by reducing the charge collection efficiency [5, 6], increasing the leakage current [7], and consequently modifying the pulsed transient waveforms [8]. This necessitates a deeper study of peculiarities of carrier recombination channels attributed to radiation defects of large density. Carrier thermal generation and trapping parameters are the most important in evaluation of the performance of particle detectors operating at high fluences. Therefore, new techniques are desirable for the reliable *ex situ* and *in situ* spectroscopy of large density traps when traditional methods, such as DLTS, become non-applicable. Determination of the spectral signatures (such as activation energy, capture cross-section, etc.) of the dominant radiation traps and of their variations during irradiation is important in order to clarify the main reasons of the degradation of particle detectors under heavy irradiations. This is also relevant in search of methods for the enhancement of radiation tolerance of particle detectors. Study of pions, their impact on the material, is of great interest. During high-energy physics experiments performed on the LHC, it is very important to monitor background radiation in a wide range. This necessitates applying of the appropriate monitoring methods, specifically using the contact-less, fast and remote measurements techniques. Furthermore, the concept of the evolution of defects

in the crystal, their stability under the impact of the exotic particles, like pions [17,102,103], is examined rather poorly.

2.3. Issues in analysis of the Si, GaN and diamond sensor signals

Si based particle detectors are commonly made of high purity and large resistivity material [104]. These detectors should be radiation tolerant up to an extremely large fluences of $>10^{16}$ cm^{-2}. However, the effective doping density N_{eff} of the material varies during detector operation due to charged radiation defects inevitably introduced. As a result, the charge collection efficiency, being the most important characteristic of electrical detector functionality, is reduced [105]. It is necessary to control the spectra of the introduced radiation defects, to predict the changes of detector parameters. The standard and widely used spectroscopy technique is capacitance deep level transient spectroscopy (C-DLTS) which is a sufficiently sensitive and straight spectroscopy technique for characterization of deep radiation traps [77]. However, the standard application of C-DLTS is limited by the trap concentration, which should not be larger than the doping density [76]. The measurement of generation current (I-DLTS) is an alternative option to the DLTS technique, which can be approved for the spectroscopy of high density carrier traps in silicon detectors made of large resistivity material [78]. An electrical filling of deep traps by manipulating the carrier injection pulses exploited in standard DLTS techniques can be inefficient for the radiation affected junction of the sensors. Therefore, an additional modification of DLT spectroscopy is implemented by using an optical carrier injection leading to the optical current DLTS (O-I-DLTS) regime [76]. Optical excitation employing the laser or LED light illumination fills both types of the majority and minority carrier traps. However, it is impossible to distinguish the current components ascribed to the majority and minority carrier traps within the generation current transients. This is a disadvantage for usage of O-I-DLTS [106].

Analysis of particle detector operation is commonly performed on the basis of consideration of the injected charge drift induced Ramo's current [6, 26, 27]:

$$i_A = \frac{dQ_A}{dt} = -\frac{e}{V_A}\frac{dV_e}{dt} = -\frac{e}{V_A}\left[\frac{dV_e}{dX_e}\frac{dX_e}{dt}\right], \tag{2.1}$$

where dX_e/dt stands for velocity of the moving charge, and $(1/V_A)\times(dV_e/dX_e)$ is the weighting field. The current transients are widely examined in order to reconstruct an electric field distribution within the active layers of particle detectors [107-113]. In the heavily irradiated detectors, a sensor signal can be considerably modified by the injected charge trapping due to radiation defects introduced under long irradiation exposure of the particle detectors. Profiling of the carrier recombination centres [114, 115] and of the injected charge drift velocities [116-120] can be performed by the cross-sectional scans of the photoconductivity and drift current transients. However, a simplified analysis of the drift current transients in detector junction structures is usually applied for the interpreting of the detector signals. The most general consideration is based on the Maxwell's equations for matter. Static and dynamic approaches exist to describe the transient electrical characteristics in matter [121]. The static theories are devoted to description of a drift velocity versus electric field characteristic. The common feature of static and quasi-steady-state approaches is a consideration of only the static and uniform electric fields. The most general dynamic theories deal with the charge transport properties under dynamic conditions when electric field varies in time and space. However, in most of approaches in analysis of the operational characteristics of semiconductor devices, the paradigm of drift current description is based on consideration of the first Poisson's equation with either the continuity equation or drift-diffusion current model, which actually can be ascribed to quasi-steady state approaches. The first Poisson's equation calibrates the charge in the system, but an electric field of an injected drifting charge is often ignored. Charge balancing through the changes of image charge leads to an appearance of electric fields varied in time and space. An example can be a consideration

of recombination models and continuity equation, where necessary to precisely include the balance of charged carrier flows, of group velocity and of electric fields. The main inconsistency of such models appears due to non-calibrated potential in field equations, i.e., by ignoring of the image charge. The main relation of electrostatics requires the unambiguous correlation between the charge and potential. This correlation is calibrated by the second Poisson's integral including impact of the image charge, which is actually provided by external source. For non-calibrated consideration of the drift-diffusion approximation, this approach is only valid for partial description, for instance, drift-diffusion can be applied for description of current in the transitional layers nearby the field discontinuity interfaces (e.g., electrodes) after rapid transitional processes of field discontinuity drift are finished or balanced. Actually, the widely used drift-diffusion and the hydrodynamic approaches are based on consideration of the convection current, while in pulsed detectors routinely containing the depletion regions, the displacement current component is prevailing. The Ramo's derivation gives an algebraic form of current expression obtained from the principles of simultaneous conservation of the electrostatic energy or reciprocity principle, of charge and of charge momentum for the complete closed circuit with fixed electrodes. It has been proved that equal fields superpose in modification of time varied current due to a drifting charge. These fields are time and drifting charge position dependent. Thereby Shockley-Ramo's theory should be ascribed to dynamic models. Usage of Ramo's current expression with ignored electrostatic induction field leads usually to a static model in description of drift velocity.

In addition, the analysis of transient currents [20-25] due to moving charges is commonly based on the Shockley-Ramo theorem [26, 27]. Alternatively, current density changes dependent on applied voltage can be simulated based on a system of Boltzmann equation, e.g., [28], using conservation laws for carrier concentration, momentum and energy. However, the latter approach is acceptable for simulation of quasi-steady-state regime, and, as emphasized in [29], "an analysis based on the Boltzmann equation with

a rigorous treatment of the collision integral is prohibitive" in the dynamic theories concerned with the transport properties under dynamic conditions, *i.e.*, when the electric field varies in time and space. Therefore, the dynamic models including electric field variations are needed for deeper understanding of the transient currents in particle and photo-detectors and for more precise description of sensor responses.

Radiation-induced defects are one of the most significant limiting factors for the operational characteristics of particle detectors during high fluence irradiations. Therefore, radiation harder materials such as GaN [122,123] and diamond [124, 125] are considered as promising candidates for the design of the radiation tolerant detectors operational in the harsh environment of the future high brightness hadron collider experiments (Fig. 2.5).

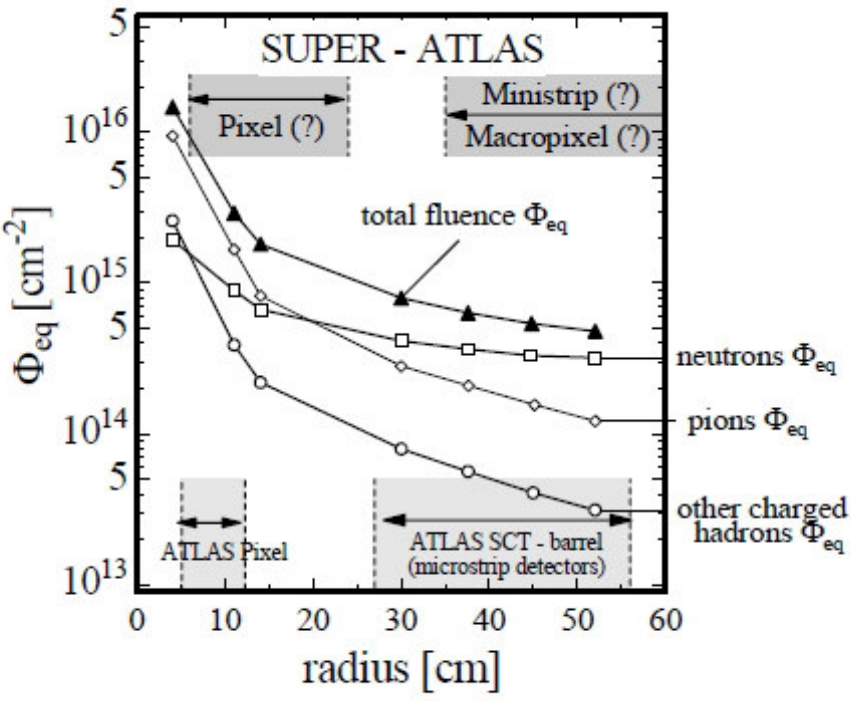

Fig. 2.5. Hadron fluence expected in the inner SUPER-ATLAS detector after five years of operation, [123].

GaN crystalline material of a proper quality is usually obtained by the MOCVD technique, and the as-grown epi-layers are rather thin. It has been evaluated that carrier pair generation by high energy protons comprises efficiency of 40–80 pairs per μm length of the device active width per proton

[123]. The internal gain implemented through multiplication processes is also a good alternative to compensate for device performance degradation caused by radiation defects and reduction of carrier lifetime [126]. Additionally, the thermal noise current is considerably reduced in wide band-gap materials. Several attempts to generalize a simple Ramo's approach to multi-electrode and arbitrary space-charge field distribution systems had been made. An additional kinetic equation should be considered to determine the instantaneous velocity, as a motion velocity of charge is only postulated in Shockley-Ramo's derivations. However, in most applications of Ramo's theorem, the consideration of motion velocity, which should incorporate the induction (image) charge field, is ignored. Ignoring of the image charge field renders the Ramo's current expression not practically applicable for analysis of detector signals. The motion velocity of these carriers varies during carrier drift, and it is determined by the changes of charge on the electrode. The charge, supplied to electrodes [27] by an external source (circuit) actually serves as an image charge for the moving charge within an inter-electrode space. The field inhomogeneity effects on boundary of electrode of a fixed dimension can also be important, especially for small drifting charge. More complications appear within the consideration of a kinetic equation, when the injected charge can vary due to charge traps inside the inter-electrode space. These traps in dielectric material can be a reason for charge localization and local charge generation. The mentioned brief review of problems in description of fast response sensors imply the necessity for development of the more comprehensive and adequate models in description and interpretation of advanced sensor signals.

III. Characterization techniques and characteristics of sensor materials

Adequacy of detector signal processing considerably depends on characteristics of materials exploited in formation of sensors and on variations of these characteristics during operation in harsh environments of irradiations. Therefore, the initial stage is the material precursory characterization for deeper understanding of peculiarities and evolution of sensor signals. This requires the concerted measurements of various material parameters using relevant techniques to have the comprehensive characteristics of materials employed in fabrication of sensors. A brief description of the examined samples, the invoked characterization techniques and of the most important characteristics is presented within this chapter. Here, the more detail discussion on the characteristics of the initial materials: diamond and GaN, while characteristics of the examined polycrystalline CdS structures are published in more detail within articles [127, A5].

3.1. Characteristics of synthetic diamond

3.1.1. Materials and samples

The HPHT diamond single crystals, synthesized by the high pressure (4.5–5.0 GPa) and high (1350–1450 °C) temperature gradient technology [128] using the Ni–Fe–C liquid solvent/catalyst carbon metallurgy system, were investigated. Growth was carried out of about 65–70 h. The solvent/catalyst system comprised the 70% Fe and 30% Ni metals in crystal growth cell, respectively. A 250–300 μm dimension pad of synthetic diamond with (100) plane, oriented towards the carbon source, served as a seed. Growth regime was controlled by measurements of electrical power consumption. These power consumption parameters are correlated with temperature by additional calibration measurements with precision of ±15 °C. The as-grown yellow-colour single crystal of 1.22 ct weight had a cube-octahedral frame (Fig.3.1a).

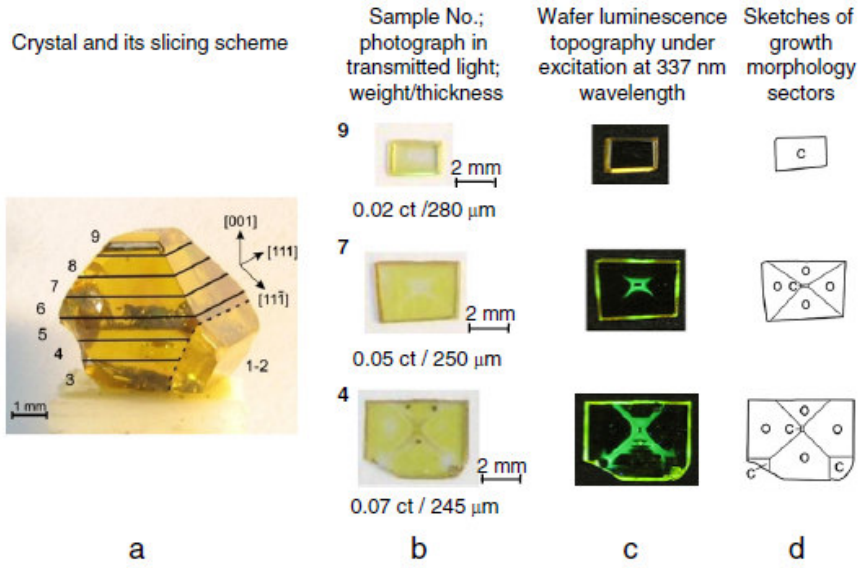

Fig. 3.1. a – The as-grown crystal and a scheme of slicing of the wafer samples; b – weight and dimension parameters and photographs of the as-polished diamond wafers taken in transmitted light; c – the fluorescence topography registered under excitation by ultraviolet light; d – the idealized sketches of the growth-morphology sectors. Here, "C" denotes cube sectors, "O" indicates the octahedral sectors.

The octahedral growth planes prevailed on the as-grown crystal, while a cube growth sector can clearly be observed on the crystal-top plane situated oppositely to a seed. The cube growth sectors on the side-planes of a crystal were not clearly observable. The as-grown crystal contained a crack, denoted in Fig.3.1a by a dashed line contour, in parallel to the lower octahedral plane. Wafers No. 1 and No. 2 were cut in parallel to this line. The samples from No. 3 to No. 9 were prepared by slicing of the residual part of the crystal into wafers across the plane (001) in parallel to the crystal base. The 250–500 μm thick two-side mechanically polished wafers contained surface roughness less than 20 nm, as inspected by an atomic force microscope. A scheme of wafer sample slicing is presented in Fig. 3.1a. Wafers No. 4, No. 7 and No. 9 have been examined in this work, in order to study distribution of the grown-in defects and impurities by mapping the lateral profiles of carrier lifetime. Dimensions and weight of each wafer are denoted in Fig. 3.1b. The photographs of each sample placed on a white sheet have been taken in transmitted light. These photographs are illustrated in Fig. 3.1b. The yellow

colour inhomogeneity and the contours of growth morphology sectors can be estimated from these photographs as suggested in [39]. For wafer No. 4, the complicated projections of different morphology sectors grown from a seed [39, 41] and metallic inclusions are also observed in Fig. 3.1b.

3.1.2. Microscopy and composition characteristics

The microscopy imaging has additionally been performed for selection of wafer areas containing the inherent macroscopic defects using a microscope Olympus BX51. A few of these microscopy images are illustrated in Fig. 3.2. Their origin has been identified by scanning electron microscopy (SEM) imaging combined with the energy dispersion X-ray spectroscopy (EDXS) using instruments SEM CamScan Apollo 300 and EDX Oxford Instruments spectrometer, respectively.

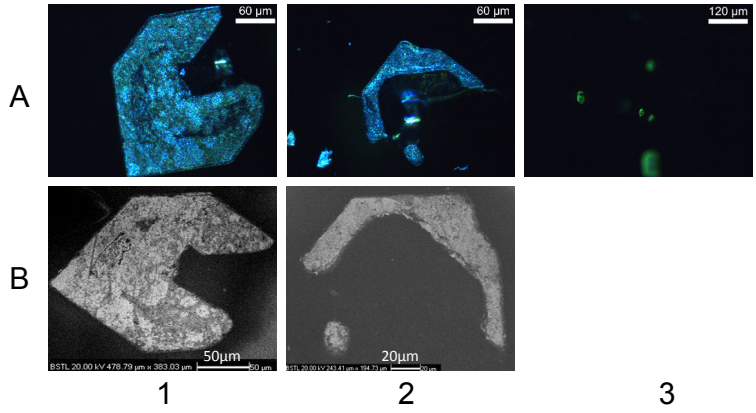

Fig. 3.2. A- Optical microscopy images taken in dark field for the characteristic locations on a wafer No. 4: 1- the metallic phase inclusion, 2 - the macroscopic metallic precipitate, 3- small platelet defects. B – SEM images for the observed defects 1 and 2 [A8].

It can be deduced from examination of wafers in transmitted light and by fluorescence imaging (Fig. 3.1) that wafer No.4 contains the most expressed variety of growth-morphology sectors. The most expressed inhomogeneity of yellow-brownish colour lateral distribution in transmitted light and of intensity of yellow-green luminescence imply plenty of defects. Therefore, analysis of defects in this wafer sample No.4 has been performed and discussed in detail.

It has been unveiled the different areas of a crystal which contains inherent inhomogeneities, namely: a cross-shaped defect distribution (Fig. 3.3 Aa), the small metallic precipitates (Fig. 3.3 Ab), the metallic phase inclusions (Fig. 3.3Ac and Ad), highlighted by the microscopy imaging. The microscopy image photographs were taken in the sample area where accumulation of the cross-shape defect distribution is observed under UV excitation (Fig. 3.3 Aa). Here, the superimposed projections of the cube, trapezohedral and octahedral growth-morphology sectors with different orientations can be implied according to the idealized schemes of the growth-morphology sectors [39,129,130]. The cross-shaped accumulation of defects in the central area of wafer No. 4, which is highlighted by the brownish-yellow colour in the transmitted light photograph, is inherent for the nickel-rich diamond material [41]. The enhanced scattering of light in this area can be deduced from the optical microscopy images. The scattering of light, deduced from Fig. 3.1. and within optical microscopy image of Fig. 3.3 Aa, implies clustering of defects of dimensions close to the light wavelengths <1 μm. A pedestal of the enhanced IR absorption within FTIR spectra hints that dimensions of scattering centres can be extended up to 10 μm. Thus, light scattering centres of dimensions in the range of 1-10 μm can be interpreted as non-dissoluted particles of the metal solvent/catalyst matter trapped into a crystal during the initial growth phase. This hypothesis is supported by the structure of the microscopy image (Fig. 3.3Aa) taken under ultraviolet light illumination, where the central black spot of small area (surrounded by the cross-shape contour of the enhanced intensity luminescence) can reliably be ascribed to a cube morphology sector which seems to be rather free of impurities. The cross-shape contour of enhanced intensity of the yellow-green luminescence can be attributed to Ni impurities at the boundaries of the octahedral sectors. Ni impurities are predominantly concentrated within areas of the octahedral sectors [130].

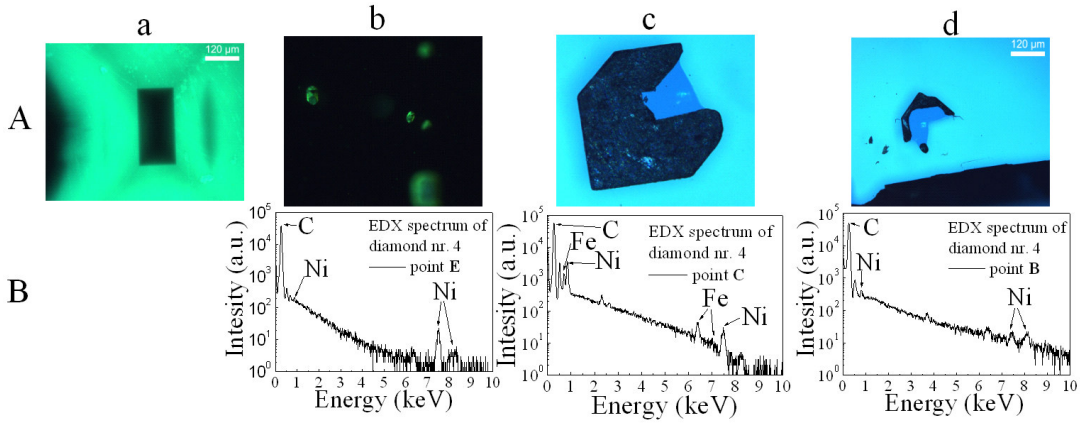

Fig. 3.3. A-Optical microscopy images: a- of the central sector of the sample No. 4, b- of the dispersed precipitates, c- of the iron-nickel inclusion, d- of nickel inclusion. The images were registered using the ultraviolet light illumination (a, b) and bright-field (c, d) regimes. B- EDXS spectra registered for the respective optical microscopy images [A8].

The larger precipitates of the 20-60 µm dimensions have also been highlighted in microscopy images taken using ultraviolet light illumination (Figs.3.3Aa-Ab) and the bright-field regime (Fig. 3.3Ac-Ad). Different inclusions of dimension of about 200 µm (Fig. 3.3Ac) and 50 µm (Fig. 3.3 Ad) have been resolved within wafer area using the bright-field regime. The origin of the metallic traces of the catalysts/solvent mixture trapped in the diamond crystal and of macroscopic defects had been identified by examination of the SEM images combined with EDXS. The inherent EDXS spectra are illustrated in Fig. 3.3B, correlated with the macroscopic defects highlighted by optical microscopy. The different metal ascribed EDXS peaks, analyzed by software installed within EDXS instrument, are denoted in Figs. 3.3B.

3.1.3. Spectral characteristics

3.1.3.1. FTIR spectra

Evaluations of the total concentration of the nitrogen ascribed defects in the central area had been performed using methodology described in [132-135] based on FTIR measurements. Fourier Transform Infrared (FTIR) spectroscopy was performed using Bruker Vertex 70 spectrometer with spectral resolution of 0.5 cm^{-1}. The transmittance I/I_0 had been examined in

the spectral range of 400- 4000 cm^{-1} wavenumbers keeping an aperture of 1.1 mm diameter. Values of the absorption coefficient α at fixed wavelength can routinely be determined [136] as $\alpha=d^{-1}\ln I_0/I$. However, for more reliable evaluation of nitrogen impurity concentration, the calibration method has been involved. The concentrations N of the A, C and C+ defects were calculated from the absorption coefficients α at wavenumbers of 1282, 1130 and 1332 cm^{-1}, respectively [132-135]. In order to determine the absorption coefficient for the single phonon absorption region, the absorption coefficient at 2030 cm^{-1} wavenumber has been used as a standard, where α_{2030} is accepted to be 12.8 cm^{-1} [131]. Concentrations of the A, C and C+ type defects are calculated by using the relations N_A-$_{1282}$(ppm)= $(\alpha_{1282}/\alpha_{2030})\times12.8\times16.5$, $N_{C\text{-}1130}$(ppm) = $(\alpha_{1130}/\alpha_{2030})\times12.8\times25$, $N_{C+-1332}$(ppm)= $(\alpha_{1332}/\alpha_{2030})\times12.8\times5.5$ [132-135], where N_A-$_{1282}$, $N_{C\text{-}1130}$ and $N_{C+\text{-}1332}$ are the concentrations of the A-, C- and C+-defects, respectively. Thereby, the total concentration of the nitrogen ascribed defects in the central area of a definite wafer sample has been determined to be 2×10^{19} cm^{-3} in wafer No.9, 4×10^{19} cm^{-3} in wafer No.7, and 4.4×10^{19} cm^{-3} in wafer No.4, respectively. Values of defect concentration within wafer periphery region comprise a half of the concentration value in the centre of wafer.

Detailed Fourier Transform Infrared (FTIR) spectroscopy in transmission mode has been performed on wafer No. 4 by using FTIR spectrometer Bruker Vertex 70 equipped with Bruker Hyperion 3000 microscope. The FTIR scans were carried out within local areas selected by a knife-edge aperture from 20×20 μm^2 to 200×200 μm^2. These areas correspond to micro-volumes of different material quality and have been used to highlight inclusions of metallic phase precipitates. The extracted values of absorption coefficient have been used for evaluation of the local concentration of the nitrogen impurities. Precision of separation of the clearly distinguishable areas, where a difference of the impurity concentration can reliably be separated, is determined by an aperture used in measurement of FTIR spectrum ascribed to the local area. Therefore, the line between the points M-E, where separation of aperture areas

is reliable, has been taken for detailed examination of changes in carrier lifetime correlated with nitrogen impurity concentrations.

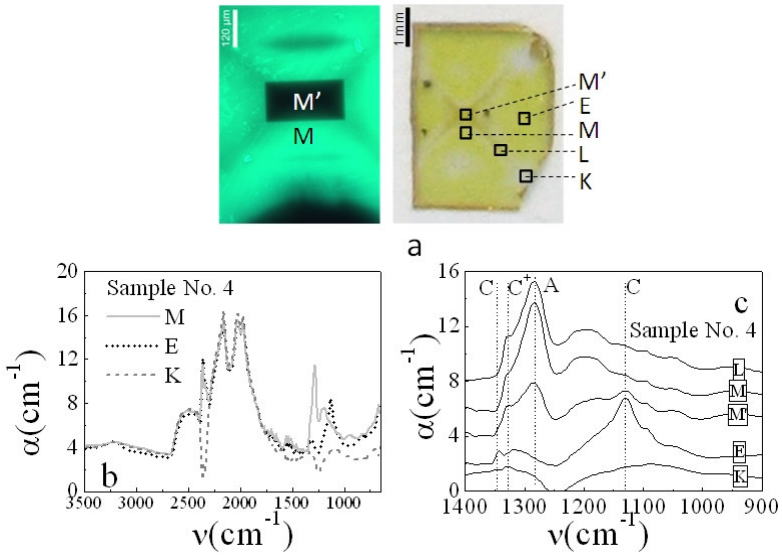

Fig. 3.4. FTIR transmission spectra measured on sample No. 4 scanning different locations of wafer area. a- Attribution of the location points scaled with a microscopy image of a wafer fragment in the central area taken under ultraviolet light excitation (left panel) and a wafer photograph in transmitted light (right panel). b- FTIR spectra over 400 -3500 cm^{-1} spectral range for several denoted points on wafer. c- Comparison of the structure of spectra (shifted by 2 cm^{-1} across the ordinate for values of the absorption coefficient) recorded for different points within wafer area: for points M (cube and octahedral sectors) and M' ({001}cube morphology sector) correspond to the central area of the cross-like luminescence image; K - for cube {100} morphology sector at the corner of wafer; L- for the boundary of two octahedral sectors on the cross-like line superimposed with {100} cube sector, E- for octahedral {111} sector [A8].

The spectra of the absorption coefficient recorded for different locations within wafer No. 4 are illustrated in Fig. 3.4. The attribution of the location points is sketched in Fig. 3.4a. Here, a microscopy image of a wafer fragment in the central area taken under ultraviolet light excitation and a wafer photograph in transmitted light may serve as a lateral coordinate scale. The spectra over 400 -3500 cm^{-1} spectral range are shown in Fig. 3.4b. These spectra are displayed (in Fig. 3.4c) for the narrower range of 1400-1000 cm^{-1} of wavenumbers with spectral peaks ascribed (according to Refs. [39, 130, 132] nomenclature) to the nitrogen defects of various types. The peaks are

here highlighted and attributed to: C^+ ($1332cm^{-1}$), - a charged isolated-substitutional-nitrogen; C ($1130cm^{-1}$), - a neutral isolated–substitutional-nitrogen; and A ($1282cm^{-1}$), - the aggregate of a pair of the nearest-neighbour substitunional nitrogen atoms.

These spectra have been recorded in sample No. 4 for several specific locations: spectra for point M (superimposed cube and octahedral sectors) and M' (cube morphology sector, rather narrow range) correspond to the central area of the cross-like luminescence image; K – for cube {100} morphology sector at the corner of wafer; L – for the boundary of two octahedral sectors on the cross-like line, E – for octahedral {111} sector. The spectrum attributed to the point E has been obtained for the rather homogeneous area of material aside the cross-like image; point K corresponds to the non-luminescent image of a wafer area where no clear defects can be imaged.

The observed changes in FTIR spectra could be interpreted as follows. For an area overwhelmed by a scan aperture at M' point, a third of the probed area is within a dark square (left panel of Fig. 3.4a). This part of probed area is non-luminescent and covers a cube morphology sector. Consequently, the concentration of nickel impurities is there extremely small in this area. Therefore, the aggregation of nitrogen is weak in this region relative to the octahedral sectors where a concentration of nickel is elevated. This leads to the predominant formation of C-type neutral isolated-substitutional-nitrogen defects. The FTIR peaks ascribed to the A and C^+ defects appear from the superimposed area of the octahedral sectors. For the M point localized within octahedral sector nearby M', the trapped nickel impurities accelerated the aggregation of nitrogen into A-type defects of pairs of the nearest-neighbour substitunional nitrogen atoms, which there are the prevailing defects.

Luminescence of the enhanced intensity in vicinity of M point indicates the nickel-rich sectors. The nickel mediated formation of C^+ charged nitrogen defects corroborates also this hypothesis. The scanned L point is located on

the shoulder-line in the cross-like defect distribution picture. This L point covers the octahedral nickel-rich sector. Therefore, the structure of a FTIR spectrum recorded in the L area is similar to that obtained for M point. However, there appears the less concentration of the nitrogen ascribed defects. A little bit less luminescence intensity in the range of L point could be a motivation for a reduced concentration of the nitrogen impurities. It can also be assumed that the growth rate was lower during formation of the diamond crystal in vicinity of L point and the lower concentration of nitrogen was trapped. The FTIR spectrum, registered at E point, is typical for the Ib diamonds. The C-type defects prevail there. The area at the E point is non-luminescent. This indicates the reduced concentrations of nickel impurities, and the A- and C^+ - type defects are non-resolvable in FTIR spectra recorded for this range. For K- point at corner of the wafer with inherent colourless and non-luminescent material ascribed to cube morphology sector, the concentration of nitrogen ascribed defects is below the resolution limit in registered FTIR spectra.

Table 3.1. Concentration of nitrogen impurities evaluated from FTIR spectra, recorded for different locations within surface area of wafer No. 4 using an aperture of 20×200 μm^2, and the ~1×1 mm^2 aperture averaged values in wafers No.7 and No. 9.

Defect type	Location point within wafer No.4			Wafer No.7	Wafer No.9
	E	M	K	Central area	Central area
	Defect concentration $\times 10^{18}$ cm^{-3}				
C	22±2	nr	nr	3.6±1	9.1±2
A	nr	23±2	nr	37.0±3	11.0±2
C^+	1±1	3±1	nr	1.4±1	nr

Values of concentration of the nitrogen impurities being in different crystalline defect forms, extracted from the FTIR absorption spectra, are listed in Table 3.1, where local values of the concentration for different type defects in wafer No.4 are also presented. The largest concentration of nitrogen

ascribed defects is localized at the centre of diamond wafer No. 4 and on the cross-like lines. The C- type defects prevail within the rather homogeneous area of material aside of the cross-like image. There, the A-type defects have not been detected. The inherent defect concentration values are obtained to be of about (1-23)×10^{18} cm^{-3}, while in several areas the concentration of the identified type (A-C) defects is below the resolution limit (i.e. non-resolvable – nr). The integral concentration of the nitrogen attributed defects in wafer No.4, evaluated using a sum of FTIR peaks and averaged over central area of > 1×1 mm^2, is about of (47±3) ×10^{18} cm^{-3}. Values of concentration of the nitrogen attributed defects in the central area of wafers No.7 and No.9, evaluated from FTIR spectra peaks using a larger (of 1 mm dimension) aperture, are also presented in Table 3.1.

The revealed defects and their lateral distributions are important in selection of suitable wafer fragments for fabrication of fast-response sensors.

3.1.3.2. Pulsed photo-ionization spectra

The pulsed photo-ionization spectra have been examined by using microwave probed photo-conductivity transients under spectrally tuned 235-9000 nm excitation pulses generated by an optical parametric oscillator.

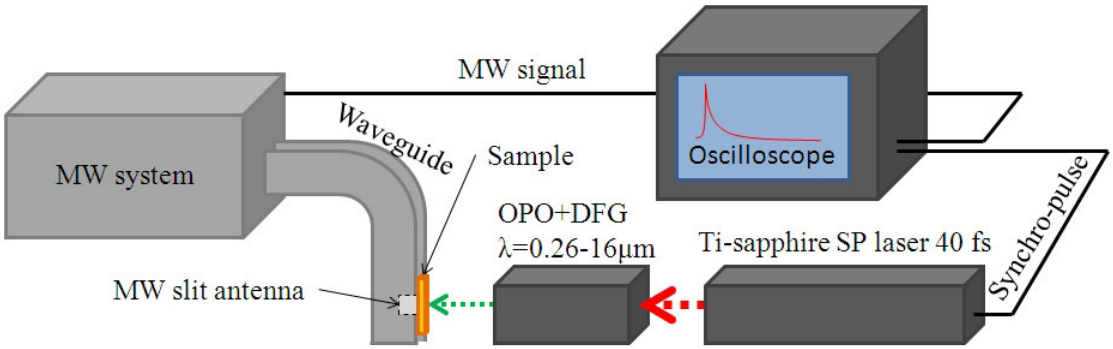

Fig. 3.5. A scheme of the experimental arrangement for pulsed photo-ionization spectroscopy measurements.

The generalized sketch of the pulsed photo-ionization spectroscopy arrangement is illustrated in Fig. 3.5. The excitation 40 fs pulses of tunable wavelength were generated by an optical parametric oscillator (OPO) pumped

by a Titanium: Sapphire laser. The MW-PC response [71, 115, 137] at fixed excitation wavelength has been detected by using a coaxial needle-tip MW probe. The signal recording scheme contains a balanced microwave bridge circuit. The photo-response signal is recorded by a digital 1 GHz oscilloscope Tektronix TDS-5104. The microwave signal actually represents the material conductivity $\sigma(t)=\sigma_0+\Delta\sigma(t)$ transient, which amplitude $U_{MW\text{-}PC}(t)\sim\Delta\sigma/\sigma$ [71] is proportional to the excess carrier concentration $\Delta n(t)\sim\Delta\sigma(t)$ generated by photo-ionization at fixed wavelength. The MW-PC transient additionally represents a carrier decay characteristic related to electronic transitions attributed to a definite deep level involved into photo-ionization processes at fixed excitation wavelength. To avoid non-controllable filling of deep levels, a spectrum is routinely measured starting from the longest excitation wavelengths.

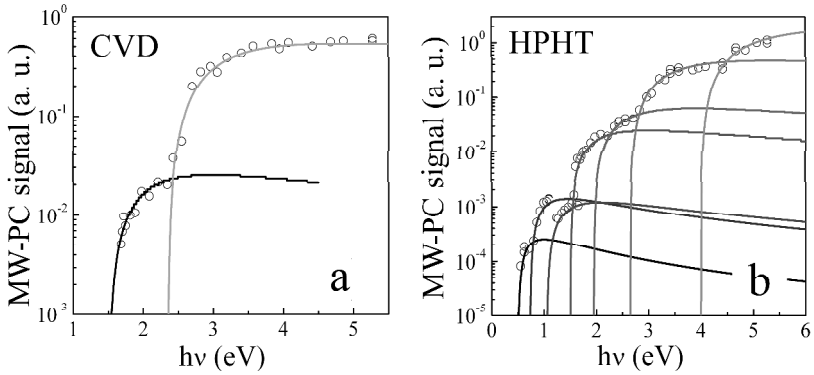

Fig. 3.6. Pulsed photo-ionization spectra obtained on CVD (a) and HPHT (b) diamond samples, respectively. Solid lines represent the simulated spectral steps using Lucovsky's model.

The pulsed photo-ionization (PPI) spectra, measured in the photon energy range of 1.7–5.3 eV for CVD diamond (a) and of 0.5–5.3 eV photon energy range for HPHT diamond samples (b), respectively, are illustrated in Fig. 3.6. The step-shape structures of the PPI spectra were observed in diamond samples grown by both CVD and HPHT technology. These spectral steps have been fitted (solid lines in Fig. 3.6) using Lucovsky's model [140]. By using fit parameters for every PPI spectral steps, the threshold photo-ionization energy values have been extracted.

Table 3.2. Threshold activation energy values, extracted by using Lucovsky's model, and assignment of defects.

	Photoactivation energy (eV)	Defect type
HPHT diamond	0.52±0.05	a-C [138]
	0.74±0.06	a-C [138]
	1.1±0.1	a-C [138]
	1.5±0.1	a-C [138]
	2.0±0.1	N-V [139]
	2.7±0.1	N-VN_iV-N [44]
	4.0±0.1	N_i, N_2-VN_i-N_2 [44]
CVD diamond	1.5±0.1	a-C [138]
	2.4±0.1	N subst. [44]

Values of the threshold photo-activation energy, extracted for different spectral steps using simulations by Lucovsky's model, are listed in Table 3.2. These photo-activation energy values have been assigned to defects, according to existing literature. The shallower levels, with photo-activation energy below 1.5 eV, have been ascribed to the a-C defect [138]. The activation energy of 2.4 eV has been assigned to the nitrogen substitutional defect [44]. A nitrogen-vacancy, with activation energies of 2.0 eV and of 2.7 eV, and the nickel-related deep levels, with activation energy of 4.0 eV, respectively, have been identified for HPHT diamond. Nitrogen is present as an unavoidable impurity in synthetic diamond while the nickel impurities are commonly incorporated within HPHT diamond, synthesized using a nickel-containing alloy catalyst-solvent. The nitrogen and nickel impurities, detected by FTIR and ESR spectroscopy, compose with vacancies the deep photo-active centres, resolvable by PPI spectroscopy.

3.1.3.3. Spectra of time resolved photo-luminescence

The PL light is collected from the area with a normal directed towards a bisector between the incident and the reflected UV light beams (Fig. 3.7). The UV filtered PL light is focused onto a slit of a MDR-23 monochromator. The PL light is dispersed using a grating monochromator, and the PL pulsed signal is detected by a Hamamatsu H10721 photomultiplier with 1 ns resolution in time. This PL signal is also transferred to another channel of the digital

oscilloscope TDS-5104, where the PL transient is displayed and processed together with MW-PC transient. Profiling of the carrier lifetime distribution is implemented by a 2D stage driven by step-motors with positioning precision of about 2 μm.

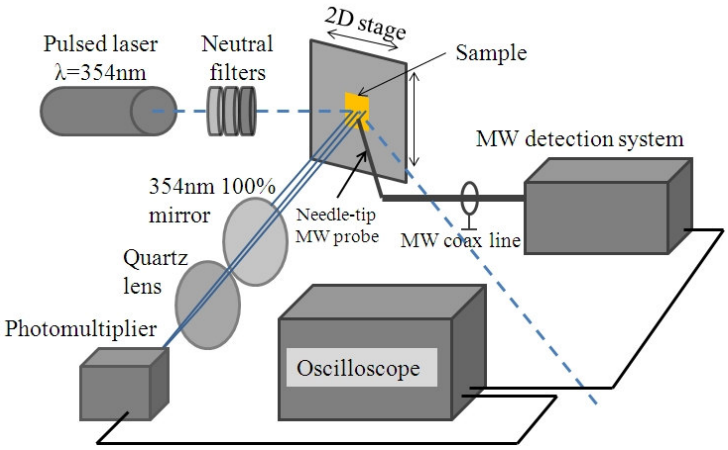

Fig. 3.7. Setup of the experimental arrangement for simultaneous recording of the pulsed photoconductivity and spectrally dispersed photoluminescence transient signals.

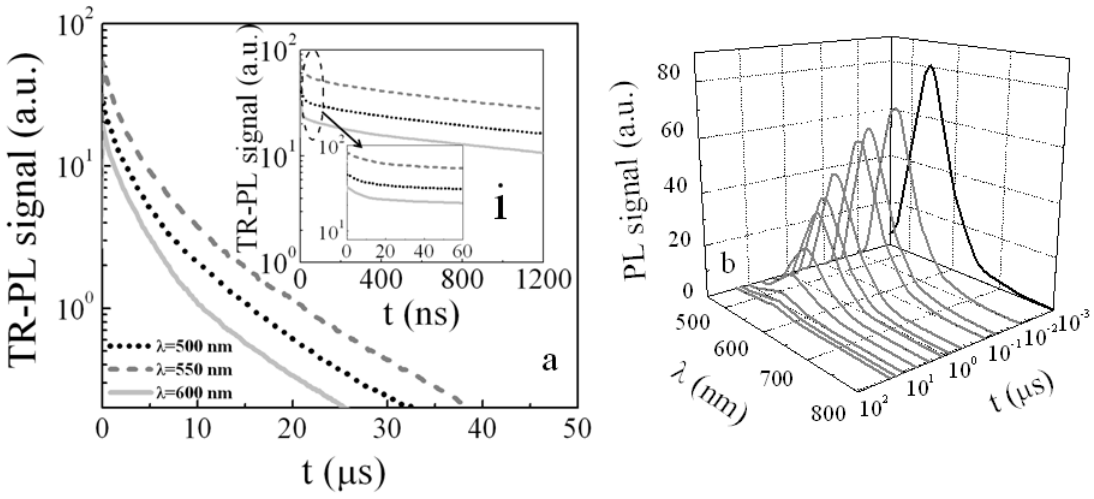

Fig. 3.8. a- Transients of the green-yellow PL recorded in the sample No. 4 at different PL wavelengths. In the inset (i), the initial components of the PL transients in semi-log scale are presented. b- Evolution of PL spectrum [A8].

The typical variations of the time resolved green-yellow PL (TR-PL) transients recorded simultaneously with MW-PC signal for a fixed UV laser excitation spot are illustrated in Fig. 3.8. These variations of PL spectra were recorded at room temperature for a fixed excitation wavelength 354 nm.

The clearly multi-componential TR-PL transients with clearly expressed two terms are observed (Fig. 3.8a). The initial components are significantly shorter than the asymptotic one (Fig. 3.8a). The effective PL decay lifetime within the very initial PL decay stage (in the inset of Fig. 3.8a of durations ≤10 ns) is close to values of the MW-PC transient. This component generally represents the initial changes of the total density of excess carriers. Fast non-radiative recombination is able to reduce the carrier capture to radiation centres, while only rather small portion of the initially photo-generated carriers decay through luminescence. Thereby, a short segment of the very initial PL decay stage seems to represent the initial filling of deep radiative recombination centres (responsible for photoluminescence) which compete with the non-radiative recombination centres. Nevertheless, duration of the complete PL transient considerably exceeds that of the MW-PC transient. This result hints that processes of the radiative and non-radiative recombination are governed by different types of defects.

Evolution of the PL spectra is illustrated in Fig. 3.8b. These PL spectra are obtained for transparency spectral range of a diamond crystal, - therefore the sample thickness averaged PL signal has been recorded. To cover the entire range of the resolvable PL signals, the logarithmic time scale is here used. The spectral peak of the PL band is at 550±10 nm. The slightly asymmetric spectral band has been recorded. It is broadened towards the long wavelength wing, while this spectral band is rather wide covering a spectral range from 450 to 800 nm. This result is in agreement with spectra reported in Ref. [141]. This photoluminescence band had been ascribed to the octahedral growth morphology sectors, and it was interpreted in [44, 45, 141, 142] through the radiative transitions within complexes of the positively charged nickel atom aggregated with nitrogen impurities and di-vacancy.

The PL relaxation rate is slightly different for various spectral ranges: the green PL process appears to be longer within the asymptotic stage of the PL decay, relative to those transients recorded for the yellow PL (Fig. 3.8a). Moreover, the rather long green-yellow PL durations within two-componential

transients and considerably longer asymptotic components support the visibility of the fluorescence images (Fig. 3.1).

The non-exponential TR-PL decay can appear [52] for the donor-acceptor photoluminescence (DAP) if radiative recombination rate *W(R)* depends on the spatial separation *R* between the donors and acceptors involved. This leads to an increase of the instantaneous DAP decay lifetime with display time *t*. The DAP intensity transient $I_{DAP}(t)$ can be described by expression [52]:

$$I_{DAP}(t) \propto N e^{4\pi \int_0^\infty (e^{-W(R)t}-1)R^2 dR} \left(\int_0^\infty W(R) e^{-W(R)t} R^2 dR \right) \quad (3.1)$$

According to this model [52], the PL band originating from the DAP-type radiative transitions is expected to shift to the longer wavelength spectral wing. In our experiments, no clearly observable shift (Fig. 3.8b) of the PL band peak is obtained. Alternatively, the inhomogeneous distribution of excess carriers, captured to the DAP-type centres, can be expected due to the carrier diffusion mediated surface recombination. The luminescence signal, collected from the excited sample bulk, is then the wafer thickness averaged function of time. The time variations of luminescence intensity $I_{PL}(t)$ could reproduce the surface recombination determined transient, - for values of the radiative recombination lifetime $\tau_{RR} \sim 1/B_{RR} n_{exA,D}$ (with a coefficient of radiative recombination B_{RR} and carrier concentration $n_{exA,D}$ captured to *A* and *D*) which would be longer than carrier capture lifetime τ_C and shorter than effective lifetime of surface recombination $\tau_{eff} = (\tau_b^{-1} + D\eta_I^2)^{-1}$, i.e. $\tau_C < \tau_{RR} < \tau_{eff}$. The two-exponential character of PL transients (Fig. 3.8a) with asymmetric initial and asymptotic decay components imply the photoluminescence decay transients governed by surface recombination.

3.1.3.4. Electron spin resonance spectroscopy

The electron spin resonance (ESR) technique provides information concerning microscopic structure of defects. In this research, the ESR technique has been applied for identification of the electrically active

impurities and their complexes involved. The ESR measurements have been performed by using a Bruker Elexsys E580 X-band spectrometer operating (Fig. 3.9) in 8–10 GHz microwave frequency range. A Bruker cryostat is also employed for measurement of the temperature dependent ESR spectral changes in the range of 90–300 K using this cryostat. A programmable goniometer E218-1001 is exploited for the rotation of the oriented sample with respect to the external magnetic field in order to observe the angular variations of the ESR spectra. The resonance microwave frequency and relevant MW power (varied in the range of 0.2–2.4 mW) are initially defined. Thereby, several MW power levels are tried to find the optimal MW power for the sample under investigation and to avoid signal distortions. The modulation amplitude is changed in the range of 0.1–2 G. Ranges of saturation of the ESR signal are determined by examination of the ESR signal changes dependent on the applied MW power.

The ESR typical spectra enabled us to identify the dominant defects in different samples (Fig. 3.10). These spectra are normalized to a sample volume since it is required for Bruker software for evaluating the concentration of spins. Sample weight as well as volume and absolute values of ESR signals have been correlated to extract concentration of spin-active impurities of nitrogen and metal.

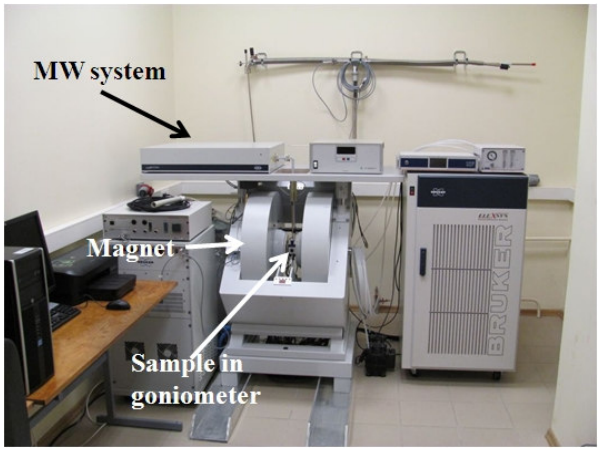

Fig. 3.9. Bruker Elexsys E580 ESR spectrometer

The ESR spectrum of the diamond sample measured at room temperature exhibits the characteristic ESR resonances from the *P1* paramagnetic centre [143], associated with a neutral single substitutional nitrogen impurity (S=1/2) in the diamond lattice. The *g*-factor of the central line of the *P1* paramagnetic centre is equal to 2.00217±0.00003, and the line width, evaluated by the peak-to-peak value, is 0.26 mT. For the externally applied magnetic field aligned parallel to a <110> crystallographic direction, the low-field and high-field satellites are symmetrically observed at +/-2.9 and +/-3.7 mT around the central ESR resonance of the P1 centre. Also, two additional ESR resonances (at ±1.8 mT with reference to the central resonance) appear in the ESR spectrum. These additional resonances are caused by the exchange interaction between the nitrogen atoms if their concentration is rather large, $>2 \times 10^{18} cm^{-3}$ [144]. The observed *P1* centres are in good agreement with the literature data [144-147]. The ESR spectrum of these *P1* centres is formed by the hyperfine interaction between the unpaired electron and the N14 nitrogen nucleus with a spin of *I*=1 [145]. Angular variations of the ESR spectra in diamond, measured at room temperature, are illustrated in Fig. 3.11. The hyperfine structure tensors and an anisotropy (*A*) values for the *g*-factor were evaluated being of the $A_{\|}$ = 113.98±0.05 MHz, $A_{\perp}$ = 81.34±0.05 MHz and $g_{\perp} - g_{\|}$ = 0.0002 by using the EasySpin [148] simulation platform.

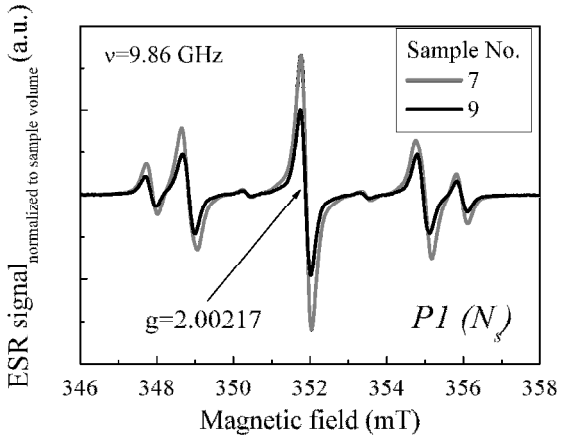

Fig. 3.10. ESR spectra recorded at room temperature in different diamond samples ascribed to the nitrogen impurities. These spectra are normalized to a volume/weight of each sample. The magnetic induction vector *B* was parallel to the <110>crystallographic direction [A8].

These values correlate well with the data published in Ref. [149]. Due to the very small value of the *g*-factor anisotropy, the shift of the central ESR resonance is not observable.

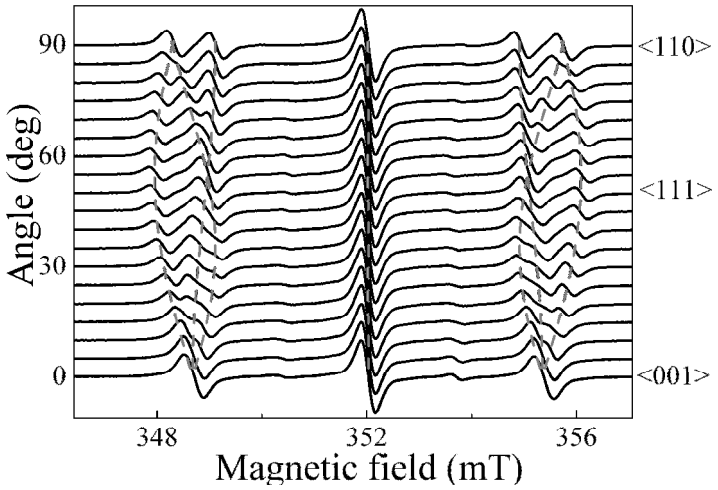

Fig. 3.11. Angular variations of the ESR spectra in diamond crystal measured at room temperature. Gray dashed lines are modelled by using EasySpin simulation platform [A8].

The temperature scans (Fig. 3.11) of the ESR spectra enabled us to resolve the ESR signals ascribed to the substitutional negatively charged nickel (Ni_s^-) S=3/2, referenced as *W8* centre [146]. This centre was first observed in a synthetic diamond grown in the nickel-containing system [150]. The Ni involvement in *W8* (g=2.0319) was confirmed, and a 0.65±0.005mT hyperfine splitting from Ni61 was observed in powdered specimens with 86% content of this isotope in comparison with its 1.2% natural abundance [146]. The saturation of the ESR signal ascribed to the *P1* centre increases at low temperatures (100 K) within temperature scans of the ESR spectra. However, the additional single peak P_{Ni} of the rather high intensity appears within the ESR temperature scanned spectra at the same power (2.4 mW) of MW probe (Fig. 3.12). The latter resonance P_{Ni} stays in the stable spectral position (346.88 mT) during measurement of the angular characteristic. While the saturated ESR peak, ascribed to the *P1* centre (caused by the hyperfine interaction between an unpaired electron and a N14 nitrogen nucleus) shifts its spectral

position within angular dependence. The *g*-factor of the isotropic ESR resonance P_{Ni} is equal to g=2.0319±0.0001, and a width of the peak-to-peak resonance curve is 0.28 mT.

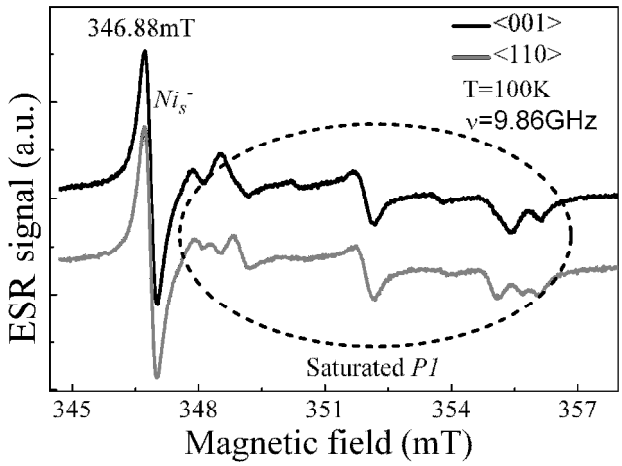

Fig. 3.12. ESR spectra measured at 100 K in diamond crystal, when the sample is oriented perpendicularly to magnetic field <001> and in parallel to magnetic field <110>. The Ni ascribed resonance is indicated (g = 2.0319) as Ni_S^- in the figure, which can be attributed to the *W8* centre known in the ESR nomenclature [A8].

The concentrations of *P1* and P_{Ni} defects have been evaluated by employing the standard Bruker spectrometer software using values of each wafer volume (using the weight and material density values). The ESR spectra were measured at different MW power values to avoid the saturation effect during concentration evaluations. The concentration of *P1* defects has been evaluated to be in the range of (1.2-2)×10^{19} cm^{-3} in all the samples. While, the concentration of P_{Ni} defects was evaluated to be 1.9×10^{17} cm^{-3}, 1.4×10^{17} cm^{-3} and 5.4×10^{16} cm^{-3} in samples, No. 4, No. 7, and No. 9, respectively (Table 3.3).

Table 3.3. Concentration of defects in various diamond samples evaluated by ESR spectroscopy.

Sample No.	Defects concentration (cm^{-3})	
	P1 (N)	P_{Ni}
4	(2.4±0.3)×10^{19}	(1.9±0.5)×10^{17}
7	(2.2±0.3)×10^{19}	(1.4±0.3)×10^{17}
9	(1.2±0.2)×10^{19}	(5.4±0.4)×10^{16}

Table 3.4. Concentration of the identified impurities in HPHT diamond wafer samples, evaluated by combining ESR and FTIR spectral analyses.

Defect Type	Technique	Sample Nr.4			Sample Nr.7	Sample Nr.9
		Defect concentration x 10^{18} cm^{-3}				
P1 (N)	ESR	24±3			22±3	12±2
P_{Ni}	ESR	0.19±0.05			0.14±0.03	0.054±0.004
Location on the sample		D	F	G	Central area	Central area
C	FTIR	nr	nr	22±2	3.6±1	9.1±2
A	FTIR	nr	23±2	nr	37±3	11±2
C^+	FTIR	nr	3±1	1±1	1.4±1	nr

Concentrations of the inherent defects, extracted using ESR spectroscopy data, fit well (within error bars, Table 3.4) that values determined using FTIR measurements on the same samples.

3.1.4. Characteristics of defects extracted by electrical techniques

The transient signals of the microwave probed photoconductivity (MW-PC) and time-resolved photoluminescence (TR-PL) have been simultaneously measured by employing the experimental set-up sketched in Fig. 3.7. Both the MW-PC and TR-PL transient signals, generated by the same UV (354 nm) beam spot of a pulsed (400 ps) laser STA-3H, are displayed by a real-time digital oscilloscope. Excitation of the excess carriers is implemented by two-photon/two-step transitions, as it has been deduced from the measurements of the time-resolved transmission dependent on the intensity of the incident light (at 354 nm). The excitation density is varied by spectrally neutral optical filters in the range of 0.025–0.5 mJ/cm^2. The MW-PC response [115,137] has been detected by using a coaxial needle-tip MW probe [151] and a Vilnius University (VU) propriety instrument VUTEG-4 operating in the range of about 21 GHz. The near-field detection regime is employed using the needle-tip MW antenna, while a pulsed photoconductivity signal is collected from an area determined by a spot dimension of the focused laser beam. The microwave signal is determined by material conductivity $\sigma=\sigma_0+\Delta\sigma$, and the

amplitude of the transient response $U_{MW\text{-}PC} \sim \Delta\sigma/\sigma$ is proportional to a photoconductivity $\Delta\sigma$. Microwave probed photoconductivity technique is applicable at rather low excitation levels $\Delta\sigma/\sigma<1$, as for $\Delta\sigma/\sigma\geq1$ saturation of the $U_{MW\text{-}PC}$ appears. At low excitation levels, variations of carrier mobility can be ignored. Therefore, the registered variations in time t of the amplitude $U_{MW\text{-}PC}(t)$ of the microwave probed photoconductivity response is entirely determined by the changes of the excess carrier density $n_{ex}(t)$. The linearity of the MW detector response relative to the carrier concentration is commonly verified by calibration measurements of $U_{MW\text{-}PC}$ as a function of excitation intensity I_{ex} using well-examined samples (e.g. Si with known values of σ_0). The registered MW-PC signal is transferred from VUTEG-4 to a digital 1 GHz oscilloscope Tektronix TDS-5104, equipped with a computer, where MW-PC transient is displayed and processed.

The transients of the microwave probed photoconductivity (MW-PC) recorded in various diamond wafers are illustrated in Fig. 3.13. It can easily be noticed in Fig. 3.13 that the largest MW-PC signals and the longest transients, as a rule, are obtained for wafer samples No.9 and No.7, while these values are reduced for sample No. 4. It has been clarified that the MW-PC transients appear to be single-exponential (inset of Fig. 3.13 in semi-log scale).

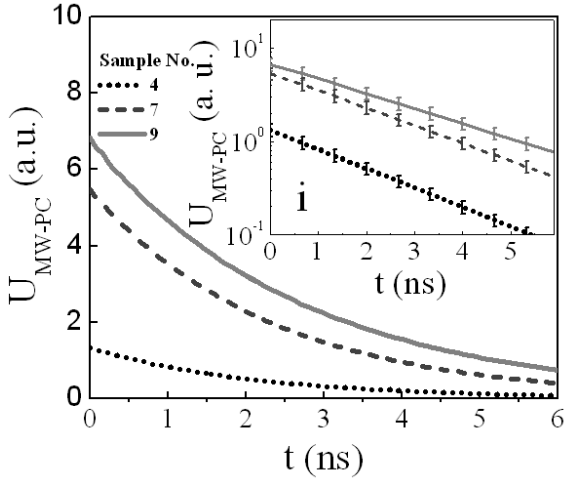

Fig. 3.13. The MW-PC transients recorded in different diamond wafer samples. In the inset, these transients are re-plotted in the semi-log scale [A8].

The recombination lifetime values are directly evaluated from the slope at a level e^{-1} of the MW-PC transient curve plotted within a semi-log scale. The rough relations between the luminescence efficiency (Figs. 3.1, 3.4, 3.8) and the MW-PC signals (Figs. 3.13 and 3.14) can be deduced from the qualitative comparison of the fluorescence images and MW-PC scans. These carrier lifetime profiles scanned by the MW-PC technique are illustrated in Fig. 3.14 for wafers investigated.

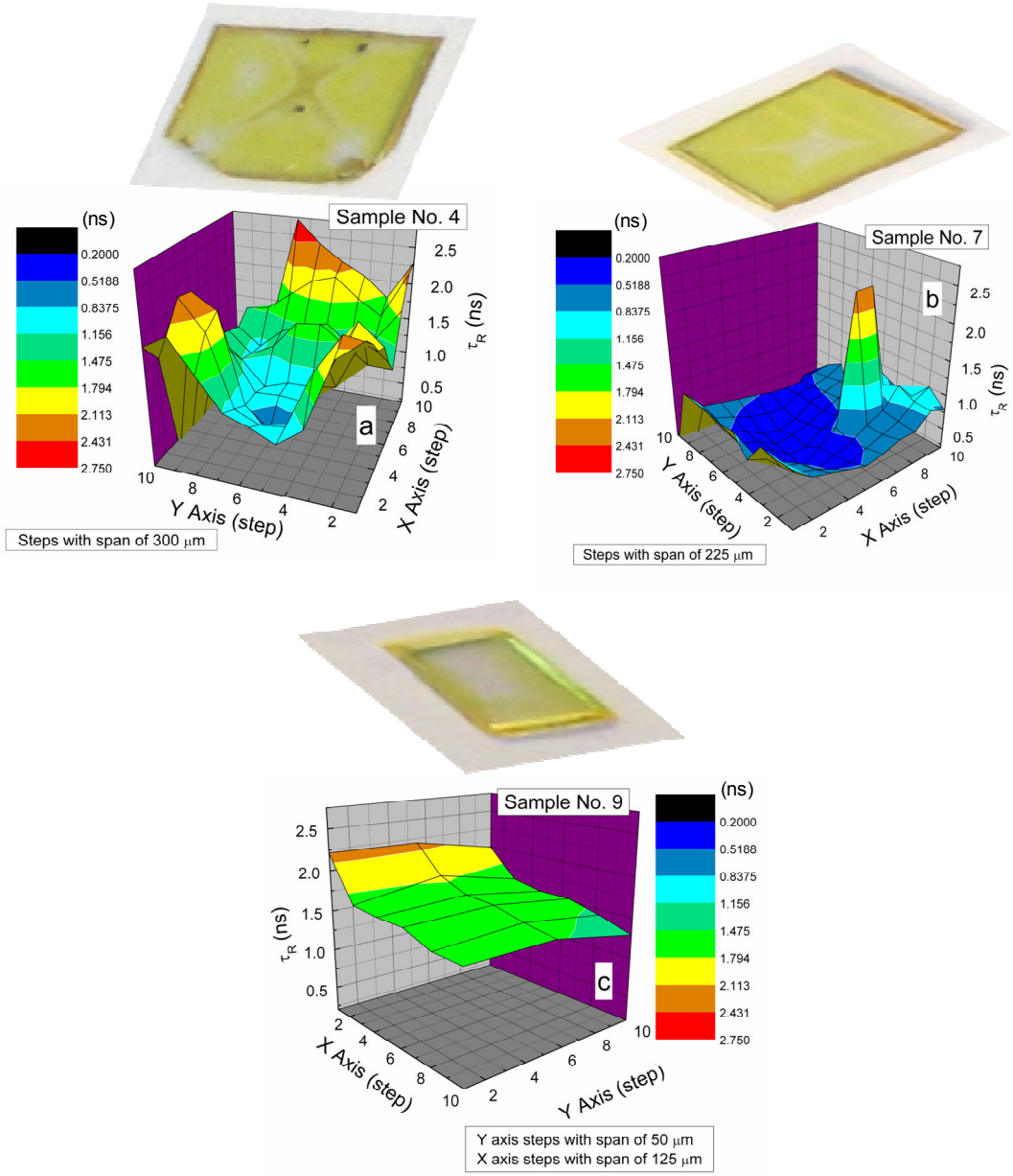

Fig. 3.14. Carrier lifetime lateral distribution profiles in different wafers of the No. 4 (a), No. 7 (b) and No. 9 (c), respectively, mapped by the MW-PC transient scans [A8].

The qualitatively different profiles (Fig. 3.14) of carrier lifetime lateral distribution are obtained in different HPHT diamond samples. A rather flat profile of carrier lifetime values is obtained for wafer No.9 (Fig. 3.14c). It is in agreement with FTIR and fluorescence imaging results obtained for wafer No. 9 where the smallest concentration of nitrogen impurities (Table 3.1) and no fluorescence profile have been obtained. This result is also supported by the largest amplitude of the MW-PC signals (Fig. 3.13). The rather flat lifetime distribution profile (Fig. 14c) hints that the cube morphology sector (nearly all the area of wafer No.9) contains the smallest concentration of nitrogen and metal impurities. The rather homogeneous distribution of recombination lifetime with a single local area of increased lifetime values (Fig. 3.14b) is also obtained for wafer No.7. This local area of enhanced carrier lifetimes could be attributed to a cube morphology sector surrounded by the octahedral sectors. The dark region (of a small area) in samples No.4 and No. 7 has been highlighted within microscopy imaging (Figs. 3.3 and 3.4) which can be ascribed to the cube morphology sector. This sector is in the centre of the cross-like fluorescence image (Fig. 3.1c). The elevated values of the carrier lifetime in the profiling of wafer No.4 (Fig. 3.14a) are revealed for the central area and the corner regions where cube morphology sectors reside. The reduced values of carrier lifetime, relative to those in the central and corner regions of wafer No. 4 (Fig. 3.14a), have been obtained in wafer areas ascribed to the octahedral growth morphology sectors (Fig. 3.1).

The MW-PC transients compared for different sectors (Fig. 3.15) in wafer No.4 imply that the reciprocal relation between the carrier lifetime and the concentration of nitrogen impurities is qualitatively held. A profile of the inverse lifetime scanned in between of the points M and E is illustrated in Fig. 3.16a for wafer No. 4.

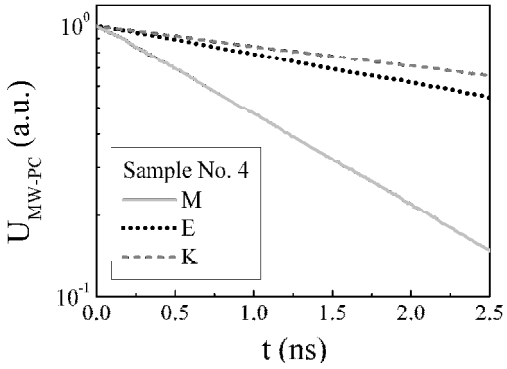

Fig. 3.15. The normalized to a peak MW-PC transients recorded at different location within wafer No. 4 [A8].

There, variation of the concentration of nitrogen impurities extracted from the scanned FTIR spectra (Fig. 3.16b) are used in plots represented in Fig. 16a. A comparison of the lifetime variation profile with a change of the concentration of the nitrogen defects of different types hints the correlation between the inverse carrier lifetime and the concentration of the A-type (N_A) defects, pairs of the nearest-neighbour substitutional nitrogen atoms. It appears that the change of concentration of various type defects ascribed to nitrogen impurities within the mapped line can only be correlated with variation of A-type centres.

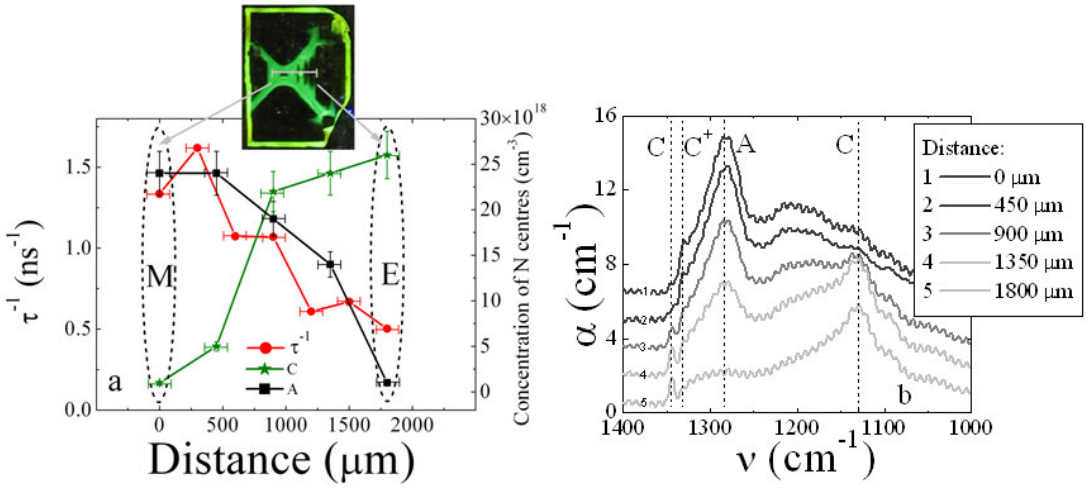

Fig. 3.16. a- Carrier lifetime variation profile scanned along line in between of points M and E denoted in Fig. 6 and concentration of A and C defects in these points for sample No. 4. b – FTIR spectra scanned across the line M and E by step of about 450 μm [A8].

Here, the inverse decay lifetime actually highlights variation of the defect concentration $N_{N\text{-}A}$, as the rough estimation implies $N_{N\text{-}A} \propto 1/(\tau\sigma_{R-N}v_T)$. Here, v_T is the thermal velocity, $\sigma_{R\text{-}N}$ is the capture-cross section for the definite defects, and τ is the measured value of recombination lifetime.

However, the anti-correlation between the inverse lifetime and the concentration of C-type centres is obtained. The changes of the parameters (τ^{-1} and N_A) along the M-E line in wafer No.4 correspond to lifetime scans pointed from the central area to periphery of a crystal. The decrease of the total concentration of nitrogen and of nickel impurities appears within this M-E line due to crystal growth conditions. Reduction of nickel concentration can implicitly be correlated with changes of the C^+ peak (N_{C+}) (Table 3.1) within FTIR spectra. It can be noticed that intensity of the green-yellow PL is also decreased along this M-E direction in wafer No.4. Thereby, the correlation between distribution of the τ^{-1} and N_A obtained in wafer No.4 (Fig. 3.16) and verified for other samples can be explained by competition of the point defects ascribed to nitrogen (A-type) as well as to the nickel impurities those decorate these defects. As mentioned, the trapped nickel impurities had accelerated the aggregation of nitrogen into A-type defects of pairs of the nearest-neighbour substitutional nitrogen atoms, which there are the dominant defects. Luminescence of the enhanced intensity in M vicinity indicates the nickel-rich sectors. The nickel mediated formation of C^+ charged nitrogen defects corroborates also this hypothesis.

Thereby, the lateral distribution of nickel impurities can be associated with a profile of A centres, pairs of nitrogen atoms. The nickel impurities can thus be implied to be the prevailing centres of non-radiative bulk recombination. Therefore, it is necessary to estimate whether the bulk recombination is dominant and resolvable within MW-PC transients relative to the impact of surface recombination. The single-exponential shape and durations of the order of magnitude of 2-3 ns disagree with specific features of carrier decay inherent for surface recombination. In the case of the prevailing

surface recombination, the initial non-exponential component (as a result of superimposed higher decay modes) should be observed and followed by the single-exponential longer decay, determined by the main decay mode and characterized by the effective lifetime $\tau_{eff}=(\tau_b^{-1}+D\eta_1^2)^{-1}$ [71, 115, 137]. Values of this effective carrier decay lifetime are governed by the bulk recombination lifetime only if the τ_b is significantly shorter than the surface component $\tau_{s1}=1/D\eta_1^2$. Value of τ_{eff} can considerably be dependent on both τ_b and τ_{s1} only in a narrow range of close values $\tau_b \approx \tau_{s1}$ of these lifetimes. For rather thin samples with non-passivated surfaces, the surface recombination component determines the effective carrier lifetime τ_{eff}. The shortest component $\tau_{s1}=1/D\eta_1^2$ascribed to surface recombination would be reached at the diffusion limited regime [71, 115, 137]. Value for the surface recombination component at diffusion limited regime $\tau_{s\infty}$ would be $\tau_{s\infty}=d^2/\pi^2 D \geq 1$ μs for our 250-280 μm thick samples assuming the typical carrier mobility μ= 1400 -3000 cm^2/Vs values [152]. Thus, the obtained values of carrier decay lifetimes (Fig. 3.13) of the order of a few nanoseconds, are significantly shorter than that predicted for the diffusion limited surface recombination (of velocity $s\rightarrow\infty$) and do not fit the inherent features of the dominant surface recombination process. Therefore, the prevailing of the bulk recombination through centres of the large cross-section and concentration is inferred. The MW-PC transients actually represent the rates of radiative and non-radiative channels acting together. Thus, the correlation of the MW-PC relaxation curves with the photoluminescence transients, simultaneously measured from the same wafer area, is necessary for the deeper understanding of the prevailing carrier decay processes.

3.2. Characteristics of GaN and CdS materials

3.2.1. Materials and samples

The GaN samples under study were grown by using metal-organic vapour phase epitaxy (MOCVD) on sapphire substrates and hydride vapour phase

epitaxy (HVPE) methods. The MOCVD GaN epi-layers of 2.5–25 μm thickness were grown on sapphire substrates using MOCVD reactor at Vilnius University. The commercial HVPE GaN wafer fragments of 475 μm thickness contained Fe impurities of concentration of 2×10^{17} cm^{-3}, as verified by ESR spectroscopy. Pictures of the wafer fragment samples are illustrated in Fig. 3.17.

a b c

Fig. 3.17. Wafer fragment samples: of commercial HVPE GaN:Fe (a); HVPE-HD GaN (b) and HVPE-LD GaN (c). Wafer thickness: 475 μm (a) and 400 μm (b, c).

Colour of wafer samples is determined by the type and concentration of the intentionally introduced impurities. These metallic impurities were introduced by vendors, in order to modify resistivity of the materials.

3.2. 2. Spectral characteristics of GaN

3.2.2.1. Pulsed photo-ionization spectra

The pulsed photo-ionization spectroscopy (PPIS) has been implemented using excitation by a tuneable wavelength laser and measurements of the photo-response using microwave probed photoconductivity transient (MW-PC) technique sketched in Fig. 3.5. Here tuneable wavelength (in the range of 0.26 μm to 16 μm) femtosecond (40 fs) light pulses with energies of 20 μJ – 1mJ per pulse are generated by a laser system (Ti:Sapphire - HE-TOPAS) with an optical parametric amplifiers (OPO) and differential frequency generators (DFG). The sample was placed on the slit-antenna of 21 GHz microwave (MW) system. The pulse microwave response detected in the MW system represents a change in the signal of photo-conductivity which is proportional to

excess carrier concentration generated by laser pulses. The transients of MW-PC signal have been recorded by using 1 GHz oscilloscope Tektronix TDS-5104 (Fig. 3.5.).

The PPIS spectra recorded at room temperature on HVPE GaN and MOCVD GaN wafer samples are illustrated in Fig. 3.18. The photo-ionization spectrum is obtained as the MW-PC signal amplitude, proportional to excess carrier density generated by photo-ionization, dependence on photon energy. This PPIS spectrum has a step-like structure.

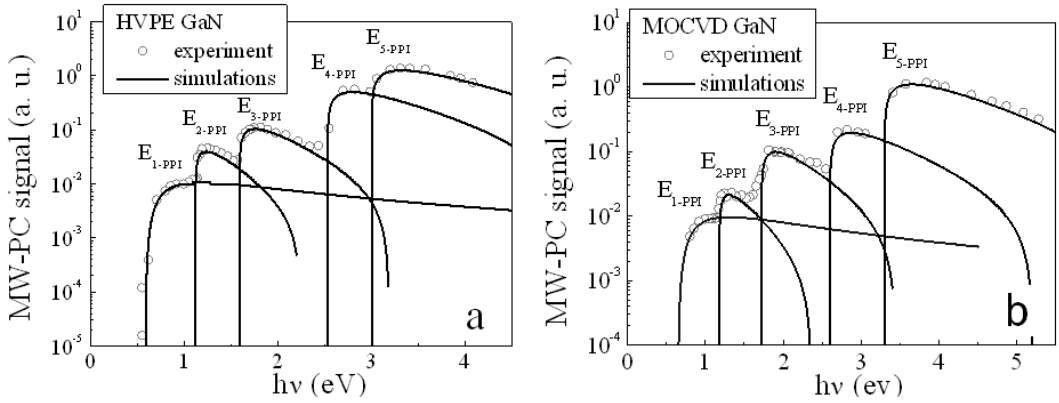

Fig. 3.18. The photo-ionization spectra of HVPE (a) and MOCVD (b) GaN [A2].

Photo-ionization or photo-neutralization of deep levels is characterized by optical cross-section, and spectroscopy of these cross-sections provides the direct information concerning matrix elements coupling wave functions of deep levels to those wave functions of band free carriers. Assumption of a δ-type potential of deep centre leads to the Lucovsky's model [140,153]. This model is suitable for evaluation of the red threshold of the photo-ionization energy.

Lucovsky's model is a simple approach and has actually only a single parameter E_d of optical activation energy within a fitting procedure of spectra analysis. The photo-ionization of the trapped carriers n_d by using short (fs) pulses of spectrally discriminated light enables ones to determine the

parameters of deep traps and a state of their filling. The cross-section $\sigma_{p\text{-}e}$ in Lucovsky's model [153], is described by expression

$$\sigma_{p-e}(h\nu) = \frac{BE_d^{1/2}(h\nu - E_d)^{3/2}}{(h\nu)^3}, \tag{3.2}$$

where B is a multiplicative factor. Changes of absorption coefficient $\alpha(h\nu)$ for $h\nu$ energy photons due to photo-ionization of n_{d0} trapped carriers can then be described by

$$\alpha(h\nu) = \sigma_{p\text{-}e}(h\nu) n_{d0}. \tag{3.3}$$

Illumination by a light pulse of surface density $F(h\nu)$ of the incident photons leads to the density of photo-emitted carriers $n^*_d = \sigma_{p\text{-}e}(h\nu) n_{d0} F(h\nu)$ registered by MW probe. Then, the density of N_d traps can be evaluated from an absorption coefficient $\alpha(h\nu)$ spectrum. The filling factor n_d/N_d can be controlled by combined measurements of MW-PC signal peak value or $\alpha(h\nu)$ as a function of $F|_{h\nu}$, and the saturation of these characteristics indicates a complete photo-ionization of N_d traps. The PPIS spectrum can be approximated by eq. (3.2) for fixed $F|_{h\nu}$ and n_{d0} quantities.

For more precise fitting of the measured spectral steps, the analysis of differential $d\sigma_{e\text{-}p}/dh\nu$ changes of the photo-ionization cross-section may be preferential. To include a strong electron-phonon interaction, the more comprehensive model of A. Chantre et al (C-V-B model) [154, 155] can be applied, which is more flexible in simulation of the spectral-step shape and the location of spectral maximum, expressed through a product of the electronic transition probability and the vibrational overlap integral. However, it should be pointed out that in C–V–B model [154] three adjustable parameters are exploited, instead of a single E_d parameter for Lucovsky's model.

The step-like photo-ionisation spectra contained up to five spectral peaks, denoted in Fig. 3.18 as $E_{i\text{-}PPI}$, have been obtained for both HVPE and MOCVD GaN samples. The threshold photo-ionization energy values, extracted by fitting of experimental peaks, have been analyzed by comparing with literature

data. Thereby these photo-ionization peaks have been associated with different deep centres.

Table 3.5. The threshold activation energy values, estimated by using Lucovsky model, and assignment of defects, using typical activation energy values referenced in literature.

Material	HVPE GaN		MOCVD GaN	
Spectral step	Photo-activation energy (eV)	Defect type	Photo-activation energy (eV)	Defect type
$E_{1\text{-}PPI}$	0.6±0.1	V_{Ga}^{-} [52]	0.7±0.1	V_{Ga}^{-} [52]
$E_{2\text{-}PPI}$	1.1±0.1	N_{Ga} [53]	1.2±0.1	N_{Ga} [53]
$E_{3\text{-}PPI}$	1.6±0.1	Fe^{3+} [54]	1.7±0.2	$V_{Ga}O_N$ [64]
$E_{4\text{-}PPI}$	2.5±0.2	C_N [64]	2.6±0.2	C_N [64]
$E_{5\text{-}PPI}$	3.0±0.2	Fe^{2+} [156]	3.3±0.2	C_NO_N [64]

The dominant PPIS peaks obtained for HVPE and MOCVD GaN wafer samples are listed in Table 3.5, where attribution to the photo-active centres caused by the technological defects is denoted and referenced to the relevant papers. The crystalline structure defects as vacancy as well as anti-site and carbon impurities have been discriminated in both HVPE and MOCVD GaN materials. It has also been obtained that Fe impurities induce the dominant deep centres in HVPE samples while C impurities are photo-active centres in MOCVD GaN samples.

3.2.2.2. Parameters of GaN evaluated by deep level transient spectroscopy

The DLTS measurements have been implemented by using a HERA-DLTS System 1030 spectrometer [157]. The temperature scans are performed in the range of 20–300 K using a closed-cycle He cryostat. The temperature sensors are connected to a *LakeShore* temperature control device. The barrier capacitance changes (due to carrier traps) are directly recorded as the capacitance transients by using a *Boonton* capacitance meter installed within the HERA-DLTS System 1030 spectrometer. DLTS measurement procedures

are controlled by a personal computer with installed Phys-Tech software. The PhysTech software is calculating the properties of deep levels such as the carrier capture cross-section, trap thermal activation energy and concentration of the levels. In order to suppress carrier fast decay through large density of carrier traps, inherent for compensated or unintentionally doped sample, it has been continuously illuminated by LED light of 380 nm wavelength for optical-DLTS [76, 158] measurements (O-DLTS). The bias LED illumination of the compensated or unintentionally doped GaN serves for steady-state generation of free carriers. These carriers enable the partial depletion regime in the steady illuminated structure. For material without steady-state illumination, it is completely depleted at conditions close equilibrium. To predict changes of detector parameters, it is necessary to control the spectra of the introduced radiation defects. The standard and widely used spectroscopy technique is the C-DLTS which is a sufficiently sensitive and straight spectroscopy technique for characterization of deep radiation traps. However, the standard application of C-DLTS is limited by the trap concentration, which should not be larger than the doping density. The measurement of generation current (I-DLTS) is an option of the DLTS technique, which can be approved for the spectroscopy of high density carrier traps in silicon detectors made of large resistivity material. An electrical filling of deep traps by manipulating the carrier injection pulses exploited in standard DLTS techniques can be inefficient for the radiation affected junction of the detectors. Therefore, an additional modification of DLT spectroscopy is implemented by using an optical carrier injection leading to the optical current DLTS (O-I-DLTS) regime. Optical excitation employing the laser or LED light illumination fills both types of the majority and minority carrier traps. However, it is impossible to distinguish the current components ascribed to the majority and minority carrier traps within the generation current transients. This is a disadvantage for usage of O-I-DLTS. The O-I-DLTS regime has been implemented by using optical 20 ms injection pulses generated by an yttrium aluminium garnet neodymium (Nd:YAG) laser at 1064 nm wavelength.

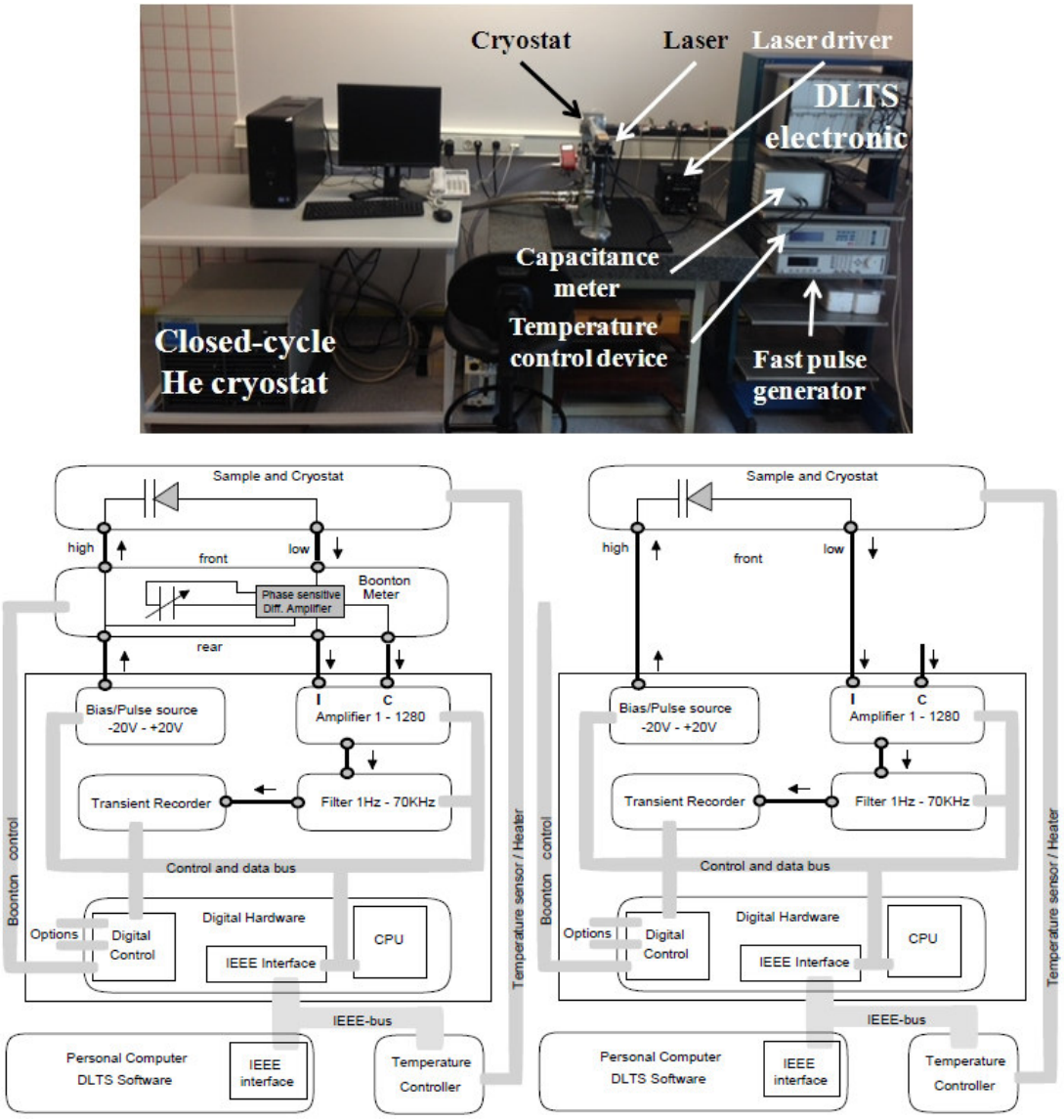

Fig. 3.19. A view (on top) of spectrometer and schemes (on bottom of figure) of module connections within HERA-DLTS System 1030 instrument [157].

The DLTS technique allows evaluating of the activation energy, concentration and analysis of capacitance transients caused by trapping and emission processes [76]. Interaction between free carriers and centres is described by the rate equations, employing the parameters of $c_n=\sigma_n\langle v_n\rangle n$ electron capture rate, of $e_n=\sigma_n\langle v_n\rangle N_C\exp[-(E_C-E_T)/k_BT]$ electron emission rate, of $c_p=\sigma_p\langle v_p\rangle p$ hole capture rate and of hole emission $e_p=\sigma_p\langle v_p\rangle N_V exp[-(E_T-E_V)/k_BT]$ rate. Here σ denotes capture cross-section, $\langle v\rangle$ stands for thermal velocity, n and p denote free carrier density for electrons and holes,

respectively, N_C, N_V represent density of states within conduction and valence bands, respectively, E_T is the activation energy for definite trap. It is well-known that carrier capture rates depend on free carrier density while carrier emission rates depend on trap activation energy and temperature. With special regimes it possible to observe majority and minority carrier traps and to have injection either by electrical or optical pulse.

A routine capacitance based DLTS the filtered signal is proportional to the ratio of trap concentration (N_T) to that of the effective doping (N_{Def}). The time varied barrier capacitance change $\Delta C(t)$, determined by the majority carrier emission from deep levels, is described by relation:

$$\frac{\Delta C(t)}{C} = \frac{1}{2}\frac{N_T}{N_{Def}} e^{-e_n t}, \tag{3.4}$$

with the parameter C of barrier capacitance.

The I-DLTS signal does not depend directly on N_{Def} value, and there is no limitation for the ratio of N_T/N_{Def}. The total current density is then expressed by relation $J(t)=J_L+\delta J$, where the first component represents the leakage current density J_L while the second term is the transient signal of the current density δJ (t)) The last quantity is expressed as

$$\delta J(t) = -\frac{1}{2} q x_d N_T \frac{e_n}{e_n + e_p}\left(e_n - e_p\right) e^{-(e_n+e_p)t}. \tag{3.5}$$

The amplitude of the transient signal δJ depends on the depletion width x_d, on the concentration N_T of deep traps and on the emission rate e_n.

In order to achieve the efficient filling of deep traps and governing of a barrier in rather compensated material, the optical excitation is commonly employed for the high resistivity samples. In the case of optical excitation, both majority and minority carriers determine the amplitude of the transient signal. Then, photo-injected carriers determine variations of depletion width dependent on carrier drift velocity and on carrier concentration, due to carrier emission within partially depleted junctions. Thus, O-DLTS transients are mainly governed by carrier density changes due to thermal emission. In order

to suppress carrier fast decay through large density of carrier traps, inherent for compensated or unintentionally doped GaN, the sample has been continuously illuminated by LED light of 380 nm wavelength for optical-DLTS [71] measurements (O-DLTS).

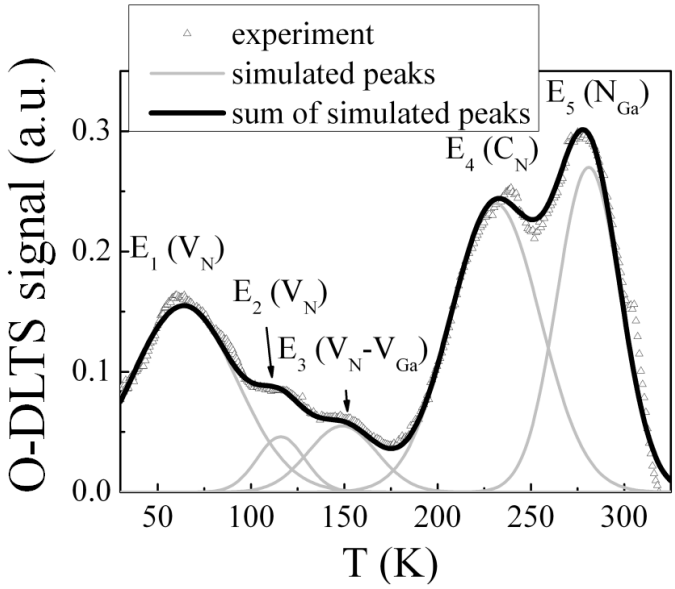

Fig. 3.20. O-DLTS spectra recorded on MOCVD GaN Schottky diode [A2].

Spectra of thermal activation of the deep levels, recorded using O-DLTS measurements, are illustrated in Fig. 3.20. The O-DLTS spectra were recorded at a reverse bias of U_R=-2 V in the temperature range of 30–315 K using time windows of t_w=2s. The electrical injection pulse of U_p=-0.1 V of duration t_p=1s was used in these experiments. At least five overlapping O-DLTS spectral peaks have been observed in MOCVD GaN Schottky diodes. The amplitudes and their positions within temperature scale of different O-DLTS peaks have been separated by simulating the sum amplitude of the overlapping spectral peaks. The spectra have also been manipulated by varying time window of t_w. The Arrhenius plots then were made to evaluate activation energies associated with different O-DLTS peaks. Using extracted values of the separated O-DLTS peaks, the thermally active traps have been identified by comparing with literature data. These traps with the denoted activation energies have been ascribed to technological defects as follows: $E_{1\text{-}ODLTS}$= 0.15 eV as vacancy V_N defect [59], $E_{2\text{-}ODLTS}$= 0.20 eV as V_N defect [63], $E_{3\text{-}ODLTS}$= 0.27 eV as V_N-V_{Ga}

complex [63], $E_{4\text{-}ODLTS}$= 0.44 eV as C_{Ga} impurity [62], $E_{5\text{-}ODLTS}$= 0.54 eV as N_{Ga} anti-site defect [55]. The carbon impurity ascribed centres seem to be involved in photo-ionization and thermal emission processes.

3.2.2.3. ESR spectra for GaN

In order to verify existence of Fe impurities in HVPE GaN material, the ESR measurements have been performed on these samples. The ESR spectra measured for the magnetic field oriented in parallel to the crystal c-plane (Fig. 3.21a) provide clear identification of Fe impurities [7]. The angular dependence of the ESR response (Fig. 3.21b) measured for both the parallel and perpendicular magnetic field orientations relative to c-plane provided the structural information concerning Fe impurities. These ESR spectra variations supported the PPIS data obtained on the same samples. It has also been deduced from ESR measurements that concentration of 2×10^{17} cm^{-3} Fe impurities resides in HVPE GaN.

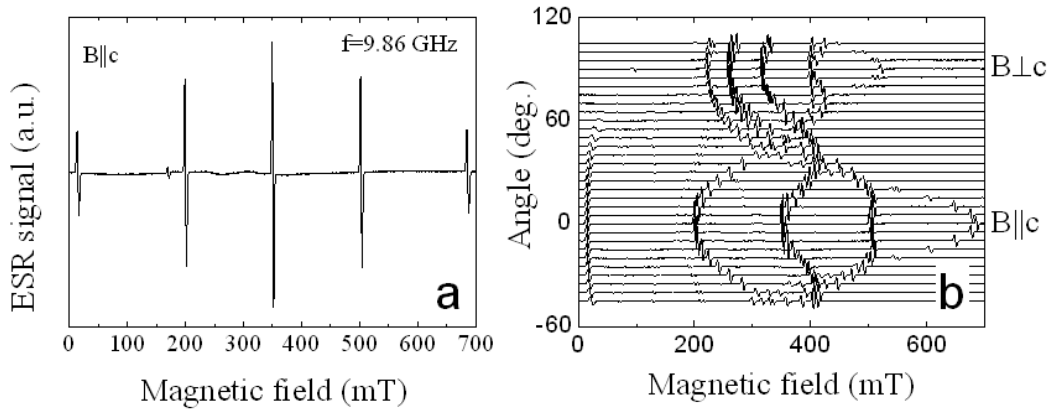

Fig. 3.21. An ESR spectrum (a) and its angular dependence (b) on the orientation of the magnetic field relative to the c-plane [A2].

3.2.2.4. Photo-luminescence spectra for GaN

The time resolved (TR) and continuous wave (cw) photo-luminescence (PL) spectra (Fig. 3.21) in the initial GaN materials were examined in order to have baseline data for comparison with irradiated samples.

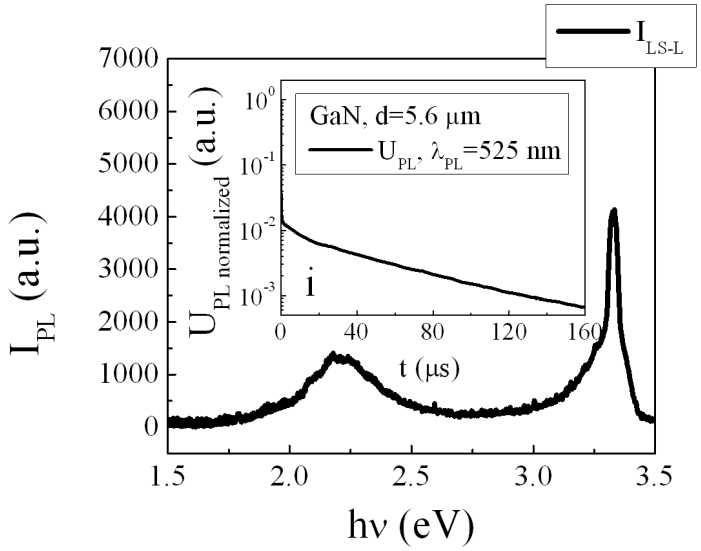

Fig. 3.22. The cw-PL spectra excited by a laser pulse at 354 nm wavelength. Inset i - The TR-PL transients are illustrated.

In Fig. 3.22, the cw PL spectra excited by a laser pulse at 354 nm wavelength are illustrated. Several TR and cw-PL bands (Fig. 3.22) can be resolved. Namely, the ultra-violet (UV) and blue (B) bands in the range of wavelengths 350-430 nm, the yellow-green (YG) peaked at 560 nm and the red- infrared (RIR-L) with peak in the range of 710 nm are resolved. The UV-B and YG bands are well-known [52], and these luminescence bands are commonly ascribed to radiative recombination through excitonic and donor-acceptor transitions, where the latter centres are attributed to the growth defects in MOCVD GaN layers. The YG and the RIR bands are commonly associated with randomly distributed point defects [52]. Alternatively to interpretations [52] of the B-PL band origin, the B-PL can also be attributed to the rather high density of dislocations, which is estimated by XRD technique to be of the order 10^{10} cm^{-2} in this MOCVD GaN epi-layers.

3.2.3. Microwave probed photoconductivity transients in GaN

The MW-PC transients recorded in most of the GaN samples appear to be two-componential (Fig. 3.23).

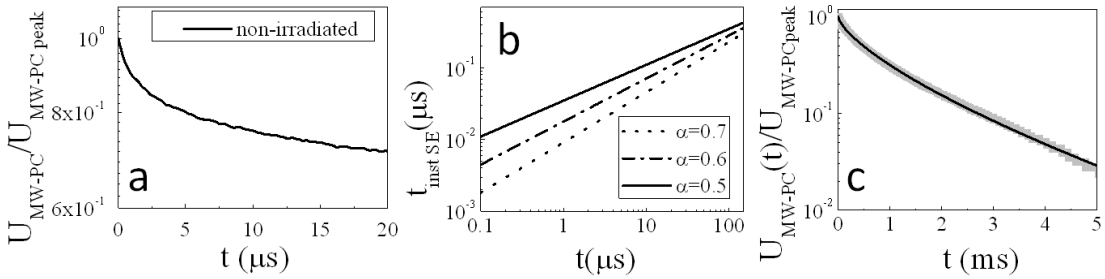

Fig. 3.23. a - MW-PC transients in non-irradiated GaN. b - figure represents the simulated instantaneous lifetimes ascribed to different time instants within interval $0 \leq t \leq t_{inst}$ varying SER index. c - illustrates the persistence of two-component relaxation curve of carrier density over the longer display scale.

The MW-PC asymptotic decay component of durations in a millisecond time scale obeys ($U_{MW\text{-}PC}(t)=U_{MW\text{-}PC}(t=0)\exp[-(t/\tau_{SE})^{\alpha}]$) the stretched-exponential (SER) relaxation law interpreted through a disorder of material. Here, $U_{MW\text{-}PC}(t)$ is the change in time (t) of the amplitude of the MW-PC signal; τ_{SE} is the characteristic time ascribed to the SER process approximated using SER with index α [159,160]. The disorder in the as-grown GaN epi-layers can be related to the dislocation networks at the prism type crystallites which are twisted to each other by a certain angles [161]. Values of α are extracted using a routine plot (Fig. 3.22c) in SER analysis [159,160].

As it was shown in Ref.[80], the photoconductivity (PC) asymptotic decay component with a duration in the millisecond time scale obeys to:

$$U_{PC}(t)=U_{PC}(t=0)\exp[-(t/\tau_{SE})^{\alpha}] \quad (3.6)$$

the stretched-exponential relaxation (SER) law (eq.(3.6)) interpreted through a disorder of material in both contact (C-PC) and contactless (MW-PC) signal recording modes. Here, $U_{PC}(t)$ is the change in time (t) of the amplitude of the C-PC/MW-PC signals approximated using SER with index α [159]. τ_{SE} is the characteristic time of SER process expressed as

$$\tau_{SE}=[(4C_D/x^2)\tau_1]^{w/(w-2)}=[(4C_D/x^2)\tau_1]^{1/\alpha} \quad . \quad (3.7)$$

The characteristic time of SER process is related to the parameters of anomalous diffusion with a coefficient

$$C_D=Dt^{1-(2/w)}, \quad (3.8)$$

and the diffusion exponent *w,* in approach of the anomalous diffusion of carriers (with the diffusion coefficient *D)*. Here, *x* denotes the displacement in random-walk with a single-step-walk duration τ_1. To cover wide range of PC transients of different durations, the changes of the instantaneous lifetime

$$\tau_{inst} = n(t) \Big/ (-\frac{dn(t)}{dt}) \ , \tag{3.9}$$

expressed in the case of SER as

$$\tau_{inst,\,SE} = \tau_{SE}^{\alpha} t^{1-\alpha} / \alpha \ , \tag{3.10}$$

have been examined. This instantaneous lifetime expression reproduces the power law $\sim t^{1-\alpha}$ dependences with the time *t* exploited in analysis of dispersive transport transients. The disorder in the as-grown GaN epi-layers can be related to the dislocation networks at the prism type crystallites which are twisted to each other by certain angles [161]. Simulation of instantaneous lifetime using experimental transients for the time interval $0 \leq t \leq t_{inst}$ (as illustrated in Fig.3.23b) enables to evaluate the SER index α. Prevailing of SER type relaxation curves can be implied from a seeming two-componential decay (Fig. 3.23c) over different display scales of transients.

3.3. Evolution of the material characteristics during irradiations

3.3.1. Arrangements for the in situ measurements

The in situ measurements are devoted to track evolution of material characteristic variations under introduction of radiation defects. Particularity of this type measurement is a requirement for remote sensing of signals by obviating the radiation damage of instruments and personnel. Also, the contact-less techniques are preferential in order to avoid modifications of electrode materials and contamination of the examined material with products of the radiation damage of metal structures.

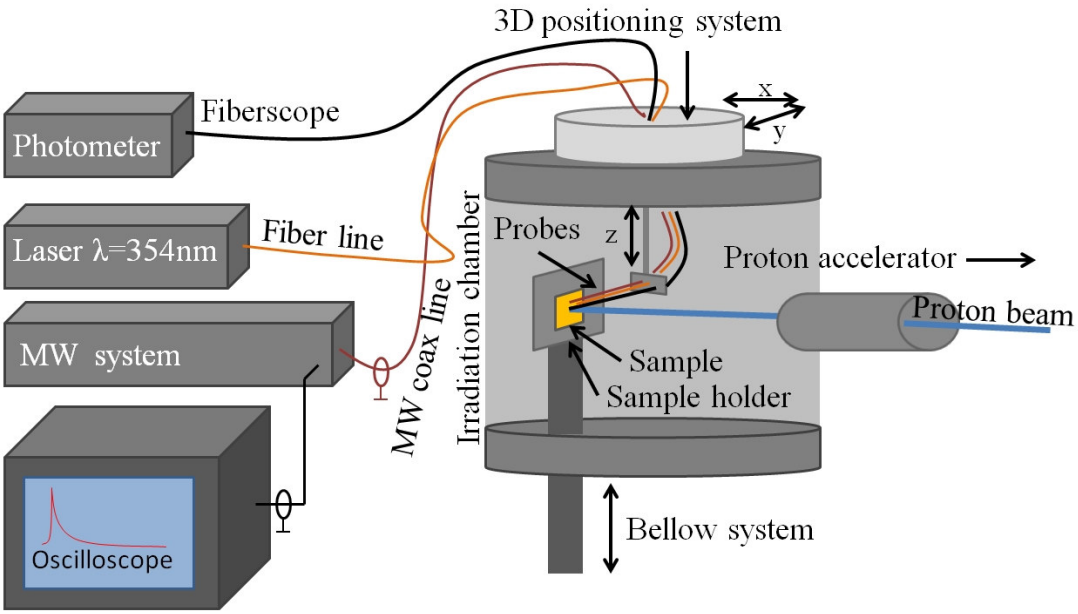

Fig. 3.24. The set-up for the *in situ* and synchronous measurements of the proton beam induced photoluminescence (PL) spectra and microwave-probed photoconductivity transients.

In our experimental arrangement (Fig. 3.24), the photoluminescence spectra and microwave probed photoconductivity (MW-PC) transients were simultaneously recorded. The transient signals of the MW-PC and TR-L have been measured by collecting a response to the same UV (354 nm) excitation beam spot (of an area of 8×10^{-3} cm^2), generated by a micro-chip laser STA-1-TH employed for the pulsed (500 ps) excitation of the excess carriers or the changes of the cw-PL spectra under particle beam exposure. To implement the remote recording of the signals and to transfer excitation/ probe radiations, the optical fiber and waveguide/coaxial transfer lines are designed. The excitation is varied by spectrally neutral optical filters in the range of energy E_L=0.001–0.2 μJ per laser pulse. The MW-PC response has been detected by using a coaxial needle-tip probe and a near field probing regime, performed by a Vilnius University propriety instrument VUTEG-3 equipped with a microchip laser, a system of laser beam attenuation and shaping and a port for connection to fiber lines as well as with microwave generation/detection system and microwave waveguide attachment port. A microwave reflection mode has been implemented in these measurements. The MW-PC registered

signal is transferred from the VUTEG-3 module to a digital 1 GHz oscilloscope Tektronix TDS-5104, equipped with a computer, where MW-PC transient is displayed and processed. The TR-PL/cw-PL light is collected from an area with normal directed towards a bisector between the incident and the reflected UV light beams or an impinging particle beam. The UV filtered TR-PL light is focused onto a slit of a ScienceTech-9030 monochromator. The TR-PL light is displayed using a grating monochromator and detected by a Hamamatsu H10721 photomultiplier. This TR-PL signal is also transferred to another channel of the digital oscilloscope TDS-5104, where the TR-PL transient is displayed and processed together with MW-PC transient. The laser induced luminescence spectra (LI-L), registered by a signal integration regime, have complementarily been registered by employing a spectrophotometer Avantes AvaSpec-2048TEC equipped with a fibber adjusted input. The PL light has been transferred to the photometer input slit using a fiberscope with an aperture of 3×10^{-2} cm^2 area.

3.3.2. Evaluation of the parameters of the radiation impact for GaN

GaN material can be utilized for fabrication of a combined double-purpose device which is able to operate both as scintillating and charge collecting detector. However, the efficiency of such detectors and their functionality has been insufficiently investigated. This work is addressed to study the evolution of the photo-electrical characteristics and of the efficiency of photon and hadron induced luminescence. The production rate of radiation defects has been examined by in situ and post-irradiation changes of the radiative and non-radiative recombination and by combining irradiations using penetrative hadrons, as nuclear reactor neutrons and 24 GeV/c protons, and 1.6 MeV protons, strongly absorbed within a GaN layer. The role of technological and radiation induced defects has been studied by analysis of changes of the material disorder factor evaluated through a stretched-exponent index and the instantaneous carrier decay lifetimes dependence on irradiation fluences in wide range of $10^{11} – 10^{16}$ cm^{-2}.

3.3.2.1. In situ variations of recombination characteristics

The GaN sample is mounted on a cold finger within a specially fabricated irradiation chamber [80] during the 1.6 MeV proton irradiations and the in situ measurements of MW-PC and luminescence signals. This chamber contains the coaxial and fiber connectors to transfer the optical and microwave signals between probes inside vacuum chamber and the measurement instrumentation placed remotely from the irradiation area. The thickness of epi-layers and the 1.6 MeV energy of protons have been chosen on the basis of the initial simulations made by TRIM [162], where a nearly homogenous energy loss of a proton beam is obtained during interaction of protons with GaN material. Contrarily, the optical excitation at 345 nm wavelength determines the initially inhomogeneous excitation due to a large absorption coefficient β=4.7×10^4 cm^{-1} [51]. Thereby, the distribution of the excess carriers acquires the stabilized in-depth profile only after diffusion time $t_D \cong d^2/D$=63 ns (estimated using approximation $d \cong (Dt_D)^{1/2}$) overwhelming the layer thickness d. Here, $D \cong$ 1 cm^2/s is the coefficient of carrier ambipolar diffusion in GaN. The 2.6 -12 μm thick GaN samples were employed for irradiations by penetrative hadrons, - nuclear reactor neutrons and 24 GeV/c protons.

In Fig. 3.25, the S-L spectra excited by a laser pulse (LS-L) at 354 nm wavelength and by a 1.6 MeV proton beam (at a very initial stage, 1 sec, of irradiation) are compared. This comparison has been employed to initially evaluate the excess carrier density excited by protons and to relate it to that of the yellow-green S-L induced by protons. Several TR-L and S-L bands (Fig. 3.25b) can be resolved within both the laser and the proton induced spectra. The ultra-violet (UV-L) and blue (B-L) bands in the range of wavelengths 350-430 nm, the yellow-green (YG-L) S-L peaked at 560 nm and the red- infrared (RIR-L) with peak in the range of 710 nm are resolved. The UV-/B-L and YG-L bands are well-known [52], and these luminescence bands are commonly ascribed to the growth defects in MOCVD GaN layers. The YG-L and the RIR-L bands are commonly associated with randomly

distributed point defects [52]. Irradiation leads to a decrease of the intensity for the most of luminescence spectral bands.

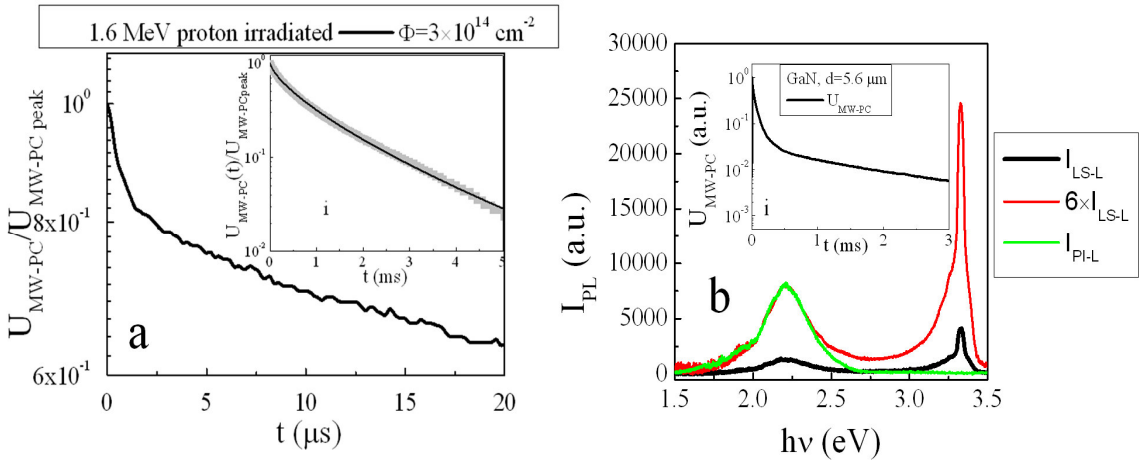

Fig. 3.25. a-MW-PC transients in 1.6 MeV proton irradiated GaN. Inset (i) illustrates the persistence of two-component relaxation curve of carrier density over the longer display scale. **b-** The S-L spectra excited by a laser pulse (LS-L) at 354 nm wavelength and by a 1.6 MeV proton beam (at a very initial stage, 1 sec, of irradiation). The LS-L intensity for the laser induced yellow-green (YG-L) photoluminescence peaked at 560 nm is multiplied by a factor 6 to coincide it with YG-L spectral band registered for proton in situ generated luminescence. A comparison of transients of the photoluminescence (for the YG-L band) and the photoconductivity (MW-PC) recorded in 5.6 μm thick GaN epi-layer is presented in the inset for figure b [A5].

From the fit of laser and proton beam induced luminescence intensities, the average of excess carrier density generated by a proton beam can be evaluated through calibration of the laser pulse parameters and the absorption coefficient β at laser light wavelength. To increase evaluation precision, the inhomogeneity of laser excitation and the time-integration of S-L signal have been included into this fitting procedure. The depth averaged $\langle n_L\rangle = n_0(1/d)\int_0^d \exp(-\beta x)dx = (n_0/\beta d)[1-\exp(-\beta d)] \cong 1.3\times10^{17}$ cm^{-3} carrier density can then be equalized with excess pair density n_P generated homogeneously in d by penetrative protons. The equivalent density n_P of excess carrier pairs generated by protons would be equal to $\langle n_L\rangle$ if time of signal integration coincides with t_D. It has been obtained by equalizing the YG-L intensities (Fig. 3.25a) that integrated density $n_P t_D$ exceeds that $\langle n_L\rangle t_D$ by about 6 times.

This observation is in good agreement with the calculated value of this ratio if a UV pulse induced TR-L transient with initial TR-L decay time $\tau_{YG\text{-}L}^{in}$~10 ns is taken into account for YG-L band, - the spectro-photometer integrated signals over t_D=63 ns are related as $n_P t_D = \langle n_L \rangle \int_0^{tD} \exp[-t/\tau_{Y\text{-}GL}]dt = \langle n_L \rangle t_D(\tau_{Y\text{-}GL}/t_D)$. For longer integration times, the instantaneous TR-PL decay time in asymptotic $\tau_{YG\text{-}L}^{as}$~50 μs is employed to correlate the n_P and $\langle n_L \rangle$ values. A quantity of carrier pair generation by a single 1.6 MeV proton has been estimated by independent evaluating of a flux of protons using values of the proton beam current i_P and the beam area A_P=2×10^{-1} cm^2. The flux of protons is then obtained as $F_P = i_P/eA_P$ ≅8×10^{11} cm^{-2}s^{-1} with e =1.6×10^{-19} C the elementary charge of proton. Then, it is estimated a quantity of protons $N_P = F_P \tau_{L\text{-}av} A_P$ ≅1.6×10^9, which cross the GaN layer d and correspond to the YG-L signal integration time $\tau_{L\text{-}av}$ =10 ms for a single laser pulse. The efficiency κ_P of a single proton generation is obtained to be $\kappa_P = n_P/N_P$≅1.3×10^7 cm^{-3} per proton or $\kappa_P A_{pr}$=40 carrier pairs per a micrometer of layer depth per proton.

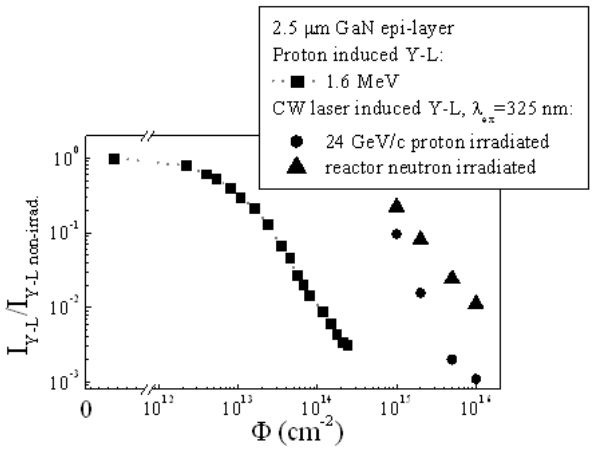

Fig. 3.26. Fluence dependent variations of the intensity $I_{YG\text{-}L}$ of the yellow-green (YG-L) luminescence for 1.6 MeV (diamonds) and 24 GeV/c (stars) proton and for reactor neutron (crosses) irradiated GaN epi-layers. Here, peak intensity $I_{Y\text{-}L}$ obtained for the irradiated samples is normalized to that recorded in the non-irradiated material [A15].

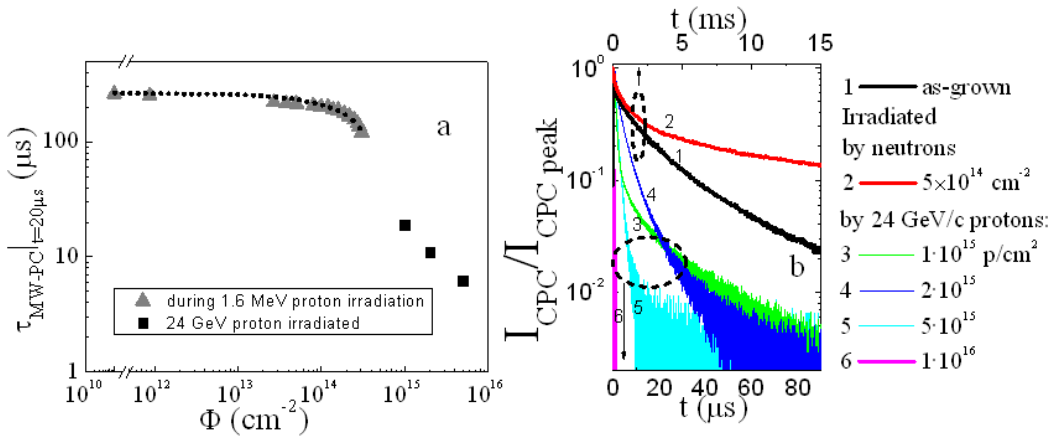

Fig. 3.27. a - fluence dependent variations of the instantaneous SER decay lifetimes measured in situ during irradiation by 1.6 MeV/c protons (hollow circles) and by post-irradiation measurements of GaN samples, irradiated with 24 GeV/c protons (stars). b - variations of the C-PC and MW-PC transients recorded for GaN samples irradiated with different energy hadrons and with various fluences are illustrated [P4].

A reduction of the peak intensity for YG-L spectral band as a function of irradiation fluence is illustrated in Fig. 3.26. The destruction of a net of these point defects is inferred from the evolution of PI-L bands (Fig. 3.26, diamond symbols). This hypothesis is corroborated by the clearly observed increase of the degree of disorder (a reduction of α) in GaN material. Alternatively to interpretations [52] of the B-L origin, the B-PI-L can also be attributed to the rather high density of dislocations, which are more resistant to the radiation destruction.

The efficiency κ_P of a single proton generation is obtained to be $\kappa_P=n_P/N_P\cong1.3\times10^7$ cm^{-3} per proton and $\kappa_P A_{pr}=40$ carrier pairs per a micrometer of layer depth per proton. This $\kappa_P A_{pr}=40$ μm^{-1}p^{-1} value is close to those values for wide-gap materials, listed in Ref. [123]. The defect production rate has been evaluated from the evolution of YG-PI-L reduction as a function of fluence (Fig. 3.26). The YG-PI-L decrease can be explained through the reduced excess carrier density $n_P=g_P\tau_{rd}$ at fixed generation rate g_P ascribed to invariable proton flux. This reduction of initially generated excess carrier density appears due to shortening of the carrier capture lifetime τ_{rd} via density of the radiation induced defects $N_{rd}=1/\sigma_{rd}\tau_{rd}\nu_T$. The N_{rd} density can be

evaluated using the typical parameters of capture cross-section σ_{rd}~10^{-14} cm^2 and thermal velocity v_T~10^7 cm/s. The PI-L intensity decrease is implied to be observable when τ_{rd} becomes shorter than $\tau_{PI\text{-}L}$, i.e. $\tau_{rd} << \tau_{PI\text{-}L}$. For the non-irradiated GaN samples, values of the instantaneous lifetime ascribed to the TR-L decay hint that density N_{rd} of radiation defects can be resolvable in the range of $N_{rd0} \cong 2\times10^{11}$ cm^{-3}. By analyzing the reduction rate within a curve of changes of the YG-L peak values in Fig. 3.27, the production rate $K_P = \Delta N_{rd}/\Delta\Phi \sim \Delta I_{YG\text{-}L}/\Delta\Phi$ of radiation defects is estimated to be $K_P \cong 0.6$ cm^{-1}. This implies that proton irradiation determines both the creation of the specific radiation defects with rate of $K_P \cong 0.6$ cm^{-1} and the modification of the material structure by increasing its disorder. The latter feature can be deduced from the observed decrease of value of the stretched-exponent index. The degree of disorder determines the character of carrier diffusion and trapping, thereby influencing a redistribution of carrier flows through radiative and non-radiative decay channels.

3.3.2.2. Ex-situ analysis under irradiation of different energy hadrons

A wider range of fluences for the analysis of the variation of the parameters of radiative and non-radiative recombination can be covered by post-irradiation measurements of the photoconductivity and photo-luminescence characteristics (Figs 3.26 and 3.27). The same waveform of C-PC and MW-PC transients were observed (inset for Fig 3.27). This result implies that the dispersive transport prevails in the investigated GaN epi-layers irrespective of layer thickness and irradiation fluence. The in situ (diamond symbols) and ex situ (stars and crosses) changes of yellow-green luminescence (YG-L) intensity are compared in Fig 3.26. It can also be deduced that the slopes of clearly distinguishable reduction for both carrier lifetime (Fig 3.27) and YG-L (Fig 3.26) are nearly the same in characteristics measured using in situ and post-irradiation regimes. Nevertheless, the threshold fluence values for 1.6 MeV protons (diamond symbols) and for reactor neutron (crosses) as well

as for 24 GeV/c protons (stars) are shifted within the fluence scale. This can be explained through different interaction cross-sections for the penetrative hadrons (24 GeV/c protons and reactor neutrons) and nearly stopped ones (1.6 MeV protons) within GaN epi-layer depth.

Summary for the chapter

The nitrogen and nickel are the main impurities those govern the non-radiative recombination of the excess carrier with characteristic lifetimes in the range of 0.4-2.4 ns. The nitrogen ascribed cross-sections of carrier capture and photo-ionization are obtained to be $\sigma_{R,N}=(2–12.5)\times10^{-18}$ cm^2, evaluated by combining the measured values of lifetimes of the non-radiative recombination, the absorption coefficient and the concentration of the spin-active centres. The nickel attributed cross-sections of carrier capture are estimated to be $\sigma_{R,Ni}=(0.8–1.3)\times10^{-15}$ cm^2, as evaluated by using the measured values of lifetimes and the concentration of the spin-active centres. It has been inferred that the nickel precipitates and iron-nickel and nickel macroscopic inclusions can also be responsible for the rapid non-radiative recombination processes. However, these macroscopic defects contain low concentration. Profiling of the carrier lifetime, the simultaneous detection of the MW-PC and PL signals collected from the same excitation area, and the results of analysis of the inherent MW-PC and PL decay times imply that the clustering areas (within wafer plane) for the nitrogen and nickel impurities coincide. However, the nitrogen impurities mainly act as the point defects, while nickel precipitation has also been clarified. Values N_{Ni} extracted from ESR spectra represent only a wafer volume averaged concentrations, while local concentrations of N_{Ni} within metal clusters can be significantly larger. The green-yellow PL of the rather long duration ~ 2 μs is ascribed to the action of the radiative recombination centres attributed to the nitrogen and nickel complexes. The measured PL decay lifetimes lead to the time of 1.9 μs for the main diffusion limited decay mode of the carriers which recombine on wafer surfaces. The lifetime of the diffusion limited surface recombination allows

estimating of the ambipolar diffusion coefficient of D_a=46 cm^2/s at room temperature for wafers of thickness ~300 μm

The profiling of the microwave probed photoconductivity transients and of the time resolved photoluminescence spectra has synchronously been performed on the synthetic diamond wafer samples in order to clarify correlation of the distribution of the grown-in defects and carrier radiative and non-radiative recombination channels. The distribution of microscopic characteristics of the grown-in defects has been correlated with carrier lifetime and TR-PL lateral profiles as well as with ESR and FTIR spectral parameters.
The pulsed photo-ionization spectra, those directly represent the photo-ionization signals obtained for various diamond materials, appeared to be well approximated using a simple Lucovsky's model. Additionally, the simultaneous measurements of carrier lifetimes using the PPI technique allow to control of the photo-activation/photo-neutralization of defects involved into photo-ionization processes. The step-like photo-ionization spectra contained up to seven spectral peaks for HPHT material while photo-ionization spectra for CVD diamond were composed of two peaks. These peaks have been attributed to a-C and substitutional N impurities in CVD diamond. For HPHT material, the photo-ionization spectral steps have been ascribed to a-C, N-vacancy and Ni- associated complexes. Thus, nitrogen and nickel attributed defects in HPHT diamond, identified by combining ESR spectroscopy, appeared to be the photo-active centres.

The crystalline structure defects as vacancy and anti-site and carbon impurities have been discriminated in both HVPE and MOCVD GaN materials by photo-ionization (PPI) spectroscopy. Fe impurities induce the dominant deep centres in HVPE samples as identified from PPI and ESR spectra, while C impurities are photo-active centres in MOCVD GaN samples. Existence of high density of metallic impurities in semi-insulating GaN material is the main factor for short carrier lifetime values in the range of 2–20 ns, as determined from MW-PC transients examined on HVPE GaN. The O-DLTS technique, using continuous wave UV light illumination has been applied for

spectroscopy of the GaN parameters of the deep levels ascribed to technological defects. Five traps with thermal activation energies in the range from 0.15 eV to 0.54 eV have been indented from O-DLTS spectra, and these deep centres can be ascribed to the technological defects related to V_N vacancies, V_N-V_{Ga} complex, carbon C_{Ga} impurity and N_{Ga} anti-site. The carbon impurity ascribed centres seem to be involved in both photo-ionization and thermal emission processes.

It has been revealed that proton irradiation induces both the creation of the specific radiation defects and the modification of the GaN material structure by increasing its disorder. The dispersive transport prevails in the investigated GaN epi-layers irrespective of layer thickness and irradiation fluence. The in situ and ex situ variations of the yellow-green luminescence intensity in GaN epi-layers indicate different threshold of material damage by penetrative (24 GeV protons and reactor neutrons) and nearly-stopped (1.6 MeV protons) hadrons. It can also be deduced from the slopes of parameter dependence on fluence that clearly distinguishable reduction for both carrier lifetime and YG-luminescence appear at nearly the same threshold fluence measured using by in situ and post-irradiation regimes.

IV. Modelling and profiling of sensor signals

Analysis of particle detector operation is commonly performed on the basis of consideration of the injected charge drift induced Ramo's current [6, 26, 27]. The current transients are widely examined in order to reconstruct an electric field distribution within the active layers of particle detectors [107, 108]. In the heavily irradiated detectors, a sensor signal can be considerably modified by the injected charge trapping due to radiation defects introduced under long irradiation exposure of the particle detectors. Profiling of both the carrier recombination centres [109, 110] and the injected charge drift velocities [110, 112-116] can be performed by a cross-sectional scan of the photoconductivity and drift current transients. However, a simplified analysis [6, 18, 108] of the drift current transients in detector junction structures (e.g., by considering only the monopolar drift of the injected charge, by using an average electric field integrated over all the depth of the possible drift region instead of the acting field, by including the carrier trapping/recombination only in the drift component and ignoring drift velocity changes, while the induction current depends on any change of charge within the inter-electrode volume, etc.) is usually applied for the interpreting of the detector signals.

The most general consideration is based on Maxwell's equations for matter. To describe the transient electrical characteristics in matter, the static and dynamic approaches exist [116]. The static theories are devoted to description of a drift velocity versus electric field characteristic. The common feature of static and quasi-steady-state approaches is a consideration of only the static and uniform electric fields. The most general dynamic theories deal with the charge transport properties under dynamic conditions when electric field varies in time and space. However, in most of approaches in analysis of the operational features of semiconductor devices the paradigm of drift current description is based on consideration of the first Poisson's equation with either the continuity equation or drift-diffusion current model, which actually can be ascribed to quasi-steady state approaches. The first Poisson's equation calibrates the charge in the system, but an electric field of an injected drifting

charge is often ignored. Charge balancing through the changes of image charge leads to an appearance of electric fields varied in time and space. An example can be a consideration of recombination models and continuity equation, where necessary to precisely include the balance of charged carrier flows, of group velocity and of electric fields [17]. The main inconsistency of such models appears due to non-calibrated potential in field equations, i.e. by ignoring of the image charge. The main relation of electrostatics requires the unambiguous correlation between the charge and potential. This correlation is calibrated by the second Poisson's integral including impact of the image charge, which is actually provided by external source. For non-calibrated consideration of the drift-diffusion approximation, this approach is only valid for partial description, - for instance, drift-diffusion can be applied for description of current in the transitional layers nearby the field discontinuity interfaces (e.g. electrodes) after rapid transitional processes of field discontinuity drift are finished or balanced.

The Ramo's derivation [26] gives an algebraic form of current expression obtained from the principles of simultaneous conservation of the electrostatic energy or reciprocity principle [27], of charge and of charge momentum ($q\mathbf{v}$) for the complete closed circuit with fixed electrodes. It has been proved that equal fields [27] superpose in modification of time varied current due to a drifting charge. These fields are time and drifting charge position dependent. Thereby Shockley-Ramo's theory should be ascribed to dynamic models. Usage of Ramo's current expression by ignoring of induction field [18, 108, 110, 112-115] leads usually to a static model in description of drift velocity.

In this work, the analysis of the electric field distribution due to the injected bipolar domain of the surface charge drifting in a fully depleted detector has been presented. In his chapter, the principles of analysis is briefly presented and addressed to interpretation of the detector current profiling, while detail derivation of the applicable equations for general consideration of sensors signals is published in article [A3]. This analysis is based on the consideration of transients of the induced currents in junction structures by the

injected charge [118]. Several regimes of the rather small charge drift and trapping as well as the large charge bipolar drift proceeded by ambipolar diffusion have been examined. The aim of this study was to distinguish the role of the non-linear effects (such as possible avalanche processes nearby the electrodes due to strong electric field) and the inherent current profiles (due to the injected charge drift) which are caused by varied injection location within detector cross-section. The next goal of this investigation was to clarify whether the radiation damage of the detector material leads to the transformation of the device layered structure (which would be responsible for the redistribution of fields inside it) or this radiation damage leads to a simple prevailing of the capture of the injected carriers on the radiation introduced traps.

Drift velocity changes in time have been considered by solving the kinetic equation including the drifting charge and external voltage source induced surface charge fields. It has been predicted in Ref. [118, A3] and shown in this work that the double-peak current transients can be inherent due to a transform of the injected charge bipolar drift to a monopolar drift regime. Thereby, profiles of the current density, obtained varying the charge injection position within a cross-section of a detector, contain a minimal current value, - within the current (peak value) dependence on the position of charge injection within detector active layer (inter-electrode space d), ascribed to a pure bipolar drift regime. Complementarily, duration of current transient pulses varies due to different charge domain transit time attributed to the bipolar and monopolar drift components, respectively.

4.1. Description of transient signals for profiling of sensor current

The analysis of the injected charge (q) domain drift current (ICDC) transients has been performed on the basis of the charge, the charge momentum (qv_{dr} i.e. drift current continuity $i=qv_{dr}S/d$ with an instantaneous drift velocity v_{dr}) and energy conservation [118]. The consideration has been made by analyzing surface charge vectors, similar to field analysis using

surface charges in Ref. [119] (Fig. 4.1.(c)) of the injected charge q with $\mathbf{E_q}=\mathbf{n_q}q/\varepsilon\varepsilon_0$ and of the surface charge σ on electrode with $\mathbf{E_\sigma}=\mathbf{n_\sigma}\sigma/\varepsilon\varepsilon_0$ ascribed to the external voltage (U) source ($q_C=C_gU$) modified by the electrostatic induction (due to the injected charge). Here, q, q_C and σ denote the surface charge density; ε and ε_0 is the material and vacuum permittivity, respectively; **n** is a vector of the normal to a single-side surface of the drifting surface charge domain; C_g is the geometrical capacitance of the system attributed to a unite of its area. The grounded circuit (with zero charge and potential on the grounded electrode [163]) and velocity vectors of allowed directions of motion for the definite polarity of charge (under the electrostatic field) are considered; therefore, the single-side surfaces are important. Details are published in our article [A3]. The finite area S electrode system is considered at assumption $S^{1/2}>>d$ relative to an inter-electrode spacing d. Then, drift of the injected q charge can be described through the changes in time t of its dimensionless position $\psi(t)=X_q(t)/d$, within a scalar representation. Here, X_q is the instantaneous position of surface charge domain. The generalized distance until the end of drift ψ_q^* for the domain, can also be defined through this instantaneous position: e.g., $\psi_h=X_h/d=\psi_h$ for holes and $\psi_e^*=1-(X_{q,e}/d)=1-\psi_e$ for electrons, respectively, within the accepted coordinates. Introduction of the dimensionless instantaneous position and the distance to drift, leads to the immediate transform of the equations for the drift velocity field and current density. The current density is considered as the σ charge changes in time domain. Then, solutions of these equations are represented by the characteristic times: the $\tau_{Mq}=\varepsilon\varepsilon_0 d/\mu q$ of the dielectric relaxation of a drifting charge which characterizes a capability of the injected charge (for instance, electrons, $-q$), localized at the initial coordinate, to induce surface charge $(+q)$ on the high potential electrode through an electric displacement field; the characteristic time $\tau_{TOF}=d^2/\mu U$ of the carrier free flight through a spacing d with the initial velocity acquired at opposite electrode due to the acting voltage U, - both τ_{Mq} and τ_{TOF} vary due to changes of the injected charge position and acting voltage

drop during a drift within the inter-electrode space with voltage source field; and the material dielectric relaxation time $\tau_{M,NDef}=\varepsilon\varepsilon_0/\mu e N_{D,ef}$ at an assumption the effective dopant density $N_{D,ef}=n_0$ is in accordance with equilibrium carrier density n_0. Here, μ is the mobility of the definite type carriers. The equality of these $\tau_{TOF}=\tau_{Mq}$ which are the characteristic times of action and reaction, respectively, implies a consequence of the electrostatic approach.

On the basis of the assumptions discussed (details can be found in Ref. [A3]), the current density (for a drift of the electron monopolar domain) and drift velocity (rate) field is described in the scalar form as [118]:

$$j=\frac{d\sigma}{dt}=q_e\frac{1}{d}\frac{dX_e}{dt}=q_e\frac{d\psi_e}{dt}, \tag{4.1}$$

and

$$\frac{d\psi_e}{dt}=\frac{1}{\tau_{TOF}}+\frac{1}{2\tau_{M,NDef}}+\psi_e\left(\frac{1}{\tau_{Mq}}-\frac{1}{\tau_{M,NDef}}\right), \tag{4.2}$$

respectively. It can be noticed that expression (Eq. 4.1) for the current density coincides with that Ramo's derived. The kinetic equation (Eq. 4.2) for the drift rate should satisfy the boundary conditions for the drift time $t_{dr,}$ as:

$$\psi_e=\psi_{e0}\ for\ t=0;\quad \psi_e=1\ for\ t=t_{dr}. \tag{4.3}$$

The solution of the Eq. (4.2) with boundary conditions Eq.(4.3) yields:

$$\psi_e(t)=\psi_{e0}\exp[-\frac{t}{\tau_{Mq}}(\frac{\tau_{Mq}}{\tau_{M,N_{Def}}}-1)]+\frac{\frac{1}{\tau_{TOF}}+\frac{1}{2\tau_{M,N_{Def}}}}{\frac{1}{\tau_{M,N_{Def}}}-\frac{1}{\tau_{Mq}}}\{1-\exp[-\frac{t}{\tau_{Mq}}(\frac{\tau_{Mq}}{\tau_{M,N_{Def}}}-1)]\}, \tag{4.4}$$

$$\text{for}\quad \tau_{Mq}>\tau_{M,N_{Def}};$$

and

$$t_{dr} = \frac{\tau_{Mq}}{(\frac{\tau_{Mq}}{\tau_{M,N_{Def}}} - 1)} \ln \frac{\frac{\frac{1}{\tau_{TOF}} + \frac{1}{2\tau_{M,N_{Def}}}}{\frac{1}{\tau_{M,N_{Def}}} - \frac{1}{\tau_{Mq}}} - \psi_{e0}}{\frac{\frac{1}{\tau_{TOF}} + \frac{1}{2\tau_{M,N_{Def}}}}{\frac{1}{\tau_{M,N_{Def}}} - \frac{1}{\tau_{Mq}}} - 1}, \quad \text{for} \quad \tau_{Mq} > \tau_{M,N_{Def}}. \tag{4.5}$$

Representation of these solutions for $\tau_{Mq}=\tau_{M,NDef}$ and $\tau_{Mq}<\tau_{M,NDef}$ can be found in [118 and A3]. It can be noticed in Eq.(4.4) that neither drift velocity nor acceleration is constant for the electrostatic induction moderated drift during $0\leq t \leq t_{dr}$. However, in the case of $\tau_{Mq}=\tau_{M,NDef}$, the dimensionless position $\psi_e(t)$ increases linearly with t in the range of $0\leq t\leq t_{dr}$, which is directly determined by τ_{TOF} and $\tau_{M,NDef}$.

The τ_{Mq} depends on the surface density q of a drifting domain. This drifting surface charge also acts as a voltage sharing element. Therefore, τ_{TOF} should also be rearranged including the acting voltage U_C, if a small surface density q charge drifts (e.g. for the initial instant $\sigma=q_C>>q$). The acting voltage can be evaluated from the energy conservation for the one-dimensional drift as

$$m_{eq} n_{eS} (\frac{d\psi_e}{dt} d)^2 = q_e U_C \ . \tag{4.6}$$

Here, m_{eq} is the effective mass of the elementary charge carrier, $n_{eS}=N/S$ is the surface density of N carriers within a drifting domain.

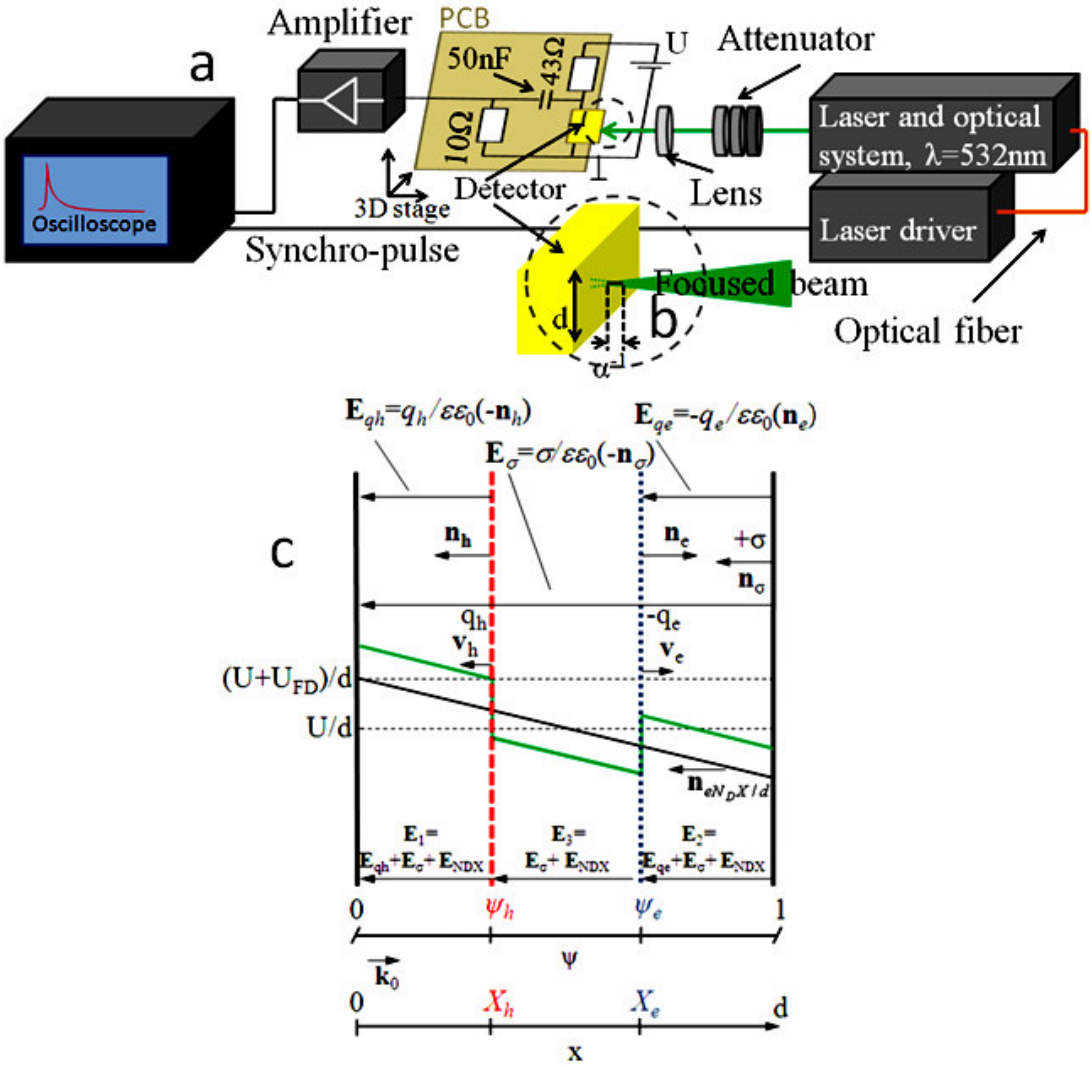

Fig. 4.1. Sketch of the electrical (a) and optical (b) measurement schemes (zoom). (c) – instantaneous field distribution for bipolar charge drift. Symbols denote as follows: $X_{e,\,h}$ is the instantaneous position of the drifting one-sided surface charge domain of the electrons ($-q_e$) or holes (q_h) (with normal vectors $\mathbf{n}_e$ and $\mathbf{n}_h$), respectively; $\mathbf{E}_1 = \mathbf{E}_{qh} + \mathbf{E}_\sigma + \mathbf{E}_{NDX}$ is the electric field caused by the superposition of the hole charge (q_h) domain, the surface (of an area S) charge ($+\sigma$, with a normal vector $\mathbf{n}_\sigma$) on the high potential electrode and the local surface charge introduced to represent the electric field at x created by a bar (of a width (d-x)) of the bulk ion charge (with a normal vector $\mathbf{n}_{eNDX}$); $\mathbf{E}_2 = \mathbf{E}_{qe} + \mathbf{E}_\sigma + \mathbf{E}_{NDX}$ is the electric field caused by the superposition of the electron charge ($-q_e$) domain, the surface charge ($+\sigma$) and the local surface charge of the ion bar; $\mathbf{E}_3 = \mathbf{E}_\sigma + \mathbf{E}_{NDX}$ is the superposition of field between the electron and hole domains and the surface charge of the ion bar, -an arrow at E_{NDX} shows a direction of E_{NDX} field not its value; $\mathbf{v}_{e,h}$ is the instantaneous velocity vector of a drift of the surface charge domain $-q_e$ or q_h, respectively; d is the inter-electrode distance; ε and ε_0 are the material and vacuum dielectric permittivity, respectively; $\mathbf{k}_0$ is the unit ortho-vector in the uni-directional coordinate system; ψ_h and ψ_e are the dimensionless, normalized positions of the drifting hole or electron domains, respectively.

The three-dimensional drift should be considered due to boundary effects appeared through the small charge and the small geometrical measures of the injected charge domain. Then, the current is changed not only due to the domain drift, but also by the carrier diffusion within directions, perpendicular (*y, z*) to a drift (*x*) direction (due to the sharp gradients of density caused by finite electrode can be ignored within the first either small density or small diameter of an excitation spot).

The boundary effects on a order approximation at accepted assumption of $S^{1/2}>>d, \phi$. Carrier diffusion processes for a fixed width ϕ of an injection spot can be approximated by a solution of the two-boundary diffusion task [110], represented as

$$n_{e,S}(t,y,z) = \sum_{m1,m2=1}^{\infty} A_{m1,m2} \sin(\eta_{y,m1} y + \varphi_{m1}) \sin(\eta_{z,m2} z + \varphi_{m2}) \exp[-D(\eta_{y,m1}^2 + \eta_{z,m2}^2)t] \quad (4.7)$$

and expressed through the spatial frequencies of the $\eta_{y,z}$ obtained from the solutions of the transcendental equations of the type

$$ctg\ (\eta\phi\ ) = \frac{D\,\eta}{s}\ . \quad (4.8)$$

Here, *D* is the diffusion coefficient of carriers, *A* denotes the norm-coefficients, φ denotes the phase shifts, the spatial frequency $\eta_{y,z}$ modes ($\sin\eta_y y$) are considered (in analogy with frequency in time domain ($\sin\omega t$)) for the task of surface recombination velocity $s=D/L_D$, which (*s*) can be related to Debye length L_D.

Another peculiarity in solution of the drift rate equations appears if carrier capture processes are significant. The charge density change in time can be approximated by $q(t)=q_0\exp(-t/\tau_C)$, which leads to $\tau_{Mq}(t)=\tau_{Mq0}\exp(t/\tau_C)$, $\tau_{M,NDef}(t)=\tau_{M,NDef0}\exp(t/\tau_C)$ and re-arrangement of equations of the type Eqs. (4.1 and 4.2) to such as

$$j = q_e(t)\frac{\partial \psi_e(t)}{\partial t} - \frac{\partial q_e(t)}{\partial t}(1-\psi_e(t)) - \frac{ed}{2}\frac{\partial N_{D,ef}(t)}{\partial t}, \quad (4.9a)$$

$$\frac{d\psi_e}{dt} - \psi_e\left(\frac{1}{\tau_{Mq,e}(t)} - \frac{1}{\tau_{M,N_{Def}}(t)}\right) - \frac{1}{\tau_{TOF,e}} - \frac{1}{2\tau_{M,N_{Def}}(t)} = 0\,. \qquad (4.9b)$$

These equations can only be solved numerically, in the general case. However, for the $\tau_C << \tau_{TOF}$, the carrier capture component prevails within these equations.

The bipolar charge initial injection causes the next peculiarity in the analysis of the recorded waveforms of the current transients. This injected neutral domain is separated into electron *(q_e)* and hole *(q_h)* sub-domains under the diffusion and external voltage source field (q_C) action. These domains drift in the opposite directions, while diffusion in these (along *x* axis) directions can be ignored if applied voltage is sufficient (i.e. $q_c >> q$). The current density module for the bipolar drift is expressed by

$$j_b = \frac{d\sigma_{e-h}}{dt} = |q|\left(\frac{d\psi_e}{dt} + \frac{d\psi_h}{dt}\right), \qquad (4.10)$$

at the same assumptions, as in derivation of Eq. (4.1). The electrostatic induction (as $|q|=|q_e|=|q_h|$) is then correlated in time (τ_b) for the bipolar drift process, if carrier capture can be ignored. The bipolar drift rate equations can be represented as:

$$\frac{\psi_0}{-\frac{d\psi_h}{dt}} = \frac{(1-\psi_0)}{\frac{d\psi_e}{dt}} = \tau_b, \quad for \quad \tau_b = \tau_{dr,e} = \tau_{dr,h}, \qquad (4.11A)$$

$$\frac{\psi_0}{-\frac{d\psi_h}{dt}} = \frac{(1-\psi_e)}{\frac{d\psi_e}{dt}} = \tau_{dr,h}, \quad for \quad \tau_b = \tau_{dr,h} < \tau_{dr,e}, \qquad (4.11B)$$

or

$$\frac{\psi_h}{-\frac{d\psi_h}{dt}} = \frac{(1-\psi_0)}{\frac{d\psi_e}{dt}} = \tau_{dr,e}, \quad for \quad \tau_b = \tau_{dr,e} < \tau_{dr,h}\,. \qquad (4.11C)$$

The regime (described by Eq. 4.11A) of pure bipolar drift, for the synchronous existence of both type carriers within the entire inter-electrode spacing, can

only be realized for a single definite point of the bipolar charge domain injection ψ_0. While mixed the bipolar processes appear when bipolar drift (within current pulse) changes to either a monopolar drift of electrons' domain (described by Eq. 4.11B) after holes reach a grounded electrode or it becomes a monopolar drift of holes domain (expressed by Eq. 4.11C) after electrons reach the high potential electrode. Such a consideration can be understood for a moving system of coordinates: one of sub-domains drifts in a system which beginning is shifted by the charge domain drifting in the opposite direction. The entire velocity of such a drift is a sum of velocities of the sub-domains. Solutions obtained (e.g. for Eq. (4.11B)) in time domain τ_b are as follows:

$$\begin{aligned} &\frac{d\psi_h}{dt} = -\frac{\psi_0}{\tau_{tr,h}}; \qquad \frac{d\psi_e}{dt} = \frac{1-\psi_e}{\tau_{tr,h}} \\ &\psi_h = \psi_0\left(1-\frac{t}{\tau_b}\right); \quad \psi_e = \psi_0 \exp\left(-\frac{t}{\tau_{tr,h}}\right) + \left[1-\exp\left(-\frac{t}{\tau_{tr,h}}\right)\right] \end{aligned} \quad . \qquad (4.12)$$

These solutions satisfy the boundary conditions:

$$\begin{aligned} &\psi_h\big|_{t=0} = \psi_0; \quad \psi_e\big|_{t=0} = \psi_0; \\ &\psi_h\big|_{t=\tau_{tr,h}} = 0; \quad \psi_e\big|_{t=\tau_{tr,h}} = [1-exp(-1)] + \psi_0\, exp(-1) \\ &\qquad\qquad \psi_e^{*0}\big(_{t=\tau_{tr,h}}\big) \equiv [1-exp(-1)] + \psi_0\, exp(-1) \end{aligned} \quad . \qquad (4.13)$$

Here, ψ_e^{*0} serves as the start position for the monopolar drift of the electrons domain, just during an instant of the domain of holes disappearing at a grounded electrode. The time τ_{bB} of the initial bipolar drift is obtained by integrating the expression for drift velocity (using Eqs. 4.11, 4.12 and 4.13) as:

$$\begin{aligned} &\frac{d\psi_h}{dt} = \frac{\mu_h}{d} E_1; \\ &\tau_{bB} \equiv \tau_{tr,h} = \frac{\psi_0 \tau_{TOF,h}}{1+\frac{\mu_h}{\mu_e}\tau_{TOF,h}\left[\frac{1}{2\tau_{M,NDef}} - \frac{\psi_0}{2\tau_{M,NDef}} + \frac{1}{\tau_{Mq,e}} + \frac{1}{\tau_{Mq,e}}(1-\psi_0)(e^{-1}-1)\right] - \frac{\psi_0}{2}\frac{\tau_{TOF,h}}{\tau_{Mq,h}}} \end{aligned} \quad . \qquad (4.14)$$

For the proceeded monopolar drift of electrons with ψ_e^{*0} as an initial position, the current density, in the case of the mixed regime (Eq. 4.11B), is expressed by using solution Eq.(4.1) as

$$j(t)=\begin{cases} j_1=\dfrac{q_e}{\tau_{tr,h}}\{\psi_0[1-\exp(-\dfrac{t}{\tau_{tr,h}})]+\exp(-\dfrac{t}{\tau_{tr,h}})\}, \quad for \quad 0\le t\le\tau_{tr,h}; \\ j_2=\dfrac{q_e}{\tau_{Mqe}}[\exp(-\dfrac{\tau_{Mqe}}{\tau_{M,NDef}})\dfrac{t}{\tau_{Mqe}}(\dfrac{\tau_{Mqe}}{\tau_{TOF,e}}+\dfrac{1}{2}\dfrac{\tau_{Mqe}}{\tau_{M,NDef}}-1+\dfrac{v_0\tau_{Mqe}}{d})], \quad for \quad 0\le t\le\tau_{e,mon} \end{cases} . \quad (4.15)$$

Here, the step-like change of field and current density would be obtained for an instant of holes arrival to the grounded electrode. To validate the charge, charge momentum, and energy conservation, the coordinate transform should be performed, to stitch solutions obtained in the moving (τ_{bB} time domain) system to that obtained (Eq. 4.1) for a still system of coordinates. This transform should include the charge induction on the electrodes, the drift velocity conservation and the coordinate relations, which can be represented as:

$$\begin{aligned} &\sigma^+=\sigma+q; \\ &\frac{d\psi^+}{dt}=(\frac{d\psi_h}{dt}+\frac{d\psi_e}{dt})\Big|_{\tau b} \quad ; \\ &\psi^+=-\frac{1}{1-\dfrac{\tau_{Mq,e}}{\tau_{M,NDef}}}+(\psi_e-\psi_{e_e}^{*0}); \quad \tau_{Mq,e}<\tau_{M,NDef} \end{aligned} . \quad (4.16)$$

These transforms relate the "new" ψ^+ still system for the proceeded monopolar drift analysis, after the charge induction procedure is accounted for and velocities are matched. The entire duration τ_P of the current pulse contains both phases:

$$t_P=\tau_{bB}+\tau_{e,mon}, \quad (4.17)$$

of the bipolar (τ_{bB}) and monopolar ($\tau_{e,\,\mathrm{mon}}$) drift of electrons. The identical procedures, similar to those illustrated through Eqs. (4.12-4.16) for the case of the mixed drift with the initial bipolar drift during a hole sub-domain drift time (regime defined by Eq. 4.11B), should be performed in profiling of current transients. All the possible mixed drift regimes (Eqs. 4.11A-4.11C) appear using the scan of the initial injection location.

For the mixed drift regime, the transformation of coordinates from moving one to the laboratory system is necessary (Eqs. (4.16)). Then, the kinetic equation of type Eq. (4.2), derived for the monopolar drift in laboratory system of coordinates with zero initial velocity, should be transformed including Eqs. (4.16). There, continuity of current, equivalent to the charge momentum conservation $q(v_{h,b}+v_{e,b})=qv_{e,mon}$ for the instant of hole arrival to an electrode, and a non-zero initial velocity should be included. In the general case, the one-dimensional approach becomes invalid for the drift current rigorous analysis. Nevertheless, the approximation of the one-dimensional drift can be obtained through replacing the coefficients (ratios of characteristic times) $R_e=\tau_{Mq,e}/\tau_{TOF,e}$ and $R_{NDef,e}=\tau_{Mq,e}/\tau_{M,NDef}$ in the re-arranged Eq. (4.2) using Eqs. (4.16) by $R_{ef,e}=(\tau_{Mq,e}/\tau_{TOF,e})(U_{C,ef,e}/(U+U_{FD}))$ and $R_{ef,NDef,e}=(\tau_{Mq,e}/\tau_{M,NDef})(U_{C,ef,e}/(U+U_{FD}))$ using the approximation $U_{C,ef,e}=1.225q_ed(\psi_e^{*0})^{1/2}/\varepsilon\varepsilon_0$ for electrons. Analogically, in the re-arranged equation for hole monopolar drift, ratios of R_h and $R_{NDef,h}$ are approximated by $R_{ef,h}=(\tau_{Mq,h}/\tau_{TOF,h})(U_{C,ef,h}/(U-U_{FD}))$ and $R_{ef,NDef,h}=(\tau_{Mq,h}/\tau_{M,NDef})(U_{C,ef,h}/(U-U_{FD}))$ using $U_{C,ef,h}=1.995q_hd(\psi_h^{*0})^{1/3}/\varepsilon\varepsilon_0$. These corrections should be made to account for the acting voltage U_C which changes with instantaneous position of drifting domain. The numerical coefficients in approximations of the $U_{C,ef}$ have been evaluated by simulations of the continuity of the drift velocity and the current. In capacitor type detectors, these coefficients (being of values in the range of 1.15–1.25) represent nearly equal distribution of the kinetic energy between the degrees of freedom in three-dimensional motion, while, in the junction detector, the coordinate dependent field distribution introduces the asymmetry in the drift velocity dependence on the instantaneous position of the drifting charge.

Signal registration circuit (namely, load resistor R_L) inevitably transforms transient shape due to voltage on detector changes depending on current value within circuit. In more general case, the transients are described by solutions of the differential equation with variable coefficients, derived as

$$\frac{\sigma(t)}{C_{Sq}(t)} + iR_L = U, \quad with \quad i = S\frac{d\sigma}{dt},$$
$$\frac{1}{C_{Sq}}\frac{d\sigma(t)}{dt} - \frac{\sigma(t)}{C_{Sq}}\frac{dC_{Sq}(t)}{C_{Sq}dt} + \frac{di}{dt}R_L = 0, \quad . \tag{4.18}$$
$$with \quad U_{CR} = U - iR_L, \quad U_{CR} = \frac{\sigma(t)}{C_{Sq}}.$$

This leads to a non-linear differential equation

$$\frac{di}{dt} + (\frac{d\ln SC_{Sq}(t)}{dt} + \frac{1}{R_L SC_{Sq}(t)})i = \frac{U}{R_L}\frac{d\ln SC_{Sq}(t)}{dt}, \tag{4.19}$$

which should be solved by using the relevant initial conditions.

The changes of the injected charge domain drift current (ICDC) transients, simulated by using model sketched within Eqs. (4.1)–(4.19) and varying the initial injection point ψ_0, are represented in Figs. 4.2 and 4.3.

It can be deduced from Fig. 4.2, that the suitable injection location ψ_0 for the pure bipolar drift depends on the injected charge density and the ratio of carrier mobilities. Simulated profiling of ICDC transients in Fig. 4.3 implies that the initial current peak increases with approach of the injection point towards electrodes. This can be explained by a shortening of the bipolar drift duration. The current changes during the bipolar drift stage also show (Fig. 4.3) that sub-domains of the drifting holes and electrons interact via the induced charges on electrodes (mediated through a voltage source).

Therefore, the ICDC pulse duration increases and a peak amplitude falls down with approach of the injection location to the mid of the inter-electrode spacing. This can be explained by the changes of the instantaneous electric field, ascribed to the injected/drifting charges. Thereby an increase of pulse duration (for the injection location which satisfies the pure bipolar drift) can also be understood at an assumption that the amount of drifting charge and charge collection efficiency are invariable.

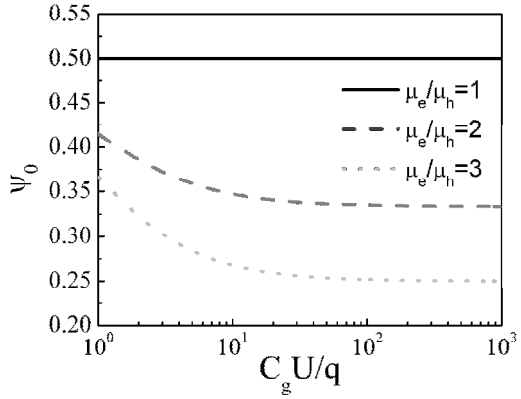

Fig. 4.2. Possible injection location for the pure bipolar drift as a function of the density of the injected charge domain, at condition $U>>U_{FD}$, for different ratios of carrier mobilities and for fixed other parameters, [A9].

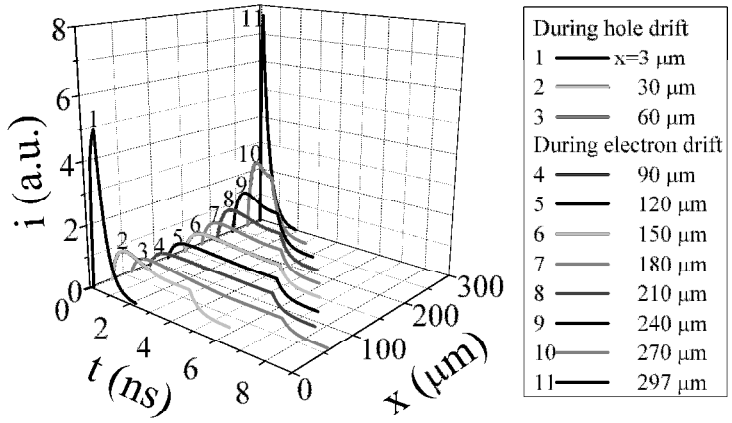

Fig. 4.3. Simulated profiling of the ICDC transients due to the injected charge (3.5×10^{-12} C/cm^2) domain in 300 μm thick n-type conductivity base for U=100 V applied voltage, [A9].

In the analysis of the avalanche effects, the kinetic energy of carriers $mv_x^2/2\geq E_g$ (with qU_C replaced by E_g the forbidden energy gap in Eq. (4.6)) determines the threshold energy for the gain of current. This gain process can be accounted for by introducing the additional generation function $f(t)$ into equations Eq. (4.1) and (4.9) by q replacing as $q(t)=q_0(1+f(t))$.

4.2. Analysis of multiplication factor

Multiplication factor $M(x)$, evaluated as the amount of carrier pair increase due to impact ionization, when a carrier, initially located at x and possessing the sufficient kinetic energy to excite the impact ionization, initiates the cascade multiplication process along its drift trajectory. Multiplication factor is the most important parameter in analysis of the efficiency of the internal gain, as it determines the possible internal amplification and the excess noise factor. Therefore, the multiplication factor *M(x)* is initially considered similarly to well-known Mc Intyre's model [164-167] and applied for analysis of semiconductor devices [168-170]. It is assumed that a single carrier $M(x)=1$ is initially generated at location x within device depth w, and the multiplication of additional pairs appears in the interval $0 \le x' < x < x'' \le w$ due to impact ionization with coefficients of α and β (in cm^{-1}) for electrons and holes, respectively. Let's assume, that holes move a distance x' to the left relative to initial location x while electrons drift to the right from x, using a circuit similar to that analyzed in [171]. Such a drift with multiplication is described by a differential equation for different segments of hole and electron drift as

$$\frac{dM(x')}{dx'} = \begin{cases} -\beta M(x'), \text{ for } & 0 \le x' < x, \\ 0, \quad \text{for } & x' \equiv x, \\ \alpha M(x'), \text{ for } & x > x' \ge w \end{cases}, \tag{4.20}$$

including the directions of motion. This equation in segments should satisfy the boundary (initial, $t=0$) condition $M(x, x')=1$ for $x' \equiv x$. Solution of Eq. (1) with boundary leads to expressions for each segment

$$M(x,x',x'') = \begin{cases} \exp[\beta(x-x')], \text{ for } & 0 \le x' < x, \\ 1, \quad \text{for } & x' \equiv x \equiv x'', \\ \exp[\alpha(x''-x)], \text{ for } & x > x'' \ge w \end{cases}, \tag{4.21}$$

Integrating Eq. (4.20) over the entire range of $0<x<w$ (for a fixed initial location x of a pair), ones obtain

$$M(x) = 1 + \int_0^x \beta M(x') d(-x') + \int_x^w \alpha M(x'') d(x'') . \tag{4.22}$$

This equation coincides with that considered within wide-spread models [164-170]. Inserting solutions Eq.(4.2.) into Eq. (4.22) for the relevant segments, Eq. (4.22) is re-arranged as

$$M(x) = \exp(\beta x) + \exp[\alpha(w-x)] - 1 = 2\exp[\frac{(\beta-\alpha)x}{2}]\exp(\frac{\alpha w}{2})\cosh[\frac{(\alpha+\beta)x-\alpha w}{2}] - 1, \quad (4.23)$$

with boundary values of $M(0)=\exp(\alpha w)$, $M(w)=\exp(\beta w)$ and $M(x)=1$. The obtained Eq.(4.23) indicates that a finite multiplication factor is only possible for the finite width w. Expression for $M(x)$ (Eq. 4.23) appears to be different from the routine McIntires' model (with infinite $M(x)$ value under a single impact ionization event), while it is close (has and *exp*-function form) to multiplication expression derived in Townsend [172] avalanche model.

The pure bipolar drift and multiplication lead to charge collection at electrodes of a set of generations (cascades) of carriers appeared due to impact ionization. Eq. (4.23) represents multiplication obtained for the first generation $M(x,1)$ of multiplied carriers determined by drift of holes and electrons in opposite directions from the initial point x within external field, sufficient for impact ionization. Only single type of carriers (holes or electrons) is collected at relevant electrode. Other counter-partner (for instance, electron, if holes are collected at x=0) of each multiplied pair is separated by diffusion and moves from this electrode and initiates the next generation (cascade) of carrier multiplication. For symmetric pure bipolar process ($\alpha\equiv\beta$, $x=x_h\equiv(w-x_h)_e$, $v_h=v_e$), electrons with initial (at x=0) quantity $e^{\beta x}$-1 generate pairs (during the transit time $\tau_{tr}\cong x_h/v_e$), and the enhanced quantity of pairs reaches (at $x'=x$) value $N_{2,x}=\int_0^x \alpha(e^{\beta x'}-1)dx'$. The holes of these $N_{2,x}$ pairs during the time t interval $\tau_{tr}<t\leq 2\tau_{tr}$ generate the second set of collected charge $M_h(x,2)=\int_0^x \beta N_{2,x}\,dx'$. By considering the same process within $(w-x_h)_e$ path of electron multiplication, the same $M_e(x,2)$ value is obtained. The total quantity of the carriers, attributed to the second generation, is $M(x,2)=2[e^{\alpha x}-1-\alpha x-(\alpha x)^2/2]$. By continuing analysis of the next generations of carriers (multiplication cascades) the multiplication factor for each generation n is derived as

$$M(x,n) = 2[e^{\alpha x} - \sum_{m=0}^{2n-2} \frac{(\alpha x)^m}{m!}] + 1 \qquad (4.24)$$

for the symmetric pure bipolar drift and multiplication process ($\alpha \equiv \beta$, $x = x_h \equiv (w - x_h)_e$, $v_h = v_e$). The cumbersome expressions are obtained for the asymmetric bipolar drift ($\tau_{tr,b} \cong x_h/v_h \cong (w-x_h)/v_e$) with properly adjusted coefficients α and β. In general case of mixed (bipolar proceeded by monopolar) drift regime, the re-calibration of charge on electrodes should be included [171]. The cascade multiplication model predicts a delayed current transient relative to a single transit time process. Here, charge collection gain is obtained as a current integral over increased pulse duration when current is held nearly invariable due to sustained multiplication of carrier pairs. The multiplication factor can be expressed as a ratio of areas beneath the current variation curves over a current pulse, obtained with and without multiplication. The completely inelastic process of carrier pair excess generation is assumed in the cascade multiplication model where drifting carriers transfer their kinetic energy (acquired from the accelerating electric field created by an external voltage source) into the impact ionization energy. Here it is also assumed that the external source is able to support the invariable voltage on electrodes irrespective of the increased current due to carrier multiplication. Thus, the capacity of the external voltage source is an external limiting factor, while the high electric field (sufficient to support the prevailing impact ionization at the end of the injected, non-equilibrium carrier acceleration over its mean free path, – "dead length" [173, 174]) is the internal condition for cascade multiplication (leading to a non-local field model [175]). Then the consideration using electrodynamics can be applied to estimate deterministically the required carrier acceleration. Therefore, the cascade multiplication, dynamic model predicts different expression of the multiplication factor relative to that of traditional [164-170] models, based on steady-state statistical consideration. The latter models can be attributed to the asymptotic ones, where multiplication region is assumed to be very long,

”what is equivalent that number of ionizing collisions per primary carrier transit is infinite” [176].

4.3. Modelling of current transients with carrier multiplication

In particle detectors, reduction of carrier lifetime due to radiation defects should be compensated (at least) by proper multiplication $M(w) > 2$. Both parameters, carrier pair multiplication factor $M(x)$ and carrier lifetime τ, lead to a change of carrier drift velocity $v=w(d\psi/dt)$ with variation of the dimensionless position $\psi=x/w$ due to carrier drift. For instance, changes of a velocity of drifting electrons (using the dynamic consideration, e.g. similarly to [171]) caused by impact ionization with $<M(x)>=m$ and carrier trapping with τ are described by solution of differential equation

$$\frac{d\psi}{dt} = \frac{1}{\tau_{Mq,0}}\psi + \frac{1}{\tau_{TOF}} \cong \frac{\exp(-t/\tau) + m(t)}{\tau_{Mq,0}}\psi + \frac{1}{\tau_{TOF}} \tag{4.25}$$

with boundary conditions $\psi=\psi_0$ for $t=0$ and $\psi=1$ for $t=\tau_{tr}$. Here, τ_{tr} denotes the transit time of a drifting charge of surface density $q=(eR/S)$ with characteristic times of free flight $\tau_{TOF}=w^2/\mu U_w$ and of dielectric relaxation $\tau_{Mq,0}=\varepsilon\varepsilon_0 w/\mu q_e$, respectively, over the definite distance w. Other symbols represent: U_w is the applied on w voltage drop, $\mu\approx(e/m_e)\tau_{tr}$ is the mobility of electrons, m_e and e is the electron mass and elementary charge, respectively; ε_0 and ε is the dielectric permittivity of vacuum and of the material filling the inter-electrode gap, respectively; S is the area of electrode surface, R is the quantity of injected pairs. It can be deduced from Eq.(4.25) that drift velocity depends on dimensionless position ψ of moving charge (due to a change of Coulomb force with distance). Actually, due to different mobilities of holes and electrons, different acting electric fields and velocities appear for holes and electrons. For the pure bipolar drift (Eqs. (4.22-4.24)), the synchronous arrival of electrons and holes to opposite electrodes is held by making drift of electrons and holes with invariable velocity [171]. Thus, to keep the same transit time τ_w ($\tau_w=x/w(d\psi_h/dt)=(w-x)/w(d\psi_e/dt)$), the coordinate and field dependent ratios

of the impact ionization coefficients $\alpha(E,x)/\beta(E,x)=x/(w-x)$ should appear. Really, an event of impact ionization would appear for simultaneous matching of energy and momentum conservation ($mv^2/2=2.3\varepsilon_G+0.7$ (eV) [3], $mv=hk(\varepsilon)+h\kappa_{ph}$). The expressions in the latter parenthesis are written using relation for phonon assisted process in material with forbidden energy gap ε_G defined in eV [55, 177] and drift momentum related to quasi-momentum and the energy band spectrum $k(\varepsilon)$ [55, 177]. Actually, to satisfy energy and momentum conservation for varied acting electric field $E(\psi)$ the spectrum κ_{ph} of the needed phonon filled states should be rather wide. This depends considerably on lattice temperature. For the mixed drift regime, when electrons and holes arrive to electrodes at different time instants, consideration becomes more complicated [171]. Assuming here that conditions for pure bipolar drift are held, every carrier pair carries an elementary charge under arrival to electrodes, and there appear the collected charge $Q_M=e<M|_{\alpha,\beta}>$ and current $i=Q_M/\tau_{tr.}$ Variations of the acting electric field $E(\psi(t))$ in time and as a function of dimensionless position $\psi(t)$ can be determined using the dynamic approach [171].

The dynamic model, including charge induction on electrodes and drift velocity (Eq. (4.25)) changes dependent on drifting charge amount, applied to analysis of cascade processes with multiplication and carrier capture, should take into account scattering of the injected carriers. Impact ionisation can then be considered as a scattering process with varied carrier pair quantity. The scattering dependent parameters, such as carrier mobility, determined for steady-state conditions, can be employed for the first iteration. The drift velocity can alternatively be considered based on solutions obtained for vacuum capacitor. There, a free mean path λ can be assumed to be a characteristic drift distance, i.e. $w=\lambda$ and with characteristic relaxation times $\tau_{TOF,\lambda}$, $\tau_{M,\lambda}$. The free mean path λ can then be estimated statistically by using Chynoweth's law [168-170] for the coefficients of impact ionization, - as $\lambda(E)=\alpha_\infty^{-1}\exp(E_{thr}/E)$, which leads to shortening of λ with enhancement of

acting field E. The acting voltage over a free path before impact ionization, as U_λ, is defined by $U_\lambda = \int_X^{X+\lambda} E(t,X_\lambda)dX_\lambda$, which depends on the amount of a drifting charge and its instantaneous position. The current transient then is comprised of fragments of the injected charge drift over a set of $\eta = w/\lambda$ of free paths. Really, the scattering process with the shortest free mean path λ_{si} should be assumed as the prevailing one: $1/\lambda = 1/\lambda_{si} + \Sigma_{i-1} 1/\lambda_i \approx 1/\lambda_{si}$, if different scattering processes can be assumed as acting in parallel.

To evaluate the possibility and the main regimes to compensate recombination through radiation defects (with carrier lifetime τ) by impact ionization $M(x,n)$ (with free mean path λ_{si}), the simplified assumptions are made: i) the applied voltage U is sufficient to initiate the impact ionization determined by inequality $(m/2)[\{e\tau_{tr,\lambda}(d/\lambda)/m\}(U/d)]^2 > 2.3\varepsilon_G + 0.7$; ii) the pure bipolar drift of carriers takes place, where single pair carries an elementary charge of electron under simultaneous arrival of hole and electron to opposite electrodes, separated by a distance d, i.e.

$$\frac{e_h}{d}\int_x^0 dx' + \frac{e_e}{d}\int_x^d dx'' = e(-\frac{x}{d}) + (-e)(\frac{d-x}{d}) = -e \qquad (4.26)$$

and the total current ascribed to a single pair drift is obtained

$$|i_{eh}| = \frac{e}{\tau_{tr,e}} \quad with \quad \tau_{tr,e} = \tau_{tr,h}. \qquad (4.27)$$

The current generated by pure bipolar drift always exceeds that of the monopolar one due to the shorter transit time, irrespective of that carried charge is the same; iii) the pure bipolar drift regime determines the invariable drift velocity [171]; iv) the pure bipolar drift regime justifies derivation of Eqs. (4.22-4.24) (with initial bipolar charge injection) and application of multiplication factor $M(x,n)$ expressions.

Current variations in time due to collection of each generation n (cascade) of multiplied carrier pairs is obtained by assuming that $x_h = v_h t$ for $(n-1)\tau_{tr} < t \le n\tau_{tr}$

$$i(t,n)=\frac{qSM\,(t_n,n)}{\tau_{tr}}M\,(t_{n-1}-\tau_{tr}=t_n=0,n-1)\exp[-(\frac{1}{\tau}+\frac{1}{\tau_{Dn}})t_n] \quad (4.28)$$

and using expressions of cascade multiplication $M(t_n,n)$, Eq. (4.24). Here, $qS=eR$ is the charge carried by the initially (at x, t=0) injected R pairs, $t=t_n+\Sigma_{p=0}^{n-1}p\,\tau_{tr}$ is the running time. The pure bipolar drift regime can be held by varied instantaneous values of coefficients α and β of the impact ionization dependent on acting field and instantaneous location of drifting charges. Diffusion within a narrow domain of the injected carrier pairs is included using the time dependent solutions of diffusion problem in a finite thickness region [115, 151]. Ambipolar diffusion is there characterized by the decay time $\tau_{Dn}=1/D\zeta_n^2$ with spatial frequency ζ_n of the main decay mode ascribed to a spatial width δ of the injected domain and including its broadening during each t_n of multiplication cascade.

Using assumptions i)-iv) and dynamic model based on Shockley-Ramo's theorem [26, 27], the simplified simulation algorithm for emulation of impact ionization attributed to the first generation carrier pairs can be made employing equal free mean paths λ_{ii}, attributed to the impact ionization, at the end of which quantity of pairs is doubled with $m=<M(x)>|_{\lambda ii}$, leading to $\eta=d/\lambda_{ii}$ segments of double multiplication of pairs. Then, the transit time $\tau_{tr,\lambda ii}$ is estimated for each segment of double multiplication, including of Ramo's current dependence on carrier density and location of each segment within inter-electrode gap. The complete transit (with multiplication) time $\tau_{tr,\Sigma,e}$ is a sum $\tau_{tr,\Sigma,e}=\Sigma_{\lambda ii}\tau_{tr,\lambda ii,e}$ of transit times over drift segments for either electrons or holes. Competition of recombination (τ) and multiplication $m=M(t,n)$ in Eq.(4.24) is accounted for in modification of drift velocity Eq.(4.25) within each segment by a sum of quantities $(-\tau_{tr,\lambda ii}/\tau)+M(\tau_{tr,\lambda ii},1)\geq 1$. Additionally, dependence of acting field on the amount of drifting charge ($eR\eta_e<M(x)>|_{\lambda ii}$) with approach of x (or $(w-x)$) to electrode is included, according to dynamic model [171], - in other words, shortening of τ_{Mq} (e.g., in Eq.(4.25)) with increase of the amount of drifting charge is taken into account. Simultaneously,

scattering leads to the three-dimensional drift regime, which makes the increased τ_{TOF} (in Eq. (4.25)), where τ_{TOF} is dependent on time and on drifting charge parameters. Multiplication process is additionally limited by the amount of the multiplied drifting charge: $eM(t,n) \leq Q_B = CU$, i.e. it cannot exceed the charge Q_B supplied by battery of voltage U to a device of capacitance C. For large multiplication, the increased charge $eM(t,n) \approx Q_B$ of free drifting carriers will screen (via electrostatic induction) the externally created charge Q_B on electrodes. Then, the current changes are determined by charge collected at electrodes, brought by diffusion.

Variations of current transients in capacitor type detector, simulated using the discussed assumptions and dynamic models with a set of parameters for GaN filled capacitor-type detector of inter-electrode gap w=5 μm, are illustrated in Figs. 4.4a and 4.4b. The results of simulations, illustrated in Fig.4.4, have been obtained neglecting the load resistance, i.e. keeping zero the load and battery internal resistances ($r_{L,B}$=0). The capacitor and PIN (with thin I-layer) type devices made of wide-gap materials show the similar characteristics when operating in particle detector regime [178, 179]. Therefore, illustration of evolution of detector transients in Fig. 4.4 enables ones to compare the capacitor as well as PIN detector characteristics and to clarify the main differences in using of the dynamic and steady-state approaches.

The simulated current evolution in time during the first generation segment of multiplied carriers is illustrated in Fig. 4.4a varying values of τ of recombination lifetime. For rather long recombination lifetime, increase of current is the fastest. The charge amount increases with time (due to multiplication caused by approach of drifting charge to electrode) and determines enhancement of acting field according to Coulomb law. These factors, - the nearly exponential increase of carrier quantity due to multiplication and of their velocity, lead to a sharp increase of current with time. However, for the large multiplication, the increased charge of free

drifting carriers will screen the externally created charge (due to applied external voltage) on electrodes. The current value limited by (screening) diffusion is sketched by a horizontal line in Fig. 4.4a.

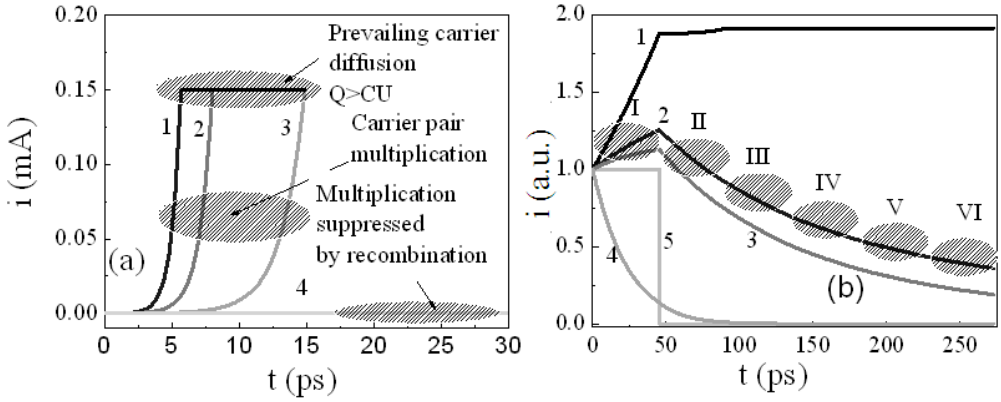

Fig. 4.4. Comparison of simulated current transients for capacitor-type detector of GaN. a- The initial component (of the first generation multiplied carrier pairs) of current transients, simulated using the described dynamic model with parameters: S= 10^{-4} cm^2, $<M(x,1)>_\lambda$=2, d=5 μm, U=40 V at initial amount of injected pairs R= 10 and varying recombination lifetime: 1 – τ=20 ps, 2 - 2 ps, 3 - 1 ps, 4 - 0.5 ps. b- Current transients including the higher generations of multiplied carrier pairs simulated using Eq.(9) with parameters D=2cm^2/s, δ=0.5μm, d=5μm, v=10^6cm/s, α=8000 cm^{-1} and carrier lifetimes 1- $\tau=\tau_D=\infty$, 2-τ=1 ns, 3-τ=300 ps; 4-20 ps, solid – (5) curve represents the current transient for pure bipolar drift without multiplication [A3].

The current transients consisting of a set of 6 generations (cascades denoted by dot circles and Roman ciphers) in multiplication sequence are illustrated in Fig. 4.4b. These transients have been simulated by using Eq. (4.28). The largest current appears for the first generation pairs due to the shortest transit time (where transit times of the counter-partners *e* and *h* coincide with carrier transit time without multiplication). Multiplied pairs of the second and the higher generations (Fig. 4.41b) run the longer paths than those for the first generation ones and consequently appear at the later instants of running time *t*. These pairs are responsible for the decreasing current variation in time after the current peak formed by the first generation pairs. The recombination consequently makes the most important influence by reducing current values within the rearward phase of a current pulse due to increase of transit time

($\exp(-t_2/\tau) > \exp(-t_3/\tau > ...$). Nevertheless, the cascade multiplication processes determine the rather long tail of current decrease (relaxation) after the peak of current caused by first generation carrier transit. Reduction of carrier recombination lifetime significantly shortens this relaxation component in current transient (Fig. 4.4b). The current pulse of the multiplied charge drift appears to be significantly longer than the charge drift current without multiplication, – Fig. 4.4b (for comparison shown this nearly square-shape pulse simulated at applied voltage slightly below the multiplication threshold). The multiplication regime enables ones to increase significantly the collected charge relative to that of the current integral (area of a square-shape pulse) determined by pure bipolar drift without multiplication. Moreover, the delayed relaxation of current pulse over multiplication processes of higher generations overwhelms the time scale from picoseconds to nanoseconds. It is a proper time range in usage of particle detectors in measurements with shaping time of several nanoseconds. The waveforms of current transients are additionally dependent on the measurement circuit elements, due to voltage drop $i(t)r_L$ within load resistor and current rise delay (τ_{rC}) within an external circuit [171].

4.4. Experimental profiling of sensor current transients

Particle pad-detectors (fabricated from n- type CZ (Czochralski grown) Si supplied by Okmetic Ltd) non-irradiated and irradiated with reactor neutrons to fluences in the range of Φ=10^{14}-3×10^{14} n/cm^2 were examined. The detectors with (p^+-n-n^+) diode structure had an active area of 5×5 mm^2 which was surrounded by 16 floating guard rings. The diode base material had dopant density of about 10^{12} cm^{-3} and base thickness 300 μm. A more detailed description of the detector structure is provided in Refs. [120,121]. To avoid boundary effects due to a field and current density distortions at narrow electrode and to keep $d << S^{1/2}$ for a detector with inter-electrode spacing d and a finite area S electrode, the diode was cut in halves, and a sawing boundary was polished by preparing a surface of the optical quality. For the evaluation of the cut boundary surface passivation by HF has been applied. The tentative

experiments were made by comparing current transients on non-cut and both passivated and non-passivated cut samples. In the last case, measurements were performed rapidly to fit a rather short duration of surface passivation with HF. However, steady-state surface leakage current seems to play the insignificant role within short duration transients, separated by a capacitor on the input of an oscilloscope.

The sample was mounted on a strip line (implemented by printing circuit board) with the polished boundary oriented perpendicularly to a focused scanning laser beam, Fig. 4.1. The strip-line with a mounted sample was connected to an external circuit using the high-frequency SMA sockets. Measurement circuit contains a diode connected in series with a reverse bias voltage source and a 10 Ω load resistor, Fig. 4.1a. An amplifier was employed for measurements of weak signals, when necessary. The measurement circuit time RC constant is 175 ps. The current transient pulse, generated by an excitation light pulse, is registered on a load resistor (and pre-amplified if necessary) by using closed input of the 1 GHz band, a real time oscilloscope TDS-5104. The calibration measurements of the strip line with sample showed the time resolution of 290 ps when using a 10 Ω load resistor while it was not better than 700 ps for a 50 Ω load. These calibration tests were performed by analyzing the rise to peak of the photo-voltage signal generated by a short laser pulse. The sample holder with circuit connectors was mounted on a step-actuator driven 3D stage. Boundary scans had been performed at room temperature by movements (with precision of 2.5 μm) of the sample relative to a pulsed (400 ps) laser beam (Fig. 4.1b).

The uncertainty concerning the laser beam propagation within bulk of the detector can appear if: i) the scanned volume can act as a waveguide; ii) an outspread of a sharply focused beam is possible; iii) a diffusive broadening of the injected carrier domain can be important if a dimension of any electrode is comparable with that of a beam. The strongly absorbed (in Si) light of 532 nm wavelength with a penetration depth of <2 μm was employed in order to avoid

these uncertainties, Fig. 4.1b. An excitation spot was either of ϕ=6 or 25 μm diameter at a waist of a focused Gaussian laser beam. The caustic of the distribution of focused Gaussian laser beam has been simulated using the WinLase software [180]. A profile of the focused laser beam has been examined experimentally by employing common techniques, e.g. Refs. [171, 181], in laser physics: both knife-edge and laser beam profiler (Coherent: Laser Cam-HR and Chameleon: CMLN-13521-CS), placed at the location of studied sample boundary. The surface density ($\leq 10^7$ cm^{-2}) of the light injected carriers has been evaluated by measurements of light energy per pulse and using calibration of the attenuator as well as a waist diameter of the laser beam. Really, the smallest surface density is limited by sensitivity of the measurement system with a suitable signal amplifier. The impact of surface passivation of the freshly prepared boundary has been estimated by comparison of the transients measured by using parallel (direction of the impinging excitation beam is the same as the applied electric field) and perpendicular orientations between the laser beam and electric field before and after cutting of a diode. The diffusive outspread (with carrier diffusion coefficient D~10 - 30 cm^2/s and the drift current pulse duration of τ_P~1–30 ns) is $\overline{V}=(2D\tau_P)^{1/2}$, which is in the range of 2.5 to 25 μm and is not larger than a laser beam spot dimension.

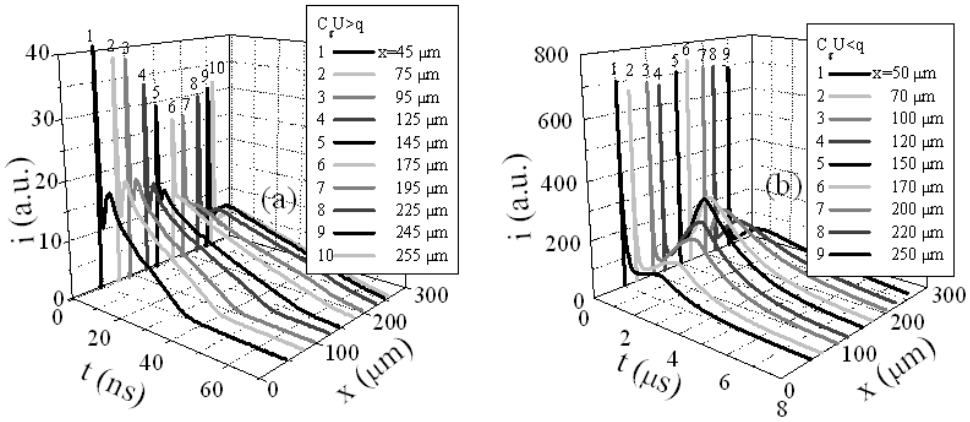

Fig.4.5. The ICDC transients measured in the non-irradiated Si pin diode (with 300 μm thick n-type conductivity base of ~10^{12} cm^{-3} dopant density) as a function of the injection location and for the rather small, - $q/q_C = q/C_gU \cong 10^{-3}$ for U=100 V applied voltage (a) and rather large, - $q/q_C \cong 10$, (b) density of the injected charge for U=11 V applied voltage [A9].

Variations of the injected charge domain drift current transients with $X_0=\psi_0 d$ for the small (top panel) and large (bottom panel) injected charge are illustrated in Fig. 4.5, as measured on the non-irradiated Si pin diode.

As can be deduced from Fig. 4.5(a), the profile of the initial current peak qualitatively agrees well with the simulated one in Fig. 4.3, for the small injected charge density. The initial peak indicates the bipolar drift phase. The rearward kink (in the current pulse), the smaller second peak implies the small charge drift regime where an increase of velocity with time within the monopolar drift phase is small and hided by velocity acquired during bipolar drift. Nevertheless, the shape of the current transient clearly shows the bipolar injection and drift phase proceeded by the monopolar drift. However, the experimentally obtained duration of the ICDC pulses is shortened with approach of the injection point to the mid of the inter-electrode spacing. This disagreement can be explained by the impact of lateral diffusion (with an enhanced surface recombination at cut boundary) within the surface plane of the injected domain due to narrow excitation spot $\nabla\sim\phi$. The impact of the lateral diffusion was not accounted for within the simulations of ICDC transients, shown in Fig. 4.3. For the sharp gradients of the $\nabla\sim\phi$, the characteristic diffusion times $\tau_D=1/D\eta^2_{m1}$ can become extremely short due to $\eta_{m1}\cong\pi m_1/\phi$, where $m_1\rightarrow\infty$. Then, the impact of the lateral diffusion is the most important for the injection locations close to a mid of the inter-electrode spacing.

For the large injected charge (in Fig. 4.5b), the diffusion within the inter-electrode spacing $d>>\phi$ appears to be the prevailing process. Then, the pulse duration of the diffusion governed process $\tau_D=1/D\eta^2_{m1}\cong d^2/D\pi^2$ reaches the microsecond range, instead of the drift governed ICDC pulses of a few nanoseconds. Consequently, the peak current values within the ICDC transients are obtained to be the largest ones for the injection locations nearby a half of d. This can be understood by the smallest impact of surface

recombination (field mediated extraction of carriers at electrodes) for $X_0 \cong d/2$. Additionally, the impact of the lateral diffusion should be the smallest. Such an increase of current peaks (initial and rearward) is really observed in Fig. 4.5b for the large bipolar domain injected at half-width (curve 5) of a base region.

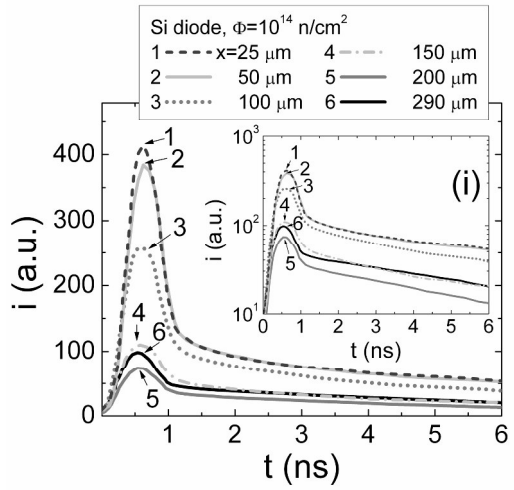

Fig. 4.6. The ICDC transients measured in the 10^{14} n/cm^2 neutron fluence irradiated Si pin diode as a function of the injection location for the small density ($q/q_C \cong 10^{-3}$) of the injected charge for U=100 V applied voltage. In the inset (i), these ICDC transients are re-plotted in the semi-log scale to highlight a bipolar drift stage and the trapping component [A9].

The small injected charge density ICDC transients, recorded on the 10^{14} n/cm^2 neutron fluence irradiated Si pin diode are illustrated in Fig. 4.6. The single peak ICDC transients can only be observed by profiling the injection location in these irradiated samples. It can be noticed that the measured ICDC pulse durations are considerably shortened (being of 1-2 ns relative to those of 10 ns – in Fig. 4.5a recorded in the same non-irradiated diode) within the bipolar drift and recombination phase. The current transient component dominated by carrier trapping can be highlighted in the semi-log scale (see inset of Fig. 4.6). It can be noticed that the duration (being of about 8 ns at exp(-1) level) of the carrier trapping component is nearly invariable. However, the more precise extraction of the carrier lifetime is rather complicated procedure, - both the charge decay and drift velocity changes (e.g. Eqs. 4.9 and 4.10) modify the current within its transient. This implies that the

carrier capture current component prevails in the current profiles obtained for the moderately irradiated diode.

The current peak profiles, recorded on different samples, are plotted in Fig. 4.7. The observed ICDC current peak profiles as well as pulse durations, obtained on the non-irradiated diode are shown in Fig. 4.7a. There the open circles denote the amplitude of the initial peak within ICDC transients, while the solid circles indicate the amplitudes of the rearward peak. The initial component indicates the bipolar drift phase with larger current relative to a monopolar drift component. The longer drift of holes (due to less their mobility) determines the larger distance of electron drift during a bipolar drift phase. Here, the profiles were scanned starting at junction, where holes are initially extracted. Also, this region is attributed to the stronger field in the diode base. Approaching to the rear electrode in profiling scans, the electrons are initially extracted, and their drift duration determines a time scale of the bipolar drift. However, this region is ascribed to the weaker field in diode base. The amplitudes of the rearward peak (solid circles) indicate current ascribed to the monopolar drift. It can be deduced form Fig.4.7a that a monopolar drift of electrons, for $x<150$ μm, determines the larger current than that caused by hole monopolar drift, for $x>150$ μm. The ratio of these amplitudes leads to $i_{peak}(x\sim40\ \mu m)/i_{peak}(x\sim260\ \mu m)\cong2.2$. This ratio would indicate the ratio of drift velocities of electrons (e) to that of holes (h). Assuming that velocity of the monopolar drift is proportional to the carrier mobility, $\mu_e/\mu_h\cong3$ for Si, and the obtained $i_{peak}(x\sim40\ \mu m)/ i_{peak}(x\sim260\ \mu m)\cong2.2$ shows difference in acting fields. Really, the monopolar drift of holes proceeds in the rising field. While for electrons, this field is descending. The pulse durations are also determined by different transit times of holes and electrons. It can be deduced from Fig. 4.7a, that the longer monopolar drift of holes (for $x>150$ μm) leads to the larger overall drift pulse duration.

The profiles of the initial ICDC current peak ascribed to the small injected charge, obtained for different applied reverse bias voltage, are presented in

Fig.4.7b. The increase of the current peak with applied voltage is ascribed to the increased electric field, which determines the bipolar drift current component even in the irradiated diodes. The current peak value clearly increases with applied voltage in the irradiated samples (Fig. 4.7b), while the drift pulse duration changes insignificantly (Fig. 4.6). This hints that the impact of the drift current component is rather small. Actually, carrier recombination in the initial quasi-neutral domain is important during separation of the charge sub-domains. Clearly, the density of the initially separated charges increases with voltage, while processes of the carrier recombination together with diffusion within ϕ dimensions are rather fast. Therefore, the mixed regime of the competing processes of drift, recombination and diffusion is represented in the measured current profiles on the irradiated samples.

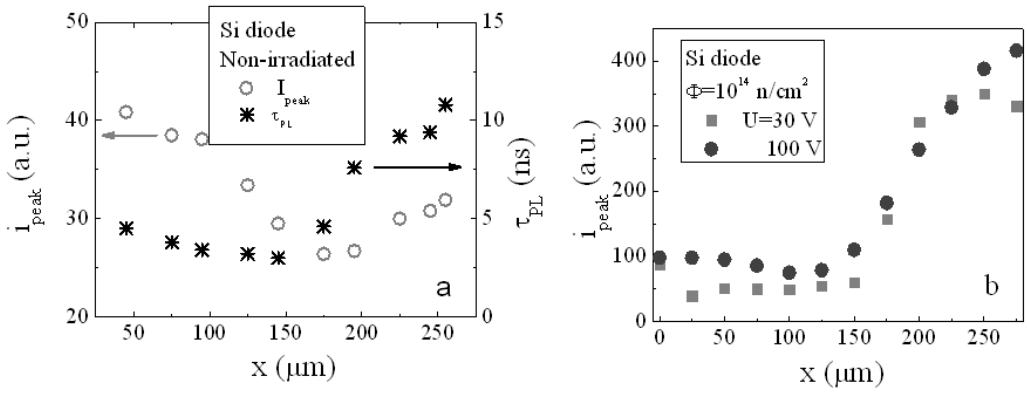

Fig. 4.7. The peak current value profiles measured in the non-radiated (a), and (b) in the 10^{14} n/cm^2 neutron fluence irradiated Si pin diode with 300 μm thick base for the small density of the injected charge ($q/q_C \cong 10^{-3}$) and for different applied bias voltage [A9].

The impact of avalanche processes can be estimated by a comparison of the peak current values, measured on the non-irradiated and the same irradiated samples. As mentioned, no impact of avalanche effects can reliably be separated within the ICDC profiles obtained on the non-irradiated diodes. The peak current values in the ICDC profiles, obtained on the irradiated same diodes, show even weaker current. This comparison allows inferring, that impact of the avalanche effects can be ignored, on the basis of principles of the description discussed above.

Summary for the chapter

The modelling of the current transients has been performed using assumptions, that: i) carrier drift within the heavily doped p^+ and n^+ layers of the pin structure can be ignored, as its duration is rather short and not resolvable within the RC time-gap of the measurement circuit; ii) nearly homogeneous domains (charged planes of a fixed area) of the injected charge are accepted in the case of the narrow excitation depth for the strongly absorbed light in the presented simulations; iii) the assumption of parallel-plate detector is valid for the drift of the small injected charge in the diode of rather large surface area S in comparison with excitation spot area $\pi\phi^2/4$ on the basis of Lagrange's (Fermat's) principle where it is kept that redistribution of charge on electrodes ($q_C=C_gU>q$) is fast enough to react on the induction caused changes of the charge density on electrode; iv) the drift velocity of injected domain is smaller than the velocity of the electric induction field (light) propagation. The principles of simulations are presented based on these assumptions.

Profiling of the injected charge drift current transients has been implemented by varying charge injection position within cross-sectional boundary of the non-irradiated and neutron irradiated Si pin diodes. The obtained profiles of the induction current density and duration of the injected charge drift pulses fit well the simulated current variations. It has been shown that the mixed regime of the competing processes of drift, recombination and diffusion appears in the measured current profiles on the irradiated samples. The impact of the avalanche effects within the range of applied voltages can be ignored based on the experimental profiling of current transients.

V. Formation technology of GaN sensors and operation characteristics

In this study, the structures of the capacitor and Schottky diode type detectors have been fabricated on GaN material grown by metal-organic chemical vapour deposition (MOCVD) and hydride vapour phase epitaxy (HVPE) using plasma etching and metal deposition technology. The material characteristics of the initial matter invoked into preparing of the tentative technology are described in Chapter III. The operational characteristics of these tentative detectors have been investigated by transient current profiling technique discussed in Chapter IV. The regimes of the perpendicular and parallel profiling have there been applied. The experimental current transients have been correlated with simulated current transients by employing the dynamic models discussed in Chapter IV, while additional modelling has been performed in order to include polarization effects. The experimental regimes of injection of the localized and bulk excess carrier packets have been examined in order to establish the surface charge formation and polarization effects. The screening effects have been observed and ascribed to surface charge and to dynamics of extraction of the injected excess carriers.

5.1. Materials and sensor types

The parameters of the invoked materials are listed in Table 5.1.

Table 5.1. Parameters of the samples fabricated as the capacitor (C_d) and Schottky diode (SD) devices.

GaN sample	Thickness (μm)	Technology	Device structure
u-GaN	24	MOCVD	C_d and SD
SI GaN:Fe	475	HVPE	C_d
HVPE-LD	400	HVPE	C_d
HVPE-HD	400	HVPE	C_d

The obtained results are important for prediction of the functionality of future GaN based sensors. The undoped (u-GaN) 24 μm thick epi-layers were

grown on sapphire substrates using MOCVD reactor (Aixtron 3x2FT close coupled showerhead system [182]). A thin (~0.2 μm) buffer layer of n^+-GaN was formed on sapphire substrate during the growth of MOCVD GaN epi-layer. This buffer layer serves as a layer of enhanced conductivity. Several semi-insulating (SI) GaN materials grown by HVPE technology and doped with compensating impurities were also employed for fabrication of sensors. The GaN:Fe sample of thickness 475 μm grown by HVPE technique was doped with Fe of concentration 2×10^{17} cm^{-3}. Also, HVPE SI GaN samples of thickness 400 μm contained growth defects and were doped with other compensating metallic impurities of low (HVPE-LD, $\sim 10^{16}$ cm^{-3}) and high (HVPE-HD, $\sim 10^{19}$ cm^{-3}) concentration. The capacitor (C_d) and Schottky diode (SD) type detectors have been fabricated using MOCVD GaN, whereas, capacitor sensors were made of HVPE SI GaN free-standing wafer fragments.

GaN material is a binary compound containing a crystalline structure with a lack of inversion centre symmetry [183-189]. Thus, a GaN crystal has a built-in polarization ascribed to the piezoelectric and the spontaneous polarization components. This polarization is directed along the crystal growth c-axis (0001), perpendicular to the epi-layer surface. For the bulk GaN material in equilibrium, this polarization field is screened by free carriers excited through band tilting and generated from the impurity and defect states. This built-in polarization can be a reason for appearance of a steady-state surface charge if the mobile carriers are extracted from the bulk by the applied external field. The built-in charge is able to screen the charge on the device electrodes induced by an external source. Free carriers trapped on the deep levels can also create a localized space charge within a region close to the electrode. Surface reconstruction during crystal relaxation may also be a reason [187] for suppressed crystal polarization effects in bulk material samples. Finally, extraction of a sub-system (of electrons or holes) of the light induced excess carrier pairs may be a reason for the formation of charged layers. These layers are depleted from one of the excess carrier sub-system, as injected electrons and holes move to opposite electrodes. There, the electrically neutral region

appears between the depleted layers, due to the sufficient density of excess carrier pairs to screen the external field (surface charge on electrodes). Thus, the acting electric field appears as a superposition of the fields. These fields are created by the surface charges on electrodes induced by an external battery, by the mobile charges of the light pulse injected carrier pairs, by the localized charge of carriers captured at deep traps and by the surface charge due to the built-in crystal polarization. The polarization effect may then occur due to the mentioned steady-state and dynamic components.

5.2. Formation steps and sensor structures

The capacitor type mesa structure detectors were fabricated using plasma etching to have the terrace structure where electrodes were deposited on the top and buffer layer surfaces. The In or Ag contacts were sputtered and sintered. The electric contacts were formed by using pressed Cu plate electrodes for bulk precursor samples using an Ag paste contact deposition on cleaned sample surface.

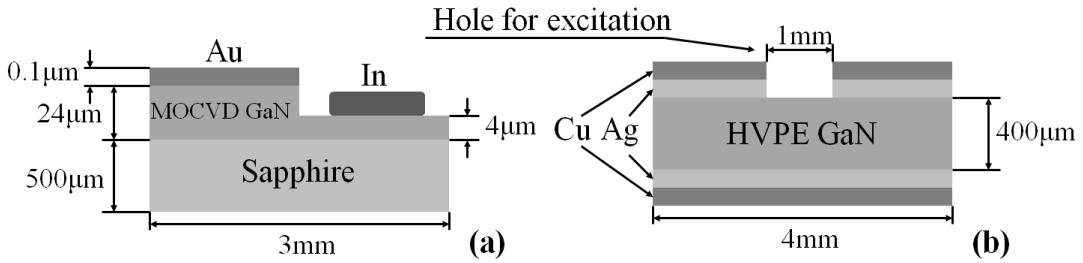

Fig. 5.1. Sketches of the Schottky diode (SD) (a) and the capacitor C_d (b) type sensors.

The Schottky barrier type mesa detectors were formed by deposition of the sintered In cathode at the bottom terrace, which was etched on GaN epi-layer, and the anode was fabricated by Au sputtering on top of the mesa structure. The schematic views of the fabricated structures are illustrated in Fig. 5.1. The top opening of ~1.5 mm width (significantly prevailing wafer thickness to suppress the role of lateral diffusion of the light injected carriers) was made for excitation of excess carriers.

In the MOCVD GaN meza structure devices and HVPE GaN wafer fragments employed for fabrication of the capacitor type and Schottky barrier sensors, the external field was always oriented along the c-axis. Therefore, for the range of rather low applied voltages, the polarization can suppress the external field, and the drift current signals disappear, similarly to formation of virtual gate and drain current collapse effects in field effect devices [189]. To reveal the dynamic and the steady-state components of the polarization, measurements of the relaxation of polarization were additionally performed.

The Schottky barrier diode formed on MOCVD GaN have been tested using BELIV, I-V and C-V measurements. These measurements indicated existence of blocking (in capacitor structure) electrodes and Schottky barrier in Au capped MOCVD GaN mesa structures. As an illustration for Schottky structures, the asymmetry of I-V (Fig. 5.2b) and capacitance decrease with enhancement of reverse voltage (Fig. 5.2c) in C-V characteristics clearly indicate the typical features of a diode. The inherent BELIV transient, illustrated in figure 5.2a, shows a barrier capacitance charging and generation current components. The latter (i_g) component appeared to be significantly modified by the additional continuous wave illumination. This result implies and supports existence of deep carrier traps.

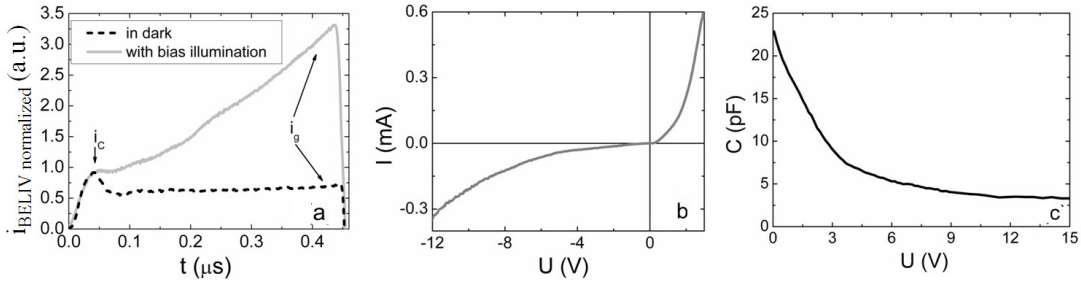

Fig. 5.2. BELIV transients recorded without and with additional illumination (a). I-V (b) and C-V (c) characteristics measured for MOCVD GaN Schottky diode, [A2].

5.3. Modelling of responses for sensors with polarization

The transients are as usual recorded within an external circuit. Therefore, the current is described as the surface charge density $\sigma(t)$ variations in time integrated over an area S of electrode. Under a switched-on external dc voltage U, a surface charge on electrodes is initially induced by an external battery. An additional surface charge on electrodes might be induced by spontaneous polarization of GaN material [183-185], filling the inter-electrode gap, as contacts are deposited within plane perpendicular to the c-axis of the MOCVD/HVPE grown crystal. The equilibrium/steady-state polarization charge can nevertheless be ignored in bulk GaN material as the surface relaxation and reconstruction [187-189] of the GaN sample and defects in the material lead to compensation of this polarization surface charge. The current transient is then formed by injection/recombination and drift/diffusion of a light pulse injected domain of excess carrier pairs (*e*-*h*) with surface charge density (q_e, q_h). It is assumed that the injected surface charge domains contain the same area as contacts and the electric fields created by these mobile domains are oriented in parallel to electric field induced by an external source. These surface charges (q_e, q_h) (due to their motion or changes in density) induce surface charges on electrodes (according to Shockley-Ramo's theorem). Under assumption of parallel oriented electric fields created by surface charges on electrodes and of injected domains, the moving surface charge domains create the varied electric fields $E_q(t, \psi)=q\,\psi(t)/\varepsilon\varepsilon_0$ dependent on instantaneous position X_q of the mobile domains within inter-electrode gap d, expressed through dimensionless parameter $\psi(t)=X_q(t)/d$. Thus, a superposition of the electric fields, created by the mobile surface charge domains and those of external battery, determines variation of surface charge on electrodes. The invariable voltage drop on sensor (as an integral of acting electric fields over inter-electrode gap d) is retained by changes in battery induced charge on electrodes. These charge variations (as a battery's feed-back to field variations within a sensor due to motion of the injected carriers) are namely registered as a current transient within an external circuit, i.e. on load resistor.

The generalized expression for the current dependence on time (t) ascribed to the bipolar (e-h) drift processes as well as to the instantaneous positions of sub-domains ($\psi_{e,h}(t)$), governed by the carrier drift and capture processes, reads as

$$i(t) = \frac{d\sigma}{dt} S = [-\frac{\partial q_e(t)}{\partial t}(1-\psi_e(t)) - q_h(t)\frac{d\psi_h(t)}{dt} - \frac{\partial q_h(t)}{\partial t}\psi_h(t) - q_h(t)\frac{\partial \psi_h(t)}{\partial t}]S \cdot \qquad (5.1)$$

This current contains the drift stages for the both polarity (bipolar) charges, which may be prolonged by the monopolar drift of holes (or electrons), if transit times (for e and h sub-domains) differ. In the case of hole monopolar drift, the current components are expressed as

$$i(t) = \begin{cases} i_1 = \dfrac{qS}{\tau_{tr,e}}[\psi_0 \exp(-\dfrac{t}{\tau_{tr,e}}) + (1-\psi_0)], \quad \text{for} \quad 0 \le t \le \tau_{tr,e} = \tau_{bC}; \\ i_2 = \dfrac{q_h S}{\tau_{Mq,h}} \exp(\dfrac{t}{\tau_{Mq,h}})[\dfrac{v_{0,\Sigma bip}}{d}\tau_{Mq,h} + \dfrac{\tau_{Mq,h}}{\tau_{TOF,h}} - 1], \quad \text{for} \quad 0 \le t \le \tau_{tr,h} \equiv \tau_{tr,h,mon} \end{cases} \cdot \qquad (5.2)$$

Here τ_{tr}, $\tau_{Mq\ e,h,}$, $\tau_{TOF,e,h}$ denote the characteristic times of transit, of dielectric relaxation and of free flight, respectively. Other symbols represent: v_0 is the initial velocity of the monopolar charge drift, d is the inter-electrode gap width, ψ_0 and $\psi_{e,h}$ are the dimensionless locations of the initial injection and of the instantaneous positions of drifting packets, respectively. The analytical description of the current transients, at low applied voltages U and bulk injection of an electron-hole packet, is implemented by considering the instantaneous position $X_{e,h}(t)=\psi_{e,h}(t)d$ variations. There appears the characteristic depth $X_{e,h0}$ of depletion, which in the case of the electron extraction is represented as

$$X_{e0}(n_0, U) = \frac{d}{2}\left(1 - \sqrt{1 - \frac{\varepsilon\varepsilon_0 U}{en_0\left(d/2\right)^2}}\right) \approx \frac{d}{2}\left(\frac{\varepsilon\varepsilon_0 (U/2)}{en_0\left(d/2\right)^2}\right). \qquad (5.3)$$

The depletion layers close to the surface occur due to screening/balance of the battery supplied surface charge by the charge of excess carriers left after initial extraction of their counter-partners within the light injected domain. The current variation in time (t) during the initial stage of a pulse ($i_1(t)$), when injected carriers drift and the depletion layer $X_{e,h\,0}$ forms, is obtained as

$$i_1(t) = S\frac{d\sigma}{dt} = \frac{S}{X_e(t)}\left(\frac{\varepsilon\varepsilon_0 U}{X_e(t)} - en_0 X_e(t)\right)\frac{dX_e(t)}{dt}. \qquad (5.4)$$

Here, ε_0 and ε represent permittivity of vacuum and material, respectively, n_0 is the initial concentration of the injected carrier pairs. A width of depletion layers can be increased and a reduction of the current within the initial stage of transients can occur for a set of injection light pulses applied if accumulation of the non-extracted carriers takes place. This may be a reason for sensor polarization. The accumulated carriers then prevent further induction of charge from the battery. This leads to a collapse of current (i_1) in transients generated by the set of injection light pulses. The current (i_1) value can only be restored if these mobile accumulated carriers are extracted by reverse polarity of the battery or shunted by a resistor installed in parallel to a sensor. These (near surface) accumulated carriers determine the dynamic polarization effect. Certainly, the accumulated carriers can also be trapped to deep levels residing in the near surface region (for instance, due to dangling bonds, impurities, etc.). This forms a space charge region which also causes polarization of sensor. The latter polarization can be reduced after trapped carriers are thermally emitted to the continuum states and extracted by appropriate polarity of the external voltage (or under relaxation to equilibrium after external voltage source is switched off). Both dynamic components of sensor polarization determine the current reduction (within the transients generated by a set of injection pulses) and duration of sensor recovery (polarization relaxation). Sketches of formation of the depletion region, of the screening and polarization fields are illustrated in Fig. 5.3.

Using equation for the instantaneous drift velocities (dX_e/dt) of carriers under acting electric fields (expressed through the dimensionless instantaneous locations ($\psi(t)$) of drifting charges), the initial stage (for the time interval $0 \le t \le \tau_{tr}$) of the drift current pulse can be described as

$$i_1(t) = \frac{S\varepsilon\varepsilon_0}{\psi(t)d} U \frac{1}{2\tau_{Mn0}}\left[\frac{1}{\psi(t)} - \frac{\tau_{TOF}}{\tau_{Mn0}}\psi(t)\right] \times \left[1 + \psi(t) - \frac{\tau_{Mn0}}{\tau_{TOF}}\frac{1}{\psi(t)}\right]. \qquad (5.5)$$

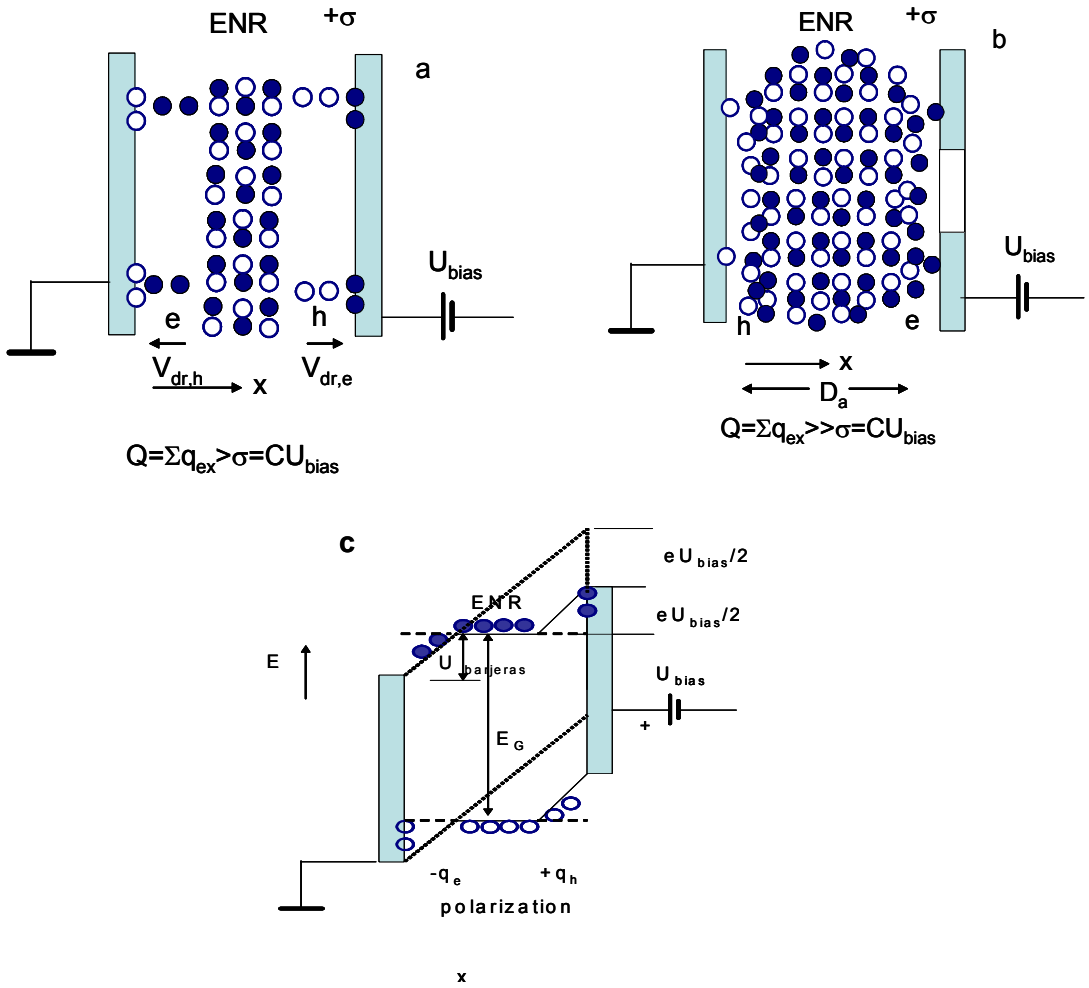

Fig. 5.3. Formation of the depletion regions (a), of the screening field by the photo-injected (into dielectric) bulk charge domain as well as its diffusive relaxation (b), and of the polarization field (c), respectively. ENR denotes the electrically neutral region.

An additional current component, ascribed to the carrier capture and recombination (with inherent lifetimes τ_C and τ_R, respectively), is introduced as

$$i(t)_{+\tau_R} = \begin{cases} i_1(t)\,|_{0\le t\le\tau_{tr}} - eS\dfrac{\partial(n_0 e^{-\frac{t}{\tau_R}})}{\partial t}X_e(t) \\ i_2(t-\tau_{tr})\,|_{t_2>\tau_{tr}} + eSd_{eff}n_0(t=0)e^{-\frac{t_2}{\tau_R}}\sum\limits_{k=0}^{\infty}\left(\dfrac{8}{\pi^2}(-1)^k\dfrac{\exp\left(\dfrac{4D_a\pi^2}{d_{eff}^2}(2k+1)^2 t_2\right)}{(2k+1)^2}\left[\dfrac{1}{\tau_{D,k}}-\dfrac{1}{\tau_R}\right]\right) \end{cases}. \quad (5.6)$$

Here, $d_{eff}=d-X_{e0}-X_{h0}$, $\tau_{D,k}=d_{eff}^2/[4\pi^2 D_a(2k+1)]$, and D_a is the coefficient of carrier ambipolar diffusion. More detail derivations of equations (5.1-5.6) can be found in Refs. [171, 190].

Solving the current equation for the external circuit with a characteristic relaxation time $R_{L,1||2}C_{d,SD}$, the actual current transient shape (slightly modified the idealized transient, described by equations (5.1)-(5.6), due to delays within external circuit) can be simulated and employed for the fitting of the experimental transients.

5.4. Experimental regimes for evaluation of sensor characteristics

The experimental setups exploited for recording of the pulsed current and the polarization relaxation transients are shown in Figs. 5.4a and 5.4b, respectively. More details on experimental arrangements can be found elsewhere [171, 190]. The sensor was mounted on a strip-line (to exclude frequency limitations for signal transfer within external circuit), implemented as a printed circuit board (PCB). The load resistance $R_{L,1||2}$=25 Ω (Fig. 5.4a) was employed for recording of the rather short pulses.

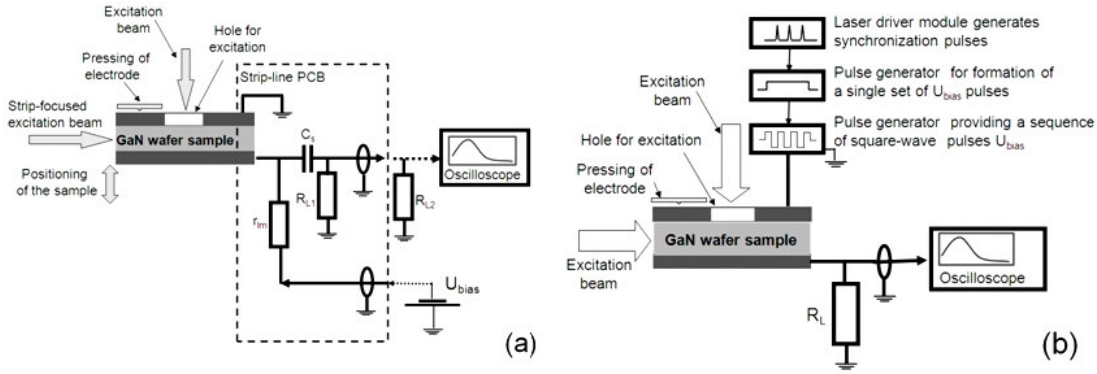

Fig. 5.4. Arrangement of measurement circuitries for the profiling of the carrier packet injection location (a) and for examination of the polarization relaxation (b), [A1].

The excess carrier packets (domains) were injected by using a beam of 354 or 532 nm light laser pulses of τ_L = 400 ps duration and 100 Hz repetition rate. A laser beam was focused by a cylindrical lens to a Δ~10 μm strip, which covered all the sample length to minimize the impact of the side diffusion of light injected carriers. Side diffusion of carriers complicates dynamics of electric field distribution, when one-dimensional approach becomes invalid. The sample depth over the inter-electrode gap was scanned by moving the

sample relative to this focused light strip. The energy of <1 μJ per laser pulse was kept, to implement the regime of small charge drift as well as to avoid screening effects attributed to the injected excess carriers, and the excitation intensity was lowered by neutral filters.

Different regimes of profiling of the sensor signals can be implemented by varying injection position and applied voltage to clarify the role of these components and to extract the parameters of carrier transport. Forming the local domains of drifting charges can be performed using carrier injection via pulsed excitation of the carriers through a cross-sectional boundary of a sensor structure when the excitation beam is oriented perpendicularly to the acting electric field. Profiling of sensor current pulses can also be implemented by varying voltage capable to extract a different amount of the injected carriers which are excited within the entire inter-electrode gap (where the excitation beam impinges in parallel to the acting electric field).

To reveal the dynamic and the steady-state components of the polarization, measurements of the relaxation of polarization were implemented. A recovery of the external field governed current transients can be observed by either switching-off the voltage or by the sudden changing of the voltage polarity. To highlight the changes of the charge induced by the external voltage source, transformations of the capacitor charging transient after each laser pulse (which injects carrier pairs and thus modifies the role/state of the surface polarization) have been examined. This has been implemented by using long pulses of applied voltage synchronized with the laser pulses which inject excess carrier pairs. Several pulse generators, sketched in Fig. 5.4b, were employed to arrange a single voltage pulse or a set of the square-wave bipolar voltage pulses. A set of laser light pulses generates the excess carriers in the bulk of GaN device during the voltage pulse. There, excitation was performed by impinging of a laser beam either through a hole made within electrode or by illuminating a cross-section of a device, as sketched in Fig. 5.4b. The set of the short charging current pulses of the amplitude decreasing in time is then recorded (as vertical lines) within a time scale of a voltage pulse and a set of

laser pulses running with 100 Hz repetition rate. These oscillograms directly represent a transient of suppression and recovery of the drift current values those were reduced due to accumulated polarization charge.

5.5. Operational characteristics sensors

5.5.1. Recombination and current transients in HVPE GaN sensors

The comprehensive study of the recombination characteristics, performed by combining analysis of the microwave probed photo-conductivity (MW-PC), recorded without external electric field, showed a wide variety in recombination and trapping lifetimes (as discussed in Chapter III). It has been inferred that the long-tail non-exponential behaviour of the MW-PC transients is caused by excess carrier trapping and de-trapping due to defects that are commonly introduced during MOCVD GaN crystal growth. The MW-PC transients obtained from MOCVD samples were well described by stretched-exponential relaxation (SER), indicating the significant disorder induced by defects in the material. Spectroscopy data for defects in GaN employed for fabrication of the device structures are discussed in Chapter III. Excess carrier relaxation transients in semi-insulating HVPE GaN samples showed considerably different time scales. It has been obtained that carrier recombination lifetime decreases with enhancement of concentration of the compensating metallic dopants, which also act as recombination centres.

Two experimental regimes have been implemented for profiling of current transients: i) by varying the applied voltage when an excitation beam is impinging in parallel to the external battery created electric field, and ii) by varying location of a focused injection beam within the inter-electrode gap when a laser beam is perpendicular to the electric field. The results of profiling of the injected charge current transients at room temperature for HVPE-HD sample with high concentration of dopants are illustrated in Fig. 5.5. The shape of the current transients is entirely related to the predominant process of recombination and drift-diffusion of the excess carriers, described in Section 5.4.

The primary current peak ($i_{peak}(t)=q/\tau_{tr,bip}$) in voltage profiled transients (Fig. 5.5a) is attributed to the bipolar drift of carriers, while a component of the decreasing current can be ascribed to the excess carrier trapping/recombination. The peak amplitudes of the current pulses dependent on detector biasing voltage show the impact of the polarization effect (Fig. 5.5b)). Formation of the near surface polarization charge by the injected excess carriers prevents charging of the device by the external battery of small voltage. These injected carriers may create a depletion layer either due mobile carriers (they cannot be extracted by a fixed polarity of external field) or they can be trapped by defect levels forming a localized space charge. This space charge may screen the electric field created by an external battery. Thus, the polarization charge suppresses the control of the injected carrier current by a small applied voltage (<50 V, Fig. 5.5b). This voltage profiling of current transients, ascribed to the injected bulk domains of carriers covering the entire inter-electrode gap, is suitable for evaluation of the role of the polarization effects. The current increase with voltage is clearly observed only for the voltages exceeding a threshold value of $U_{thr}\geq$100 V (Fig. 5.5b). Then, current increases almost linearly (Fig. 5.5b) with external voltage (>100 V) due to shortened transit time at elevated voltages for bipolar drift of injected carriers. However, this profiling regime does not allow to definitely evaluate the drift distance and transit time, as carrier trapping/recombination controls a rear stage of current transient when transit time is close to carrier lifetime.

The carrier mobility values have been estimated by analysis of the current dependence on locations of the electron-hole (e-h) domain injection (Figs. 5.5c and 5.5d), where drift distances of electrons and holes can be discriminated. For extraction of carrier mobility, the drift distance for the injected carrier sub-domain (which first reaches a contact) is evaluated from the injection position (within a profile of the peak current as a function of injection location) by including polarity of the applied voltage. Polarity of the applied voltage determines a sign (charge polarity) of the collected carriers, those arrive foremost to the electrode. The transit time for each injection position is

evaluated from the minimal current value within the respective (relative to each fixed position of injection) current transient (shown by dashed curve in Fig. 5.5d). The transit times coincide for both carrier sub-domains within a stage of bipolar drift in Fig. 5.5d, however, the drift distances are different due to different carrier mobilities. The drift time for bipolar motion stage is determined by transit of the sub-domain which foremost reaches the contact, as sub-domains synchronously move in opposite directions (Fig. 5.5d). The surface charge induced on electrodes by the latter sub-domain modifies electric field acting on another sub-domain. Therefore, current minimum is reached at the end of the bipolar drift, for a definite current transient (Fig. 5.5d). On the other hand, the minimum current at end of bipolar drift phase can be ascribed to the longest drift path and to a consequent transit time for a late sub-domain within the pure bipolar drift process (Fig. 5.5d). The flat or the ascending vertex of the second peak within current pulse indicates the monopolar drift. The transit time ascribed to the monopolar drift is then evaluated as the time interval between an instant where minimal current is reached and the end of the current pulse. The end of a drift pulse is estimated by the current bend within rear phase of a transient. The experimental transients are more complicated due to the delays, caused by external circuit elements, and the carrier capture/recombination processes. Durations of the current rise to peak and of relaxation may be distorted by the delays within the external circuit and carrier capture. Therefore, for the more precise extraction of drift parameters under mentioned complications, simulation of the current transients recorded for each injection location (Fig. 5.5d) is correlated with simulation of the entire profile (Fig. 5.5c) for the peak current dependence on injection position.

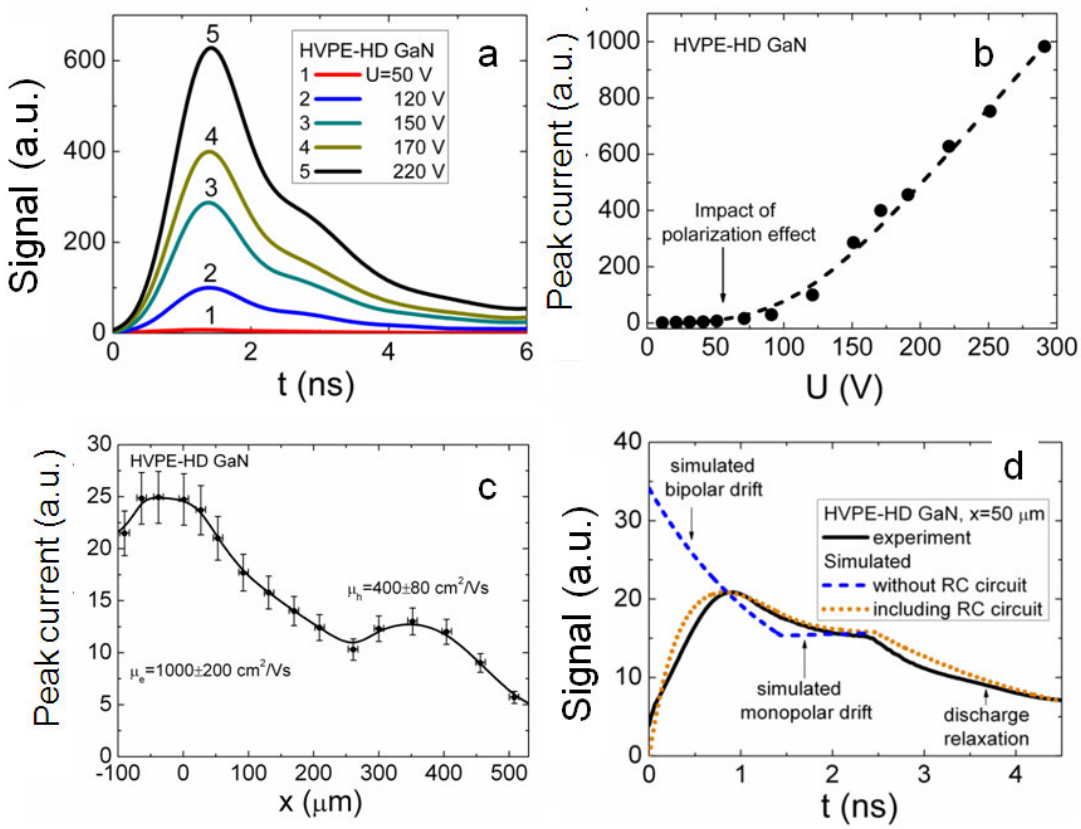

Fig. 5.5. Profiling of current transients by varied applied voltage (a) and peak amplitudes as a function of applied voltage (b). Profiling of current transients by varying location of the initial injection of e-h domain in HVPE GaN (c). In figure (d): the solid curve represents the transient as recorded within cross-sectional scan for carrier injection location at $x=X_0=50$ μm, the dashed curve represents the simulated current transient without including the impact of external circuit, the dotted curve simulated with including delays within external circuit, [A1].

The current minimum can also be observed within a profile of peak current dependent on injection position (Fig. 5.5c). This current minimum is obtained for the peculiar injection position when both sub-domains run the longest distances and reach electrodes synchronously. The square-wave shape transient would be an indication of such a pure bipolar drift regime, observable for a small density of drifting carriers when carrier capture can be excluded. The minimal current value is obtained (Fig. 5.5c), as current is a reciprocal function of the transit time. Indeed, a minimal current is observed (Fig. 5.5c) within a peak current profile, measured relative to injection position.

By combining analysis of transients and profiles (Figs. 5.5c and 5.5d), the drift distances and transit times are evaluated and employed for the extraction of carrier mobilities. To reproduce the transit time components, the recorded transients are fitted by simulated ones (as illustrated in Fig. 5.5d) for a transient recorded for a fixed injection location) using the dynamic model (sketched by equations (5.1)-(5.6)). Simulations are performed for every definite injection location using the parameters of the fixed external circuit (U, $C_{d,SD}$, S, R_L) as well as of the injection (n_0, X_0, Δ, D_a, τ_C, τ_L). The initial stage of the current pulse is always determined by the bipolar charge drift. While, the rear component of a transient is always ascribed to the monopolar charge drift, as follows from the dynamic models for small charge drift. The shape of the latter rear component depends on the applied voltage and on the density of the injected excess carrier pairs, resulting either the rising current shape or forming a rather flat vertex. The polarity of charge involved into the monopolar drift is unambiguously defined by the polarity of the external voltage. The polarity and value of the applied voltage, the transit times extracted from transients recorded for each injection location (by fitting experimental and simulated data) and the parameters of the external circuit (as RC_d) were taken into account for the evaluations of carrier mobility. Actually, the injection location and transit times for bipolar and monopolar drift were adjusted with relevant mobility of sub-domains in fitting of the experimental transients for evaluation of carrier mobilities. It is evident that the simulation procedure should be performed within a multi-dimensional space of the parameters of the external circuit, of the injection and of the material (μ_e, μ_h). Therefore, the most possible quantity of the independent relations (equations) is desirable. The peak current profile, illustrated in Figure 5.5(c), provides the additional relation to a set of transients, of the type illustrated in Fig. 5.5d. For the precise extraction of the material parameters (e.g., ascribed to carrier drift: μ_e, μ_h), a lot of iteration procedures should be performed by minimizing a functional in the non-linear least square method, serving as a measure for the best fitting between the experimental and simulated data.

Values of carrier mobility have been obtained to be: μ_e=1000±200 cm^2/Vs for electrons and μ_h=400±80 cm^2/Vs for holes, respectively. The statistical errors for extraction of mobility values are in the range of 20% relative to mean values. These errors are mainly arisen from uncertainties due to positioning of injection beam and simulation errors in evaluation of transit times. The obtained electron mobility value is in agreement with published data [191-194], while the estimated hole mobility value is twice less than those reported in [195], although it agrees with value reported in [196].

5.5.2. Current transients in GaN materials with short carrier lifetime

The discussed observations also imply the significant role of carrier capture in materials of short carrier lifetimes, in the range of a few ns, as revealed for HVPE GaN:Fe and MOCVD GaN materials. There the generation/carrier capture current components prevail.

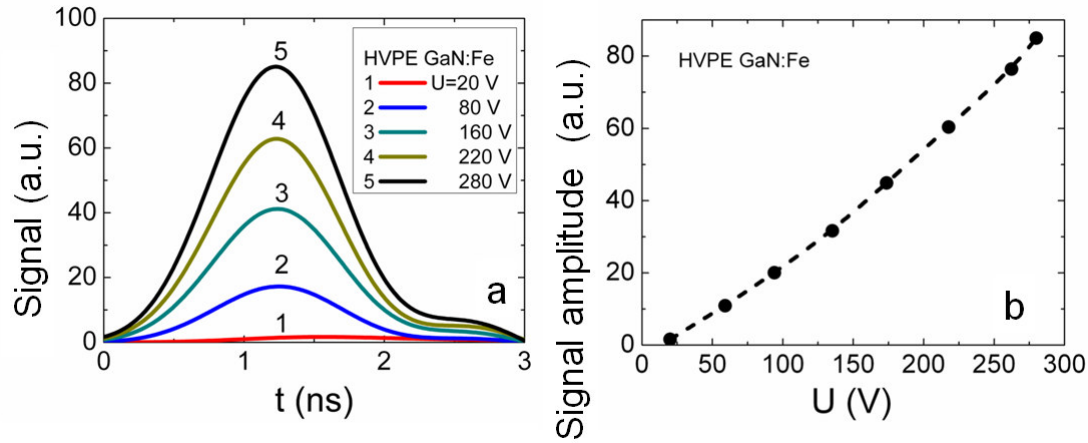

Fig. 5.6. Profiling of current transients (a) and of peak amplitudes (b) by applied voltage in HVPE GaN:Fe, [A1].

For the semi-insulating GaN material, i.e. HVPE GaN doped with Fe, current pulse duration (Fig. 5.6a) appeared to be shorter than that for the unintentionally doped HVPE GaN sample, as can be deduced by comparing transients in Figs 5.5a and 5.6a. Additionally, for the GaN:Fe sample where short recombination lifetimes (of τ_R~2 ns) were deduced from MW-PC transients, the peak current increases linearly (Fig. 5.6b) with applied voltage

over the entire range of the applied voltages, - i.e. the polarization effect is nearly negligible. In this GaN:Fe material, the current pulses, profiled by varying the injection location, appeared to be significantly shorter than those transients recorded (Fig. 5.5d) for the unintentionally doped HVPE GaN material with longer carrier lifetime.

The current increases with enhancement of voltage (Fig. 5.6a) due to the shortened transit time ascribed to the bipolar drift. However, due to rapid capture of carriers, this bipolar drift phase is not completed, - carriers disappear (through recombination) before one of the drifting sub-domains reaches a contact. Such a drift current is similar to that described by Hecht's model [197]. This can alternatively be understood as an increase of the excess carrier portion involved into drift. The registered sensor signal represents a sum of carrier drift and generation/capture current components (included within equation (5.6)). Thereby, current pulse duration is mainly determined by carrier lifetime. The transit time is indefinite in this case even for the bipolar drift phase, as neither drift distance nor drift duration can reliably be extracted from the recorded transients of 1-2 ns duration. In this case the current pulse duration is close to the carrier lifetime and the carrier drift parameters are hardly measurable in the materials with short carrier lifetime. The peak current increase with voltage is then obtained to be close to a linear function (Fig. 5.6b), as a rather small concentration of excess carriers is involved into drift. The carrier generation/capture current component then prevails in formation of the transient duration, while the current component attributed to the bipolar drift increases with voltage. The observed pulse durations are in good agreement with carrier recombination lifetimes measured by the MW-PC technique. The peak current (Fig. 5.6b) increases linearly with voltage due to predominant carrier drift processes. There, the peak current is an inverse function of a drift time which decreases almost linearly with enhancement of voltage.

5.5.3. Impact of polarization effects

To clarify the dynamics of polarization effect in MOCVD and HVPE GaN samples, the relaxation processes have been examined. Such a relaxation characteristic has been measured by controlling the changes of the amplitudes of the charging currents under action of a set of light pulses keeping either the invariable switched-on dc voltage or uni-polar voltage pulse (Fig. 5.7a) for the MOCVD GaN and by varying polarity of applied voltage for the HVPE GaN (Figs. 5.7b - 5.7d).

Formation of the surface charge and thus polarization of the MOCVD GaN structures seems to be caused by carrier capture into deep levels and formation of the localized space charge within near–surface regions, as discussed in Section 5.3. The characteristic relaxation time of the order of hundred milliseconds (Fig. 5.7a) represents duration of a balance between carrier capture to deep traps and thermal emission of trapped carriers in formation of a depletion layer of localized space charge capable to screen the external field. The relaxation transients of polarization appeared to be dependent on a series resistance for the MOCVD GaN capacitor type and Schottky diode structures. The series resistance in MOCVD devices appears due to inappropriate quality of contacts deposited on mesa structure. The series resistance leads to an increased offset within the initial component of relaxation curve in Fig. 5.7a.

For the HVPE GaN capacitor type sensors, the relaxation curve shape and duration depends on the doping level of the material (Figs. 5.7b- 5.7d). The initial offset for the relaxation curves (Figs. 5.7b and 5.7c) is rather small in highly doped GaN:Fe and HD GaN material sensors due to short carrier capture time. The duration of polarization charge creation during formation of depletion layers correlates well with carrier lifetimes when comparing transients in Figs. 5.7b (for GaN:Fe) and 5.7c (for HD GaN), where carrier lifetimes of $\tau_R \leq 2$ ns in GaN:Fe and $\tau_R \sim 20$ ns in HVPE-HD GaN, respectively, were measured by MW-PC. Thus, manifestation of the material polarization depends on bulk concentration of dopants and of excess carriers those are able to create polarization charge which screens the external field.

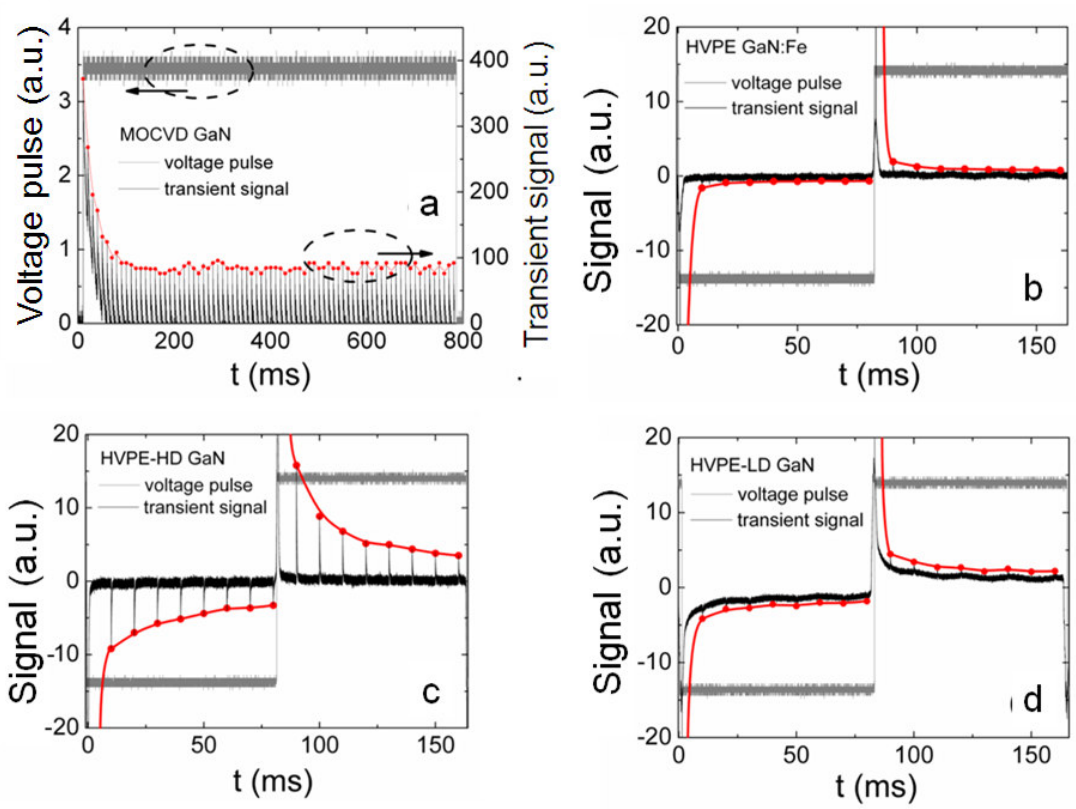

Fig. 5.7. Relaxation of peak current values under a set of injection light pulses in MOCVD GaN Schottky structure (a) and in HVPE GaN capacitor type sensors structures (sample of compensated GaN:Fe (b), and GaN samples HVPE-HD (c) as well as HVPE-LD (d)) due to polarization effect. Dashed ellipses indicate the groups of data points (curves) those are related with coordinate axis denoted by arrows, [A1].

Additionally, two relaxation components, fast and slow, can be clearly discriminated for the polarization process within curves of Fig. 5.7c. The characteristic times of the order of tens and hundreds of milliseconds ascribed to the slow component correlate with the time scale of thermal generation lifetimes attributed to deep levels. Consequently, variations of the sensor signals (Figs. 5.5a - 5.5d) determined by the injection of the excess carrier pairs and applied voltage are also sensitive to the time scale of formation/suppression of polarization.

The recorded peak amplitudes of the charging current pulses also depend on doping of the HVPE GaN material (Figs. 5.7c - 5.7d). This observation can be explained by different density of impurities and crystalline defects those modify the material ability either to accumulate the trapped carriers, by

forming surface charge, or to modify the built-in polarization. The density of defects also modifies the rate of the excess carrier decay. As a consequence, the polarization effect exhibits the steady-state (slow) and dynamic (fast) components for the HVPE GaN sensors. The charge collection efficiency realized at low voltages for injection of the bulk excess carrier domain, covering the entire inter-electrode gap, can be considerably limited due to the screening of the external electric field by a surface charge (polarization field) in such structures. The excess carriers residing nearby the electrodes can only be collected during formation of the depletion layers at low voltages. The excess carrier pairs deep in the bulk aggregate an electrically neutral region which separates the depleted layers at electrodes.

Summary for chapter

The GaN based capacitor and Schottky diode type detectors have been fabricated. Two regimes have been implemented for profiling of current transients in these devices: i) by varying the applied voltage when an excitation beam is parallel to the electric field, and ii) by varying location of a focused injection beam within the inter-electrode gap when a laser beam is perpendicular to the electric field. The carrier capture and drift components as well as polarization effect have been revealed in different GaN samples. It has been shown that the role of the polarization effect decreases with enhancement of the applied voltage. The drift component can be well discriminated by varying a location of a focused injection beam within the inter-electrode gap when the local e-h domains are injected. Profiling of the carrier injection location allows separating of the bipolar and monopolar drift components. The drift distance for drift of each sub-domain and their transit times can then be discriminated and evaluated. Using the parameters of the drift paths and of the transit times, carrier mobility has been extracted. Carrier mobility values attributed to the HVPE GaN material have been estimated to be: μ_e= 1000 ± 200 cm^2/Vs and μ_h= 400 ± 80 cm^2/Vs for electrons and holes, respectively. Relaxation of the peak current values due to polarization effect has been

examined using a set of the excitation pulses. For the HVPE GaN capacitor type sensors, the relaxation curve shape and its duration depends on doping of material. The polarization effect exhibits the components of the steady-state (slow) and of the dynamic (fast) polarization. The charge collection efficiency at low voltages can be considerably limited due to screening of the external electric field caused by the polarization effects in such structures under injection of the bulk charge within inter-electrode gap.

Technology of formation of the capacitor type sensors on diamond materials is nearly the same, as described in this chapter by discussing GaN sensors. Various metal contacts (implanted junctions, silver pasted, sintered In, pressed Cu) are there usually deposited on cleaned wafer sample surfaces. The main features of the capacitor type diamond sensors are similar in general view to those discussed on capacitor sensors made of GaN materials. Therefore, discussion of formation technology using diamond materials is skipped in this dissertation.

VI. Dosimetry sensors

The simple Si wafer fragments can serve as the irradiation dose sensors when fluence dependent variations of carrier recombination and thermal emission lifetimes are the parameters under control. It had been shown such a possibility in monitoring of fluences of the high energy protons and neutrons [198]. Then a lot of such Si wafer sensors can be sited over the large areas where rather intense radiations exist within accelerator facilities.

The more big challenge is to control irradiations by the extremely short-living sub-atomic particles, such as pions. There, a control of the pion beam profiles is also a considerable issue. Solution of this problem can be implemented by control of the lateral distribution of carrier lifetimes within Si wafer sensor areas of proper dimensions. In this study, the possibilities to monitor the pion beams and their irradiation fluences have been considered.

6.1. Prerequisites of Si dosimetry sensors

As mentioned above, the knowledge about the fluence dependent variations of carrier recombination and thermal emission lifetimes should be calibrated and ascribed to rather stable radiation defects, in order to apply Si wafer fragments for wide range dosimetry monitoring. The prerequisite investigations have been performed by using different quality Si materials and structures. Usage of rather cheap materials, for instance, solar-cell industry standard Si substrates, would facilitate production of large amounts of sensors for high fluence irradiations, relatively to alternative dosimetry sensors made of Al foils or even electronic grade devices.

The temperature dependent variations of carrier trapping lifetime is directly related to thermal emission parameters, ascribed to radiation defects. In order to have comparative information, set of the n-type Si of high resistivity (N_D~10^{12} cm^{-3}) wafer samples, grown by magnetic field applied Czochralski (MCZ) technique, and pin diodes [199] with active area of 5×5 mm^2 and thickness of 300 μm, made of the same material have been examined. These samples were irradiated with reactor neutrons of fluence Φ=10^{14} n/cm^2

(1 MeV n. eq.). Surfaces of wafer samples were passivated with thermal oxide. The isochronal anneals for 24 h were also performed by varying heat treatment temperature in the range of 80–380^{0}C for wafer samples. Wafer samples were employed for analysis of the carrier recombination and trapping/generation parameters, while diode samples were used to evaluate carrier generation characteristics on the same irradiated Si material.

Temperature dependent excess carrier decay transients have been examined by MW-PC technique [71] modified by usage of the special cryostat. This cryostat has been designed for the precise positioning of the optical fibre-tip and needle-tip MW probes in vacuum. Also, this cryostat is supplied with CaF window for the additional bias illumination of wide spectrum. Sample is commonly mounted on a cold finger cooled by liquid nitrogen. The liquid nitrogen flow is manipulated for the precise temperature stabilization. Temperature control is performed on a cold finger and the sample. Excess carriers are photo-generated by 500 ps laser pulses of 1062 nm wavelength. The excitation light is transferred into the cryostat by using optical fibre. The fibre-tip light spot excited area of the sample is probed by microwaves of 22 GHz using a needle-tip antenna. The microwave radiation is supplied to the needle-tip antenna by using the coaxial cables and vacuum proof connectors. The excess carrier decay transients are recorded by a 1 GHz digital Tektronix oscilloscope TDS-5104.

Carrier recombination and trapping lifetime values as a function of the inverse thermal energy (extracted from the measured MW-PC transients) are plotted in Fig. 6.1, as obtained for the samples irradiated with fluence of 10^{14} cm^{-2}. Carrier decay transients for the as-irradiated samples appear to be the single-exponential waveform. However, these transients are transformed into the two-componential decays after anneals. In Fig. 6.1, τ_R denotes the recombination lifetime described by the Shockley-Read-Hall (S-R-H) model with the well-known dependencies on the excess carrier density Δn and temperature T. The single-type carrier trapping is determined by the concentration M of such type defect and the effective density of states reduced

by the trap activation factor $N_M=N_{C,V}\exp(-\Delta E_M/kT)$. Spectroscopy by using the trapping effect is namely based on the temperature dependent changes of the carrier lifetime through variations of the effective density of states (i.e. $N_M(T)$). Hereby, trapping increases during the relaxation process of Δn, since the excess carrier density falls down, and the trapping effect appears as a long-tail component within the MW-PC transients at relatively low excitation intensity.

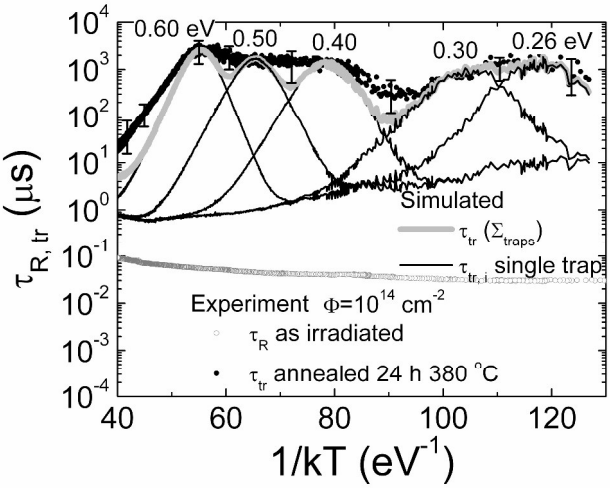

Fig. 6.1. Temperature dependent carrier recombination (τ_R) and trapping (τ_{tr}) lifetime variations in reactor neutrons as irradiated at fluences of $\Phi=10^{14}$ cm^{-2} and annealed Si wafer samples [A13].

Formation of the trapping lifetime peaks within temperature scan can serve as the indication of the transforms of radiation defects. There a system of the simultaneously acting carrier trapping (τ_{tr}) and recombination (τ_R) centres is considered. The deep traps act as the recombination defects, while carriers are temporary captured on levels which act as the trapping (generation current) centres. Competition of these centres determines the carrier decay flows and the current components in diode structures. Carrier lifetime (τ_R as well as τ_{tr}) dependences on the inverse thermal energy ($1/kT$) have been employed for evaluation of activation energy of the radiation defects. The trapping centres with the activation energy values of E_{tr1}=0.60±0.03, E_{tr2}=0.50±0.02, E_{tr3}=0.40±0.02, E_{tr4}=0.30±0.02, and E_{tr5}=0.26±0.02 eV should be employed to fit the experimental trapping lifetime changes within temperature scan for the

diode irradiated with neutron fluence of Φ=10^{14} cm^{-2} and annealed at 380^0C. Here, a pedestal of the simulated peaks is the variation of the measured recombination lifetime. In Fig. 6.1, the symbols represent the experimental changes of carrier lifetime values, while the simulated trapping lifetime peaks attributed to a definite level with characteristic activation energy are shown by lines. There, the grey curve represents the simulated sum over all the acting trapping centres. The overlap of the trapping ascribed peaks in the lifetime temperature scans (τ_{tr}-*1/kT*) can be noticed in Fig. 6.1. De-convolution of the τ_{tr}-*1/kT* bands enabled us to distinguish the centres with activation energy values of E_{tr1}=0.60±0.03, E_{tr2}=0.50±0.02 as well as E_{tr4}=0.30±0.02 eV, ascribed in literature to the radiation clusters [4] and E_{tr3}=0.40±0.02 as well as E_{tr5}=0.26±0.02 eV [3, 6] are commonly attributed to the single- and double-charged di-vacancy ($V_2^{-/0}$, $V_2^{=/-}$), respectively. It can be deduced by comparing the extracted deep level activation energy values that the di-vacancies appear as the most efficient carrier trapping centres, which determine the generation current in diode. Additionally, the thermal treatment activates a rich spectrum of traps. In the as irradiated material, the cluster defects are the dominant recombination centres, while these defects can act as the single-type carrier capture levels with large cross-sections under anneal induced defect transforms.

These traps have been confirmed by DLTS spectroscopy in the same materials [A14]. There neutron fluence dependent variation of the radiation defect spectra in MCZ Si pad detectors has been examined by combining the C-DLTS and O-I-DLTS regimes. The TDD, V-O and V_2 ascribed peaks have been observed within C-DLTS spectra measured in diodes irradiated with fluence of 10^{12} n/cm^2. Up to six O-I-DLTS peaks have been resolved within the temperature scan spectra measured in the range of 20- 300 K. These DLTS peaks have been ascribed to the TDD, V-O, V_2 and multi-vacancy complexes. The radiation induced vacancy attributed defects such as V-O, V_2 and clusters have been identified, density of which increases with irradiation fluence in the

range of 10^{12}–10^{14} cm^{-2}, while this density saturates for the collected neutron fluence of more than 10^{14} cm^{-2}. These traps appeared to be rather stable, while their density increases with irradiation fluence as illustrated in Fig. 6.2.

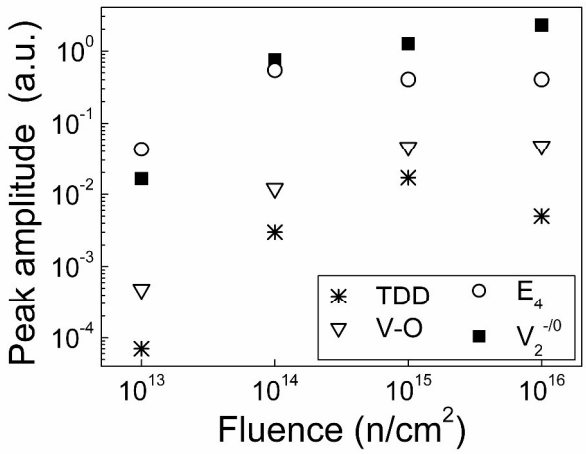

Fig. 6.2. The dependence of the amplitude of the O-I-DLTS spectral peaks on neutron irradiation fluence obtained for MCZ Si detectors, [A14].

The tentative industry solar cells, made employing of the copper technology, were examined [A11]. A solar cell contains the 180 μm thick p-Si base boron doped region. The n^+-p junction with an emitter thickness of 0.3 μm was formed by phosphor diffusion. The textured anti-reflection and the 150 nm thick Si_3N_4 surface passivation layers were formed. The silicide layers of Ni_2Si of thickness of 0.1 μm were also deposited. The electrodes were formed depositing by chemical means the Ni and Cu layers of 250 nm and 20 μm thickness, respectively.

The solar cell fragments of 4×4 mm^2 were cut for the C-DLTS measurements, as the commercial DLTS instruments enable compensation of the steady-state barrier capacitance of values less than 3 nF. It has been found within the DLTS measurements that the nickel-copper electrodes are insufficiently proof for the temperature cycling in the range of 50-300 K. Therefore, several samples were made using the 100 nm thick gold electrodes deposited by a magnetron sputtering, after the copper electrode had been removed. Then, the DLTS and BELIV techniques were combined to reveal the dominant thermal emission centres [A11].

The traps with activation energy values of E_B=0.045±0.001 eV, E_{Ni}=0.12±0.02 eV and $E_{Cu\text{-}2}$=0.23±0.02 eV have been resolved in solar cell fragments containing Ni/Cu electrodes. These traps can be assigned to B dopants with E_B =0.045±0.001 eV, and to the nickel impurities with E_{Ni}=0.12±0.02 eV. The trap with activation energy of $E_{Cu\text{-}2}$=0.23±0.02 eV can be ascribed to copper impurities. This latter activation energy value might also be inherent to Ni, as referenced in literature [158]. However, the value of the capture cross-section, attributed to Cu, is considerably larger. Therefore, the trap with activation energy of $E_{Cu\text{-}2}$=0.23±0.02 eV is assigned to the copper impurities in this consideration.

In samples made of solar cell fragment containing Au top electrode, the Ni ascribed traps with E_{Ni}=0.12±0.02 eV and the Cu attributed ones with activation energy of $E_{Cu\text{-}2}$ =0.23±0.02 eV have been resolved, as well. This indicates that Ni and Cu impurities were incorporated during the primary formation of electrodes on solar cells. The Cu impurities seem to form several deep levels with thermal activation energy values of $E_{Cu\text{-}2}$=0.23±0.02 eV, as determined from BELIV and C-DLTS temperature scans, and $E_{Cu\text{-}1}$=0.41±0.02 eV, as extracted from C-DLTS spectroscopy data. The performed spectroscopy clearly show the possibility to discriminate technological and radiation defects by comparing thermal emission spectra (DLTS) and carrier trapping lifetime (BELIV).

6.2. Dosimetry instrumentation based on carrier lifetime measurements

To cover wide range of fluences, the instrument VUTEG-5-AIDA had been designed and fabricated for dosimetry of collected fluence by MW-PCT technique (Fig. 6.3), which contains a dark measurement cabinet, wherein a steady-state bias illumination source is installed. A wafer fragment sensor under investigation, being placed within transparent plastic (polythene) bag, is mounted on positioning stage and brought into area of intersection of 500 ps pulsed IR (1062 nm) laser beam and of slit microwave antenna. The instrument

also contains modules for adjustments of measurement regime by varying pulsed IR light intensity using neutral optical filters, by MW bridge varied coupling between sample and slit antenna and by changing intensity of bias illumination. Transients are recorded by a 1 GHz band digital oscilloscope and data processing is performed by personal computer. Averaging of about 10^2 - 10^3 transients enabled us to significantly reduce an impact of noises.

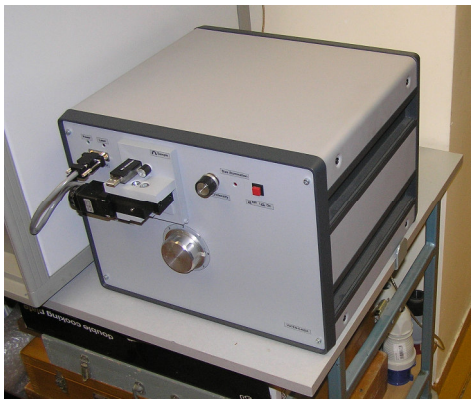

Fig. 6.3. A general view of the instrument VUTEG-5-AIDA.

Recombination parameters are rapidly extracted by using software for data processing, installed within the instrument VUTEG-5-AIDA. VUTEG-5-AIDA instrument also contains the temperature control and lateral mapping modules.

6.3. Dosimetry of pion irradiations

The latter study has been addressed to analysis of carrier lifetime changes in pion irradiated sensors made of different type Si material and to search of transforms of radiation defects under anneals in comparison with reactor neutron and high energy proton irradiation. Another task was to profile irradiation homogeneity by “pion beam” by using VUTEG-5-AIDA instrument installed at CERN.

Description of samples exploited and of parameters of the pion irradiations is presented in Table 6.1.

Table 6.1. Samples, parameters of pion irradiations and anneal regimes

SET#	Sample ID	Req. Fluence (n/cm^2)	Detector size (mm × mm)	Achieved flu. (n/cm^2)	Error (+/-%)
1907	AIDA 2012-Cz-n and Fz-n	1e11	10×10	1.34e11	7
1908	AIDA 2012-Cz-n and Fz-n	3e11	10×10	2.74e11	7
1909	AIDA 2012-Cz-n and Fz-n	1e12	10×10	7.68e11	7
1910	AIDA 2012-Cz-n and Fz-n	3e12	10×10	2.41e12	7
1911	AIDA 2012-Cz-n and Fz-n	1e13	10×10	1.07e13	7
1912	AIDA 2012-Cz-n and Fz-n	3e13	10×10	3.70e13	7
1913	AIDA 2012-Cz-n and Fz-n	1e14	10×10	1e14	7
1914	AIDA 2012-Cz-n and Fz-n	3e14	10×10	1.71e14	7
1915	AIDA 2012-Cz-n and Fz-n	1e15	10×10	4.26e14	7
1916	AIDA 2012-Cz-n and Fz-n	3e15	10×10	5.12e14	7

The rather inhomogeneous „pion beam“ irradiation profiles have been revealed by scanning the lateral distribution of carrier lifetimes in 1 cm^2 area sensors made of Si wafer fragments, as illustrated in Fig. 6.4. This implies a widely-outspread pion beam. The radiation defects introduced by pions are thermally stable showing a low migration velocity (in the range of rather small temperatures). The defect distribution profiles retain their shape over all the range of fluences and anneal temperatures applied.

It has been found the most important result that absolute values of carrier recombination lifetime in different type Si materials and irradiated with various type penetrative hadrons (neutrons, protons, pions) fit the same calibration curve, shown in Fig. 6.5.

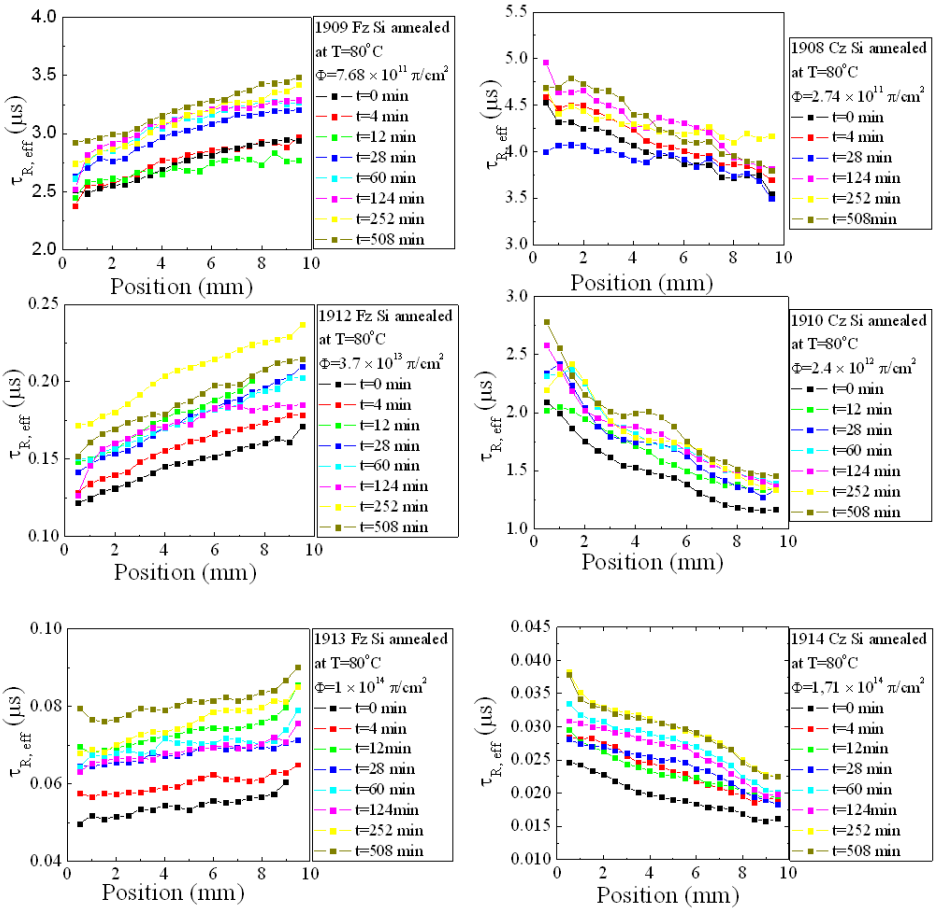

Fig. 6.4. Profiles of carrier recombination lifetime distribution along a single direction within n-Si wafer sensors (in the middle of its leg) irradiated with different pion fluences and isothermally (at 80^0C) annealed with various exposure times, [P1].

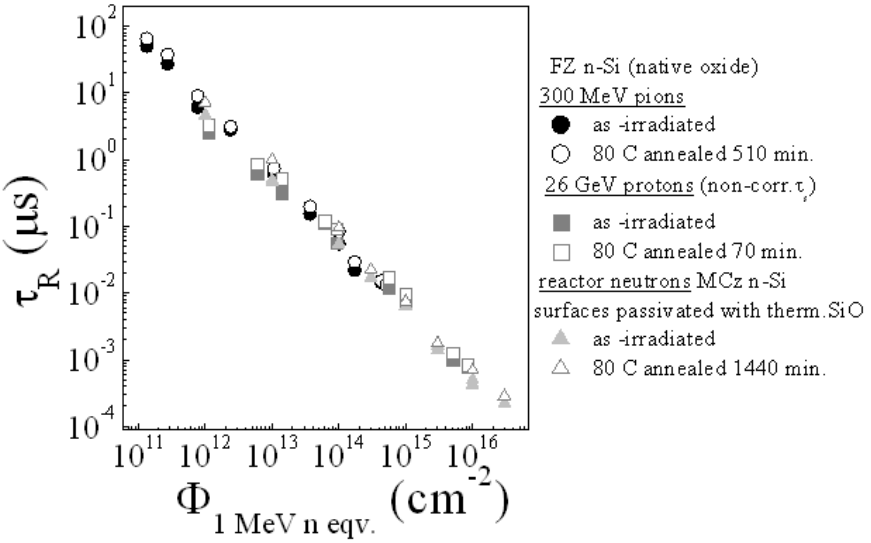

Fig. 6.5. Carrier recombination lifetime as a function of fluence for various type hadron irradiations when fluence is related to 1 MeV neutron equivalent damage, [P1].

The obtained calibration curve (Fig. 6.5) is nearly insensitive to thermal environment. Thus, the rather simple Si sensors are suitable for dosimetry of elevated hadron irradiation fluences (which is a serious issue using other dosimetry techniques).

The performed study, that different Si wafer fragments of relevant area and of proper material quality are promising sensors for fast dosimetry monitoring over the large areas where rather intense radiations exist within accelerator facilities. A single and simple test of fluence collected by a Si sensor can be performed during 1 min. including procedure of sensor mounting for measurements by VUTEG-5-AIDA instrument.

Summary for the chapter

The VUTEG-5-AIDA dosimeter for monitoring of the large fluence irradiations within facilities of hadron accelerators and spallators has been approved for monitoring of pion irradiation dosimetry. This instrument has been installed at CERN and approved for the monitoring of the accelerator environments and particle beams. It has been found the most important result that absolute values of carrier recombination lifetime in different type Si materials and irradiated with various type penetrative hadrons (neutrons, protons, pions) fit the same calibration curve. The obtained calibration curve for dosimetry using carrier recombination lifetime measurements is nearly insensitive to thermal environment. Thus, the rather simple Si sensors are suitable for dosimetry of elevated hadron irradiation fluences. Si wafer fragment sensors of relevant area and of proper material quality are promising devices for fast dosimetry monitoring over the large areas where rather intense radiations exist within accelerator facilities.

Conclusions

1. The parameters of native and radiation induced defects extracted by combining several spectroscopy techniques provide the comprehensive characterization of materials necessary in pre-selection procedure for design and fabrication of fast sensors made of wide-bandgap materials.
2. The dynamic models for description of sensor responses in different type detectors have been derived and approved for sensor signal profiling using the discretely varied external voltage and carrier injection position.
3. The dynamic models of carrier pair multiplication have been derived which are suitable for prediction of regimes in design of single active-layer sensors with internal gain.
4. The GaN based capacitor and Schottky diode type detectors have been fabricated. The polarization effects have been revealed in sensors made of different GaN materials. It has been shown that the role of the polarization effect decreases with enhancement of the applied voltage.
5. For the HVPE GaN capacitor-type sensors, the relaxation curve shape and its duration depends on doping of material. The polarization effect exhibits the components of the steady-state (slow) and of the dynamic (fast) polarization.
6. The charge collection efficiency at low voltages is considerably limited due to screening of the external electric field caused by the polarization effects in such structures under injection of the bulk charge within inter-electrode gap.
7. The drift current component within GaN sensor response can be well discriminated by varying a location of a focused injection beam within the inter-electrode gap when the local e-h domains are injected. The drift distance for drift of each sub-domain and their transit times can then be discriminated and evaluated. Using the parameters of the drift paths and of the transit times, carrier mobility has been reliably discriminated and evaluated. Carrier mobility values attributed to the HVPE GaN material have been estimated to be: μ_e= 1000±200 cm^2/Vs and μ_h= 400±80 cm^2/Vs for electrons and holes, respectively.

8. Comparison of the luminescence spectra induced by a proton beam and by a laser pulse in MOCVD grown GaN layers, enabled us to evaluate the efficiency of excess carrier generation by $\kappa_P = \langle n_P \rangle / N_P \cong 1.3 \times 10^7$ cm^{-3} per 1.6 MeV proton and carrier pair generation within layer depth by $\kappa_P A_{pr} = 40$ $\mu m^{-1} p^{-1}$. These parameters indicate that GaN layers can be an efficient material for detection of protons by combining both the electrical measurements, using a proper thickness of detector layer with $\kappa_P A_{pr} = 40$ $\mu m^{-1} p^{-1}$ to reach the resolvable charge collection signal, and scintillation detection, using rather fast photo-sensors, capable to integrate the PI-YG-L signals with $\kappa_P \cong 10^7$ cm^{-3}p^{-1}.

9. It has been obtained that the inevitable degradation of the material appears for proton irradiation fluences above 10^{14} cm^{-2} with radiation defect introduction rate $K_P \cong 0.6$ cm^{-1}. The calibrated reduction of the intensity of PI-L in the range of green-yellow luminescence can also be exploited for dosimetry of the hadron irradiations in rather wide range of fluences.

10. The rather inhomogeneous „pion beam“ irradiation profiles have been revealed by scanning the lateral distribution of carrier lifetimes in 1 cm^2 area sensors made of Si wafer fragments. This implies a widely-outspread pion beam. The radiation defects introduced by pions are thermally stable showing a low migration velocity.

11. The absolute values of carrier recombination lifetime in different type Si materials and irradiated with various type penetrative hadrons (neutrons, protons, pions) fit the same calibration curve.

References

[1] http://www.wsts.org/PRESS/Recent-News-Release.

[2] http://rd50.web.cern.ch/rd50/.

[3] H. Spieler, *Semiconductor detector systems* (Oxford University Press, New York, 2005).

[4] M. Huhtinen, *Simulation of non-ionising energy loss and defect formation in silicon*, Nucl. Instrum. Meth. A **491** (2002) 194-215.

[5] S. Assouak, E. Forton, G. Gregoire, *Irradiations of CMS silicon sensors with fast neutrons*, Nucl. Instrum. Meth. A **514**, 156 (2003).

[6] G. Lutz, *Semiconductor radiation detectors – device physics* (Springer, Heidelberg, 2007).

[7] E. Gaubas, T. Čeponis, J. Vaitkus, *Impact of generation current on evaluation of the depletion width in heavily irradiated Si detector*s, J. Appl. Phys. **110** (2011) 033719.

[8] E. Gaubas, T. Ceponis, A. Jasiunas, A. Uleckas, J. Vaitkus, E. Cortina, and O. Militaru, *Correlated evolution of barrier capacitance charging, generation and drift currents and of carrier lifetime in Si structures during 25 MeV neutrons irradiation*, Appl. Phys. Lett. **101** (2012) 232104:1-232104:3.

[9] K. Takahashi, A. Yoshikawa, A. Sandlu, *Wide bandgap semiconductors: Fundamental properties and Modern Photonic and electronic devices* (Springer-Verlag, Berlin, Heidelberg, 2007).

[10] H. Lim, S. Park, H. Cheong, H.-M. Choi, Y. C. Kim, *Discrimination between natural and HPHT-treated type IIa diamonds using photoluminescence spectroscopy*, Diam. Relat. Mater. **19** (2010) 1254–1258.

[11] Y. V. Babich, B. N. Feigelson, A. P. Yelisseyev, *Nitrogen aggregation and linear growth rate in HPHT synthetic diamonds*, Diam. Relat. Mater. **13** (2004) 1802–1806.

[12] F. De Weerdt, A. T. Collins, *Determination of the C defect concentration in HPHT annealed type IaA diamonds from UV–VIS absorption spectra*, Diam. Relat. Mater. **17** (2008) 171–173.

[13] R. Kucharski, M. Zajac, A. Puchalski, T. Sochacki, M. Bockowski, J. L. Weyher, M. Iwinska, J. Serafinczuk, R. Kudrawiec, Z. Siemiątkowski, *Ammonothermal growth of GaN crystals on HVPE-GaN seeds prepared with the use of ammonothermal substrates*, J. Cryst. Growth **427** (2015) 1–6.

[14] J. Smalc-Koziorowska, G. Kamler, B. Lucznik, I. Grzegory, *Structural defects in GaN crystals grown by HVPE on needle-shaped GaN seeds obtained under high N_2 pressure*, J. Cryst. Growth **311** (2009) 1407–1410.

[15] N. M. Shmidt, V. V. Sirotkin, A. A. Sitnikova, O. A. Soltanovich, R. V. Zolotareva, E. B. Yakimov, *SEM/EBIC investigations of extended defect system in GaN epilayers*, Phys. Status Solidi C **2** (2005) 1797.

[16] I. Pintile, E. Fretwust, G. Lindstom, *Cluster related hole traps with enhanced-field-emission the source for long term annealing in hadron irradiated Si diodes*, Appl. Phys. Lett. **92** (2008) 024101.

[17] G. Kramberger, V. Cindro, I. Mandic, M. Mikuz, M. Zavrtanik, *Effective trapping time of electrons and holes in different silicon materials irradiated with neutrons, protons and pions*, Nucl. Instrum. Meth. A **481** (2002) 297–305.

[18] V. Eremin, N. Strokan, E. Verbitskaya, Z. Li, *Development of transient current and charge techniques for the measurement of effective net concentration of ionized charges (N_{eff}) in the space charge region of p-n junction detectors.* Nucl. Instrum. Meth. A **372** (1996) 388–398.
[19] M. Pomorski, *Electronic properties of single crystal CVD diamond and its suitability for particle detection in hadron physics experiments*, (Dissertation, Frankfurt, 2008).
[20] M. Martini, G. Ottaviani, *Ramo's theorem and the energy balance equations in evaluating the current pulse from semiconductor etectors*, Nucl. Instrum. Meth. A **67** (1969) 177–178.
[21] G. Cavalleri, E. Gatti, G. Fabri, S. Svelto, *Extension of Ramo's theorem as applied to induced charge in semiconductor detectors*. Nucl. Instrum. Meth. A **92** (1971) 137–140.
[22] P. de Visschere, *The validity of Ramo's theorem*, Solid State Electron. **33 (**1990) 455–459.
[23] E. Gatti, A. Geraci, *Considerations about Ramo's theorem extension to conductor media with variable dielectric constant,* Nucl. Instrum. Meth. A **525** (2004) 623–625.
[24] I. V. Kotov, *Currents induced by charges moving in semiconductor*. Nucl. Instrum. Meth. A **539** (2005) 267–267.
[25] L. A. Hamel, M. Julien, *Generalized demonstration of Ramo's theorem with space charge and polarization effects*, Nucl. Instrum. Meth. A **597 (**2008) 207–211.
[26] S. Ramo, *Currents induced by electron motion*, Associate member, I.R.E. **73** (1939).
[27] W. Shockley, *Currents to conductors induced by a moving point charge*, J. Appl. Phys. **9** (1938) 635.
[28] J. G. Korvink, A. Greiner, *Semiconductors for micro and nanotechnology — an introduction for engineers* (WILEY-VCH Verlag GmbH: Weinheim, Germany, 2002).
[29] K. Blotekjer, *Transport equations for electrons in two-valley semiconductors,* IEEE T. Electron. Dev. **ED-17** (1970) 38–47.
[30] M. Zaitsev, *Optical properties of diamond: a data handbook* (Springer-Verlag, Berlin, 2001).
[31] M. Nakhostin, *Charged particle response of transmission diamond detectors*, Nucl. Instrum. Meth. A **703** (2013) 199–203.
[32] T. Tanaka, Junichi. H. Kaneko, Y. Kasugai, M. Katagiri, H. Takeuchi, T. Nishitani, T. Iida, *Radiation tolerance of type IIa synthetic diamond detector for 14 MeV neutrons*, Diam. Relat. Mater. **14** (2005) 2031 – 2034.
[33] S. Koizumi, K. Watanabe, M. Hasegawa, H. Kanda, *Ultraviolet emission from a diamond pn junction*, Science **292** (2001) 1899–1901.
[34] D. R. Kania, M. I. Landstrass, M. A. Plano, L. S. Pan, S. Han, *Diamond radiation detectors*, Diam. Relat. Mater. **2** (1993) 1012–1019.
[35] J. Schein, K. M. Campbell, R. R. Prasad, R. Binder, M. Krishnan, *Radiation hard diamond laser beam profiler with subnanosecond temporal resolution*, Rev. Sci. Instrum. **73** (2002) 18.

[36] F. de Weerdt, J. van Royen, *Defects in coloured natural diamonds*, Diam. Relat. Mater. **10** (2001) 474 -479.
[37] D. Fisher, *Brown diamonds and high pressure high temperature treatment*, Lithos **112S** (2009) 619–624.
[38] S. Eaton-Magana, R. Lu, *Phosphorescence in type IIb diamonds*, Diam. Relat. Mater. **20** (2011) 983–989.
[39] R. C. Burns, V. Cvetkovic, C. N. Dodge, D. J. F. Evans, M.-L. T. Rooney, P. M. Spear, C. M. Welbourn, *Growth-sector dependence of optical features in large syntheticdiamonds*, J. Cryst. Growth **104** (1990) 257–279.
[40] A. F. Khokhryakov, Y. N. Palyanov, I. N. Kupriyanov, Y. M. Borzdov, A. G. Sokol, *Effect of nitrogen impurity on the dislocation structure of large HPHT synthetic diamond crystals*, J. Cryst. Growth **386** (2014) 162–167.
[41] H. Kanda, *Nonuniform distributions of colour and luminescence of diamond single crystals*, New Diam. Front. C. Tec. **17** (2007) 105–116.
[42] D. Fisher, S. C. Lawson, *The effect of nickel and cobalt on the aggregation of nitrogen in diamond*, Diam.Relat. Mater. **7** (1998) 299-304.
[43] B. V. Yavkin, G. V. Mamin, S. B. Orlinskii, *High-frequency pulsed ENDOR spectroscopy of the NV^- centre in the commercial HPHT diamond*, J. Magn. Reson. **262** (2016) 15–19.
[44] A. Yelisseyev, Y. Babich, V. Nadolinny, D. Fisher, B. Feigelson, *Spectroscopic study of HPHT synthetic diamonds, as grown at 1500^oC*, Diam. Relat. Mater. **11** (2002) 22–37.
[45] I. N. Kupriyanov, V. A. Gusev, Yu. M. Borzdov, A. A. Kalinin, Yu. N. Pal'yanov, *Photoluminescence study of annealed nickel- and nitrogen-containing synthetic diamond*, Diam. Relat. Mater. **8** (1999) 1301–1309.
[46] S. J. Pearton, *GaN and related materials II* (Gordon and Breach Science Publishers, Amsterdam, 2000).
[47] A. Ionascut-Nedelcescu, C. Carlone, A. Houdayer, H. J. von Bardeleben, J.-L. Cantin, and S. Raymond, *Radiation hardness of gallium nitride*, IEEE T. Nucl. Sci. **49** (2002) 6.
[48] P. Sellin, J. Vaitkus, *New materials for radiation hard semiconductor detectors*, Nucl. Instrum. Meth. A **557** (2006) 479.
[49] J. Neugebauer, C. G. Van de Walle, *Atomic geometry and electronic structure of native defects in GaN*, Phys. Rev. B **50** (1994) 8067.
[50] N. Kuwano, Y. Ryu, M. Mitsuhara, C.-H. Lin, S. Uchiyama, T. Maruyama, Y. Suzuki, S. Naritsuka, *Behavior of defects in a-plane GaN films grown by low-angle-incidence microchannel epitaxy (LAIMCE)*, J. Cryst. Growth **401** (2014) 409–413.
[51] S. C. Jain, M. Willander, J. Narayan, R. Van Overstraeten, *III–nitrides: Growth, characterization, and properties*, J. Appl. Phys. **87** (2000) 3.
[52] M. A. Reshchikov, H. Morkoç, *Luminescence properties of defects in GaN*, J. Appl. Phys. **97** (2005) 061301.
[53] H. Tang, Z.Q. Fang, S. Rolfe, J.A. Bardwell, S. Raymon, *Growth kinetics and electronic properties of unintentionally doped semi-insulating GaN on SiC and high-resistivity GaN on sapphire grown by ammonia molecular-beam epitaxy*, J. Appl. Phys. **107** (2010) 103701.

[54] P. Thurian et al., *Photoluminescence of Fe complexes in GaN*, in proceedings of 1996 MRS Fall Meeting, Boston, Massachusetts, U.S.A., 2–6 Dec 1996, Mater. Res. Soc. Symp. Proc. 449.
[55] P. Hacke, T. Detchprohm, K. Hiramatsu, N. Sawaki, K. Tadatomo, K. Miyake, *Analysis of deep levels in n-type GaN by transient capacitance methods*, J. Appl. Phys. **76** (1994) 304.
[56] E. B. Yakimov, *Electron-beam-induced-current study of defects in GaN; experiments and simulation*, J. Phys.: Condens. Matter **14** (2002) 13069–13077.
[57] K. Yamamoto, H. Ishikawa, T. Egawa, T. Jimbo, M. Umeno, *EBIC observation of n-GaN grown on sapphire substrates by MOCVD*, J. Cryst. Growth **189/190** (1998) 575—579.
[58] M. A. Moram and M. E. Vickers, X-*ray diffraction of III-nitrides*, Rep. Prog. Phys. **72** (2009) 036502 (40pp).
[59] Z.-Q. Fang, D. C. Look, X.-L. Wang, J. Han, F. A. Khan, I. Adesida, *Plasma-etching-enhanced deep centers in n-GaN grown by metalorganic chemical-vapor deposition*, Appl. Phys. Lett. **10** (2003) 82.
[60] P. Muret, A. Philippe, E. Monroy, E. Munoz, B. Beaumont, F. Omnes, P. Gibart, *Deep levels in MOCVD n-type hexagonal gallium nitride studied by high resolution deep level transient spectroscop*, Mater. Sci. Eng. B **82** (2001) 91–98.
[61] A. Y. Polyakov, I.-H. Lee, *Deep traps in GaN-based structures as affecting the performance of GaN devices*, Mater. Sci. Eng. B **94** (2015) 1–56.
[62] U. Honda, Y. Yamada, Y. Tokuda, and K. Shiojima, *Deep levels in n-GaN doped with carbon studied by deep level and minority carrier transient spectroscopies*, Jpn. J. Appl. Phys. **51** (2012) 04DF04.
[63] W. Götz, N. M. Johnson, H. Amano, I. Akasaki, *Deep level defects in n-type GaN*, Appl. Phys. Lett. **65** (1994) 463.
[64] M. A. Reshchikov, D. O. Demchenko, A. Usikov, H. Helava, Yu. Makarov, *Carbon defects as sources of the green and yellow luminescence bands in undoped GaN*, Phys. Rev. B **90** (2014) 235203.
[65] H. Kim, K. M. Song, *Investigation of blue luminescence in Mg-doped nonpolar a-plane GaN*, J. Lumin. **145** (2014) 631–634.
[66] S. Suresh, S. Lourdudoss, G. Landgren, K. Baskar, *Studies on the effect of ammonia flow rate induced defects in gallium nitride grown by MOCVD*, J. Cryst. Growth **312** (2010) 3151–3155.
[67] G. Miceli, A. Pasquarello, *Energetics of native point defects in GaN: A density-functional study*, Microelectron. Eng. **147** (2015) 51–54.
[68] P. Bhattachary, R. Fornari and H. Kamimura eds., *Comprehensive semiconductor science and technology*, *Volume III: Materials, preparation and properties* (Elsevier B.V., Oxford, 2011).
[69] T. Nishinga and P. Rudolph eds., *Handbook of crystal growth: Bulk crystal growth, Volume II, Part A* (second edition, Elsevier B.V., Oxford, 2015).
[70] S. M. Sze, K. K. Ng, *Physics of semiconductor devices* (John Wiley and Sons, Inc. Hoboken, New Jersey, 2007).

[71] E. Gaubas, *Transient absorption techniques for investigation of recombination properties in semiconductor materials*, Lith. J. Phys. **43** (2003) 145 – 165.
[72] A. Kaniava, A. L. P. Rotondaro, J. Vanhellemont, U. Menczigar, E. Gaubas, *Recombination activity of ironrelated complexes in silicon studied by temperature dependent carrier lifetime measurements,* Appl. Phys. Lett. **67** (1995) 3930 – 3932.
[73] J.S. Youa, J. Kang, D. Kimb, J. J. Pak, C. S. Kang, *Copper metallization for crystalline Si solar cells*, Sol. Ener. Mater. Sol. C. **79** (2003) 339–345.
[74] K. M. Chow, W. Y. Ng, L. K. Yeung, *Barrier properties of Ni, Pd and Pd-Fe for Cu diffusion*, Surf. Coat. Tech. **105** (1998) 56–64.
[75] C. Leu, D. P. Norton, L. McElwee-White and T. J. Anderson, *Ir/TaN as a bilayer diffusion barrier for advanced Cu interconnects*, Appl. Phys. Lett. **92** (2008) 111917.
[76] P. Blood, J. W. Orton, *The electrical characterization of semiconductors: majority carriers and electron* (States Academic Press Inc., San Diego, 1992).
[77] D. V. Lang, *Deep-level transient spectroscopy: a new method to characterize traps in semiconductors*, J. Appl. Phys. **45** (1974) 3023 – 3032.
[78] S. U. Pandey, P. Middelkamp, Z. Li, V. Eremin, *New experimental and analysis methods in I-DLTS*, Nucl. Instrum. Meth. A **426** (1999) 109—11.
[79] E. Gaubas, S. Jursenas, R. Tomasiunas, J. Vaitkus, A. Zukauskas, A. Blue, M. Rahman, K. M. Smith, *Characterization of as-grown and heavily irradiated GaN epitaxial structures by photoconductivity and photoluminescence*, Nucl. Instrum. Meth. A **546** (2005) 247.
[80] E. Gaubas, V. Kovalevskij, A. Kadys, M. Gaspariunas, J. Mickevicius, A.Jasiunas, V. Remeikis, A. Uleckas, A. Tekorius, J. Vaitkus, A.Velicka, *In situ* variations of recombination characteristics in MOCVD grown GaN epi-layers during 1.7 MeV protons irradiation, Nucl. Instrum. Meth. B **307** (2013) 370.
[81] E. Gaubas, K. Kazlauskas, R. Tomasiunas, J. Vaitkus, A. Zukauskas, *Radiation-defect-dependent photoconductivity transients and photoluminescence in semi-insulating GaN*, Appl. Phys. Lett. **84** (2004) 5258.
[82] A. Finzel, J.W. Gerlach, J. Lorbeer, F. Frost, B. Rauschenbach, *High-fluence hyperthermal ion irradiation of gallium nitride surfaces at elevated temperatures*, Appl. Surf. Sci. **317** (2014) 811–817.
[83] L. Neumann, J. W. Gerlach, B. Rauschenbach, *Initial stages of the ion-beam assisted epitaxial GaN film growth on 6H-SiC(0001)*, Thin Solid Films **520** (2012) 3936–3945.
[84] L. Q. Zhang, C. H. Zhang, X. J. Jia, J. Gou, Y. T. Yang, Y. Song, C. L. Xu, Y. C. Meng, J. Y. Li, Y. F. Jin, *Structures and optical properties of Kr^{23+} and Ne^{8+}-irradiated GaN epi-layers*, Nucl. Instrum. Meth. B **307** (2013) 60–64.
[85] K. Lorenz, J. G. Marques, N. Franco, E. Alves, M. Peres, M. R. Correia, T. Monteiro, *Defect studies on fast and thermal neutron irradiated GaN*, Nucl. Instrum. Meth. B **266** (2008) 2780–2783.

[86] J. G. Marques, K. Lorenz, N. Franco, E. Alves, *Defect production in neutron irradiated GaN*, Nucl. Instrum. Meth. B **249** (2006) 358–361.
[87] A. Y. Polyakov, A. S. Usikov, B. Theys, N. B. Smirnov, A. V. Govorkov, F. Jomard, N. M. Shmidt, W. V. Lundin, *Effects of proton implantation on electrical and recombination properties of n-GaN*, Solid State Electron. **44** (2000) 1971-1983.
[88] V. V. Emtsev, V. Yu. Davydov, V. V. Kozlovskii, G. A. Oganesyana, D. S. Poloskina, A. N. Smirnov, E. A. Tropp, Yu. G. Morozov, *Radiation-produced defects in n-GaN*, Physica B **401–402** (2007) 315–318.
[89] E. Gaubas, S. Jursenas, S. Miasojedovas, J. Vaitkus, A. Zukauskas, *Carrier and defect dynamics in photoexcited semi-insulating epitaxial GaN layers,* J. Appl. Phys. **96** (2004) 4326.
[90] A. Y. Polyakov, A. S. Usikov, B. Theys, N. B. Smirnov, A. V. Govorkov,F. Jomard, N. M. Shmidt, W. V. Lundin, *Effects of proton implantation on electrical and recombination properties of n-GaN*, Solid State Electron. **44** (2000) 1971.
[91] P. Pittet, G.-N. Lu, J.-M. Galvan, J.-M. Bluet, I. Anas, J.-Y. Giraud, J. Balosso, *PL characterization of GaN scintillator for radioluminescence-based dosimetry*, Opt. Mater. **31** (2009) 1421–1424.
[92] L. Ling, H. Yue, Z. XueFeng, Z. JinCheng, X. ShengRui, L. Zhi Yu, A. Shan, M. Fan Na, *Proton irradiation effects on HVPE GaN*, Sci. China Technol. Sci. **55** (2012) 2432.
[93] R. Blachnik, A. Muller, *The formation of Cu_2S from the elements: I. Copper used in form of powders*, Thermochim. Acta **361** (2000) 31.
[94] V. A. Smyntyna, V. A. Borschak, M. I. Kutalova, N. P. Zatovskaya, A. P. Balaban, *Sensor based on a non-ideal heterojunction to indicate X-ray images,* Semicond. Phys. Quant. Electron. Optoelectron. **7** (2004) 222.
[95] F. Nataren, D. Vassilevsky, S. Chandrasekhar, B. Bouchikhi, S.Martinuzzi, *$Cu_xS/Cd_{1-y}Zn_yS/CdS$ evaporated back-wall bifilm solar cell,* Thin Solid Films **90**, L49 (1982).
[96] G. She, X. Zhang, W. Shi, Y. Cai, N. Wang, P. Liu, D. Chen, *Template-free electrochemical synthesis of single-crystal CuTe nanoribbons*, J. Cryst. Growth **8** (2008) 1789.
[97] C. Nascu, I. Pop, V. Ionescu, E. Indrea, I. Bratu, *Spray pyrolysis deposition of CuS thin films*, Mater. Lett. **32**, 73(1997).
[98] J. Cardoso, O. Gomez-Daza, L. Ixtlilco, M. T. S. Nair, P. K. Nair, *Conductive copper sulfide thin films on polyimide foils,* Semicond. Sci. Tech. **16** (2001) 123.
[99] V. M. Garcia, P. K. Nair, M. T. S. Nair, *Copper selenide thin films by chemical bath deposition,* J. Cryst. Growth **203** (1999) 113.
[100] E. Gaubas, V. Borschak, I. Brytavskyi, T. Ceponis, D. Dobrovolskas, S. Jursenas, J. Kusakovskij, V. Smyntyna, G. Tamulaitis, A. Tekorius, *Nonradiative and radiative recombination in CdS polycrystalline structures,* Adv. Condens. Matter. Phys. **15** (2013) 917543.

[101] E. Gaubas, I. Brytavskyi, T. Ceponis, J. Kusakovskij, G. Tamulaitis, *Barriel capacitance characteristics of CdS-Cu_2S junction structures*, Thin Solid Films **531** (2013) 131.
[102] M. Rogalla, M. Battke, N. Duda, R. Geppert, R. Gappert, J. Ludwig, R. Irsigler, Th. Schmid, K. Runge, A. Saldner-Rembold, *Radiation damage due to pions and protons in SI-GaAs and their influence on the detector performance*, Nucl. Instrum. Meth. A **410** (1998) 41-45.
[103] G. Kramberger, V. Cindro, I. Dolenc, I. Mandic, M. Mikuz, M. Zavrtanik, *Comparison of pad detectors produced on different silicon materials after irradiation with neutrons, protons and pions*, Nucl. Instrum. Meth. A **612** (2010) 288–295.
[104] G. Lindstrom, I. Dolenc, E. Fretwurst, F. Honniger, G. Kramberger, M. Moll, E. Nossarzewska, I. Pintilie, R. Roder, *Epitaxial silicon detectors for particle tracking, – radiation tolerance at extreme hadron fluence*, Nucl. Instrum. Meth. A **568**, (2006) 66–71.
[105] I. Pintilie, L. Pintilie, M. Moll, E. Fretwurst and G. Lindstroem, *Thermally stimulated current method applied on diodes with high concentration of deep trapping levels*, Appl. Phs. Lett. **78** (2001) 550.
[106] Z. Li, *Systematic modelling and comparisons of capacitance and current-based microscopic defect analysis techniques for measurements of high-resistivity silicon detectors after irradiation*, Nucl. Instrum. Meth. A **403** (1998) 399–416.
[107] V. Eremin, N. Strokan, E. Verbitskaya, Z. Li, Nucl. *Development of transient current and charge techniques for the measurement of effective net concentration of ionized charges N_{eff} in the space charge region of p-n junction detectors*, Nucl. Instrum. Meth. A **372** (1996) 388.
[108] C. Leroy, P. Roy, G. Casse, M. Glaser, E. Grigoriev, F. Lemeilleur, *Study of charge transport in non-irradiated and irradiated silicon detectors*, Nucl. Instrum. Meth. A **426** (1999) 99-108.
[109] S. Uxa, R. Grill, and E. Belas, *Evaluation of the mobility-lifetime product in CdTe and CdZnTe detectors by the transient-current technique*, J. Appl. Phys. **114** (2013) 094511.
[110] S. Uxa, E. Belas, R. Grill, P. Praus and R. B. James, *Effect of contact preparation on the profile of the electric field in CdZnTe detectors*, J. Phys. D: Appl. Phys. **46** (2013) 395102.
[111] S. Uxa, E. Belas, R. Grill, *Determination of electric-field profile in CdTe and CdZnTe detectors using transient-current technique*, IEEE T. Nucl. Sci. **59** (2012) 5.
[112] Z. Li, *Generalization of the modeling and design considerations of concentric and spiral Si drift detectors*, Nucl. Instrum. Meth. A **730** (2013) 73.
[113] E. Verbitskaya, V. Eremin, A. Zabrodskii, Z. Li, P. Luukka, *Restriction on the gain in collected charge due to carrier avalanche multiplication in heavily irradiated Si strip detectors*, Nucl. Instrum. Meth. A **730** (2013) 66–72.
[114] E. Gaubas, J. Vaitkus, K. M. Smith, *Monitoring of carrier lifetime in GaAs substrate–epi-layer structures by space-resolved transient microwave absorption,* Nucl. Instrum. Meth. A **460** (2001) 35.

[115] E. Gaubas, J. Vaitkus, E. Simoen, C. Claeys, and J. Vanhellemont, *Excess carrier cross-sectional technique for determination of the surface recombination velocity*, Mat.. Sci. Semicon. Proc. **4** (2001) 125.
[116] E. Verbitskaya, G. Ruggiero, I. Eremin, I. Ilyashenko, A. Cavallini, A. Castaldini, G. Pellegrini, M. Lozano, S. Golubkov, N. Egorov, K. Konkov, T. Tuuva, *Electrical properties of the sensitive side in Si edgeless detectors*, Nucl. Instrum. Meth. A **604** (2009) 246–249.
[117] G. Kramberger, V. Cindro, I. Mandic, M. Mikuz, M. Milovanovic, M. Zavrtanik, K. Zagar, *Investigation of irradiated silicon detectors by edge-TCT*, IEEE Tractions on nuclear science, **57** (2010) 4.
[118] M. Milovanovic, V. Cindro, G. Kramberger, I. Mandic, M. Mikuza, M. Zavrtanik, *Effects of accelerated long term annealing in highly irradiated n+-p strip detector examined by Edge-TCT*, JINST **7** (2012) P06007.
[119] G. Stewart, R. Bates, C. Fleta, G. Kramberger, M. Lozano, M. Milovanovic, G. Pellegrini, *Analysis of edge and surface TCTs for irradiated 3D silicon strip detectors*, JINST **8** (2013) P03002.
[120] I. Mandic, V. Cindro, A. Gorisek, G. Kramberger, M. Mikuz, M. Milovanovic, M. Zavrtanik, T*CT measurements of irradiated strip detectors with a focused laser beam*, JINST **8**, P04016.
[121] K. Blotekjer, *Transport equations for electrons in two-valley semiconductors*, IEEE T. Electron. Dev **ED-17** (1970) 38.
[122] E. Gaubas, T. Ceponis, A. Jasiunas, E. Jelmakas, S. Jursenas, A. Kadys, T. Malinauskas, A. Tekorius, P. Vitta, *Study of carrier recombination transient characteristics in MOCVD grown GaN dependent on layer thickness,* AIP Adv. **3** (2013) 112128.
[123] M. Moll, *Radiation tolerant semiconductor sensors for tracking detectors*. Nucl. Instrum. Meth. A **565** (2006) 202–211.
[124] M. Pomorski, E. Berdermann, W. de Boer, A. Furgeri, C. Sander, J. Morse, *Charge transport properties of single crystal CVD-diamond particle detectors*, Diam. Relat. Mater. **16** (2007) 1066–1069.
[125] M. Nakhostin, *Charged particle response of transmission diamond detectors*. Nucl. Instrum. Meth. A **703** (2013) 199–203.
[126] G. Kramberger, M. Baselga, V. Cindro, P. Fernandez-Martinez, D. Flores, Z. Galloway, A. Gorišek, V. Greco, S. Hidalgo, V. Fadeyev, *Radiation effects in low gain avalanche detectors after hadron irradiations*, JINST **10** (2015) P07006.
[127] E. Gaubas, I. Brytavskyi, T. Čeponis, J. Kusakovskij, G. Tamulaitis, *Barrier capacitance characteristics of CdS–Cu2S junction structures*, Thin Solid Films **531** (2013) 131–136.
[128] H. M. Strong, R. M. Chrenko, *Diamond growth rates and physical properties of laboratory-made diamond*, J. Phys. Chem. **75** (1971) 1838–1843.
[129] C. M. Welbourn, M. Cooper, P. M. Spear, De Beers, *Natural versus synthetic diamond verification instruments*, Gems. Gemol. **32** (1996) 156–169.
[130] A. T. Collins, H. Kanda, R. C. Burns, *The segregation of nickel-related optical centres in the octahedral growth sectors of synthetic diamond*, Philos. Mag. B 61 (1990) 797–810.

[131] G. B. Bokiy, G. N. Bezrukov, J. A. Klyuev, A. M. Naletov, V. I. Neshpa, *Natural and synthetic diamonds* (Nauka, Moscow, 1986).
[132] S. C. Lawson, D. Fisher, D. C. Hunt, M. E. Newton, *On the existence of positively charged single-substitutional nitrogen in diamond*, J. Phys. Condens. Matter **10** (1998) 6171–6180.
[133] R. M. Chrenko, R. E. Tuft, H. M. Strong, *Transformation of the state of nitrogen in diamond*, Nature **270** (1977) 141–144.
[134] I. Kiflawi, A. E. Mayer, P. M. Spear, J. A. Van Wyk, G. S. Woods, *Infrared absorption by the single nitrogen and A defect centers in diamond*, Philos. Mag. B **69** (1994) 1141–1147.
[135] S.R. Boyd, I. Kiflawi, G.S. Woods, *The relationship between infrared absorption and the A defect concentration in diamond*, Philos. Mag. B **69** (1994) 1149–1153.
[136] J. I. Pankove, *Optical processes in semiconductors* (Prentice-Hall, New Jersey, 1971).
[137] E. Gaubas, A. Kaniava, *Determination of recombination parameters in silicon wafers by transient microwave absorption*, Rev. Sci. Instrum. **67** (1996) 2339–2345.
[138] K. Iakoubovskii and G. J. Adriaenssens, *Optical detection of defect centers in CVD diamond*, Diam. Relat. Mater. **9** (2000) 1349.
[139] G. Davies and M.F. Hammer, *Optical studies of the 1.945 eV vibronic band in diamond*, Proc. Roy. Soc. Lond. A **348** (1976) 285.
[140] G. Lucovsky, *On the photoionization of deep impurity centers in semiconductors*, Solid State. Commun. **3** (1965) 299.
[141] A. V. Mudryi, T. P. Laryonova, I. A. Shakin, G. A. Gusakov, G. A. Dubrov, V. V. Tikhonov, *Optical properties of synthetic monocrystals of diamond*, FTP (Semiconductors, English Version) **14** (2004) 538–542 (in Russian).
[142] V. Nadolinny, A. Yelisseyev, *New paramagnetic centres containing nickel ions in diamond*, Diam. Relat. Mater. **3** (1993) 17–21.
[143] S. Nokhrin, J. Rosa, M. Vanecek, A.G. Badalyan, M. Nesladek, *EPR study of preferential orientation of crystallites in N-doped high quality CVD diamond*, Diam. Relat. Mater. **10** (2001) 480–484.
[144] J. H. N. Loubser, W. P. van Ryneveld, L. du Perez, *Exchange interaction effects in the E.S.R. spectrum of substitutional nitrogen in diamond*, Solid State Commun. **3** (1965) 307–309.
[145] J.E. Field, *The Properties of Natural and Synthetic Diamonds*, (Academic Press, London, 1992).
[146] J. Isoya, H. Kanda, J. R. Norris, J. Tang, M. K. Bowman, *Fourier-transform and continuous-wave EPR studies of nickel in synthetic diamond: site and spin multiplicity*, Phys. Rev. B **41** (1990) 3905–3913.
[147] C. E. Nebel, M. Stutzmann, *Transport properties of diamond: carrier mobility and resistivity*, (Handbook, Diam. Relet. Mat. 2000)
[148] http://www.easyspin.org/

[149] A. Cox, M. E. Newton, J. M. Baker, *13C, 14N and 15N ENDOR measurements on the single substitutional nitrogen centre (Pl) in diamond*, J. Phys. Condens. Matter **124** (1994) 551–563.
[150] J. H. N. Loubser, W. P. van Ryneveld, *Electron spin resonance of nickel in synthetic diamonds*, Nature **5048** (1966) 517.
[151] E. Gaubas, J. Vaitkus, K. M. Smith, *Monitoring of carrier lifetime in GaAs substrate epi-layer structures by space-resolved transient microwave absorption*, Nucl. Instrum. Meth. A **460** (2001) 35–40.
[152] L. S. Pan, D. R. Kania, P. Pianetta, J.W. Ager III, M.I. Landstrass, S. Han, *Temperature dependent mobility in single-crystal and chemical vapor-deposited diamond*, J. Appl. Phys. **73** (1993) 2888–2894.
[153] E. Gaubas, T. Ceponis, J. V. Vaitkus, *Pulsed capacitance technique for evaluation of barrier structures* (Lambert Academic Publishing, Saarbrucken-Berlin Germany, 2013).
[154] E. Gaubas, T. Ceponis, S. Sakalauskas, A. Uleckas, A. Velicka, *Fluence dependent variations of barrier and generation currents in neutron and proton irradiated Si particle detectors*, Lith. J. Phys. **51** (2011) 230.
[155] E. Gaubas, T. Ceponis, J. Kusakovskij, *Profiling of barrier capacitance and spreading resistance by transient linearly increasing voltage technique*, Rev. Sci. Instrum. **82** (2011) 083304.
[156] E. Malguth et al., *Fe-Centers in GaN as candidates for spintronics applications*, in proceedings of 2005 MRS Fall Meeting, Boston, Massachusetts, U.S.A., November 27 – December 2 2005, Mater. Res. Soc. Symp. Proc. **892.**
[157] http://www.phystech.de/.
[158] D. K. Shroder, *Semiconductor material and device characterization*, (third edition, Wiley, New Jersey, 2006).
[159] J. C. Phillips, *Microscopic aspects of Stretched Exponential Relaxation (SER) in homogeneous molecular and network glasses and polymers*, J. Non-Cryst. Solids **357** (2011) 3853–3865.
[160] J. C. Phillips, *Stretched exponential relaxation in molecular and electronic glasses*, Rep. Prog. Phys. **59** (1996) 1133–1207.
[161] S. Nakamura and S. F. Chichibu, *Introduction to nitride semiconductor blue lasers and light emitting diodes* (Taylor & Francis, London, 2000).
[162] J. F. Ziegler, J.P. Biersack, M.D. Ziegler, *SRIM — The Stopping and Range of Ions in Matter* (SRIM Co., Chester U.K., 2008).
[163] E. Gaubas, T. Ceponis, J. Vaitkus, J. Raisanen, *Study of variations of the carrier recombination and charge transport parameters during proton irradiation of silicon pin diode structures*, AIP Adv. **1** (2011) 022143.
[164] R. J. McIntyre, *Multiplication noise in uniform avalanche diodes*, IEEE T. Electron. Dev. (1966).
[165] R. J. McIntyre, *The distribution of gains in uniformly multiplying avalanche photodiodes: Theory*, IEEE T. Electron. Dev. **ED-19** (1972) 703–713.

[166] R. J. McIntyre, *Factors affecting the ultimate capabilities of high speed avalanche photodiodes and a review of the state-of-the-art*, in IEDM Tech. Dig., (1973) 213–216.
[167] P. Yuan, K.A. Anselm, C. Hu, H. Nie, C. Lenox, A.L. Holmes, B.G. Strretman, J.C. Campbell, R.J. McIntyre, *A New look at impact ionization—part ii: gain and noise in short avalanche photodiodes,* IEEE T. Electron Dev. **ED-46** (1999) 1632.
[168] B. J. Baliga, *Fundamentals of power semiconductore devices* (Springer Science, New York, 2008).
[169] R. van Overstraeten, H. de Man, *Measurement of the ionization rates in diffused silicon p-n junctions*, Solid State Electron. **13** (1970) 583.
[170] W. Maes, K. De Meyer, R. Van Overstraeten**,** *Impact ionization in silicon: A review and update*, Solid State Electron. **33** (1990) 705.
[171] E. Gaubas, T. Ceponis, V. Kalesinskas, *Currents induced by injected charge in junction detectors*, Sensors **13**, 12295 (2013).
[172] G. F. Knoll, *Radiation Detection and Measurement* (third edition, John Wiley and sons, Michigan, 2000).
[173] P. Yuan, C. C. Hansing, K. A. Anselm, C. V. Lenox, H. Nie, A. L. Holmes, B. G. Streetman, J. C. Campbell, *Impact ionization characteristics of III-V semiconductors for a wide range of multiplication region thicknesses*, I.E.E.E. J. Quantum. Electron. **36** (2000) 198.
[174] M. A. Saleh, M. M. Hayat, B. E. A. Saleh, M. C. Teich, *Dead-space-based theory predicts excess noise factor for thin GaAs and AlGaAs avalanche photodiodes*, IEEE T. Electron Dev. **ED-47** (2000) 625.
[175] A. R. J. Marshall, P. Vines, P. J. Ker, J. P. R. David, Ch. H. Tang, *High speed InAs electron avalanche photodiodes overcome the conventional gain-bandwidth product limit,* I.E.E.E. J. Quantum Elect. **47** (2011) 858.
[176] K. M. van Vliet, A. Friedmann, L.M. Rucker, *Theory of carrier multiplication and noise in avalanche devices—Part II: Two-carrier processes*, IEEE Trans. Electron Devices **ED-26** (1979) 752.
[177] M. E. Levinstein, S. L. Rumyantsev, M. S. Shur, *Properties of advanced semiconductor materials GaN, AlN, BN, SiC, SiGe*, (Wiley, New York, 2001).
[178] M. Pomorski, E. Berdermann, M. Ciobanu, A. Martemyianov, P. Moritz, M. Rebisz, B. Marczewska, *Characterisation of single crystal CVD diamond particle detectors for hadron physics experiments*, Phys. Status Solidi A **202** (2005) 2199.
[179] G. Wang, K. Fu, Ch. Yao, D. Su, G. Zhang, J. Wang, M. Lu, *GaN-based PIN alpha particle detectors*, Nucl. Instrum. Meth. A **663** (2012) 10.
[180] W. van Roosbroeck, *The transport of added current carriers in a homogeneous semiconductor*, Phys. Rev. **91** (1953) 282.
[181] D. J. Griffiths, *Introduction to electrodynamics* (Prentice Hall, New Jersey, 1999).
[182] http://www.aixtron.com/en/products/technologies
[183] R. Resta, *Macroscopic polarization in crystalline dielectrics: The geometric phase approach*, Rev. Mod. Phys. **66 (**1994) 899–915.

[184] F. Bernardini, V. Fiorentini, D. Vanderbilt, *Polarization-based calculation of the dielectric tensor of polar crystals*, Phys. Rev. Lett. **79** (2002) 3958–3961.
[185] M. Sumiya, S. Fuke, *Review of polarity determination and control in GaN,* MRS Internet J. Nitride Semicond. Res. **9** (2004) 1–34.
[186] H. Morkoc, *Handbook on Nitride Semiconductors and Devices*, (Wiley-VCH: Hoboken, New Jersey, 2008).
[187] A. R. Smith, R. M. Feenstra, D. W. Greve, M. S. Shin, M. Skowronski, J. E. Neugebauer, J. E. Northrup, *Reconstructions of GaN(0001) and (0001) surfaces: Ga-rich metallic structures*. J. Vac. Sci. Technol. B **16 (**1998) 1–17.
[188] B. S. Eller, J. Yang, R. J. Nemanich, *Polarization effects of GaN and AlGaN: Polarization bound charge, band bending, and electronic surface states*, J. Electron. Mater. **43** (2014) 4560–4568.
[189] B. S. Eller, J. Yang, R. J. Nemanich, *Electronic surface and dielectric interface states on GaN and AlGaN,* J. Vac. Sci. Technol. A **31** (2013) 1–29.
[190] E. Gaubas, T. Ceponis, D. Meskauskaite, N. Kazuchits, *Profiling of current transients in capacitor type diamond sensors*, Sensors **15** (2015) 13424–13458.
[191] D. C. Look, D. C. Reynolds, J. W. Hemsky, J. R. Sizelove, R. L. Jones, R. J. Molnar, *Defect donor and acceptor in GaN*. Phys. Rev. Lett. **79** (1997) 2273–2276.
[192] S. Nakamura, T. Mukai, M. Senoh, *In situ monitoring and Hall measurements of GaN grown with GaN buffer layers*. J. Appl. Phys. **71** (1992) 5543–5549.
[193] V. W. L. Chin, T. L. Tansley, T. Osotchan, *Electron mobilities in gallium, indium, and aluminum nitrides*, J. Appl. Phys. **75** (1994) 7365–7372.
[194] M. Farahmand, C. Garetto, E. Bellotti, K. F. Brennan, M. Goano, E. Ghillino, G. Ghione, J. D. Albrecht, P. P. Ruden, *Monte Carlo simulation of electron transport in the III-nitride wurtzite phase materials system: Binaries and ternaries*, IEEE T. Electron Dev. **48** (2001) 535–542.
[195] J. W. Orton, C. T. Foxo, *Group III nitride semiconductors for short wavelength light-emitting devices*, Rep. Prog. Phys. **61** (1998) 1–75.
[196] M. Rubin, N. Newman, J.S. Chan, T.C. Fu, J.T. Ross, *p-type gallium nitride by reactive ion-beam molecular beam epitaxy with ion implantation, diffusion, or coevaporation of Mg*, Appl. Phys. Lett. **64** (1994) 64–66.
[197] K. Hecht, *Zum Mechanismus des lichtelektrischen Primarstromes in isolierenden Kristallen*. Z. Phys.**77** (1932) 235–245.
[198] A. Uleckas, *Contactless spectroscopy of native and technological defects in Si, Ge and GaN structures* (Doctoral dissertation, Vilnius, 2012).
[199] S. Vayrynen, P. Tikkanen, J. Raisanen, I. Kassamakov, and E. Tuominen, *Effects of activation by proton irradiation on silicon particle detector electric characteristics*, J. Appl. Phys. **106** (2009) 024908.